TRANSTION METAL OXIDES

FOR SOLAR WATER SPLITTING DEVICES

by

ADAM M. SMITH

A DISSERTATION

Presented to the Department of Chemistry and Biochemistry
and the Graduate School of the University of Oregon
in partial fulfillment of the requirements
for the degree of
Doctor of Philosophy

September 2015

DISSERTATION APPROVAL PAGE

Student: Adam M. Smith

Title: Transition Metal Oxides for Solar Water Splitting Devices

This dissertation has been accepted and approved in partial fulfillment of the requirements for the Doctor of Philosophy degree in the Department of Chemistry and Biochemistry by:

Dr. Mark C. Lonergan	Chairperson
Dr. Shannon W. Boettcher	Advisor
Dr. Cathy J. Page	Core Member
Dr. Ben J. McMorran	Institutional Representative

and

Scott L. Pratt	Dean of the Graduate School

Original approval signatures are on file with the University of Oregon Graduate School.

Degree awarded September 2015

DISSERTATION ABSTRACT

Adam M. Smith

Doctor of Philosophy

Department of Chemistry and Biochemistry

September 2015

Title: Transition Metal Oxides for Solar Water Splitting Devices

Although the terrestrial flux of solar energy is enough to support human endeavors, storage of solar energy remains a significant challenge to large-scale implementation of solar energy production. One route to energy storage involves the capture and conversion of sunlight to chemical species such as molecular hydrogen and oxygen via water splitting devices. The oxygen evolution half-reaction particularly suffers from large kinetic overpotentials. Additionally, a photoactive material that exhibits stability in oxidizing conditions present during oxygen evolution represents a unique challenge for devices. These concerns can be potentially addressed with a metal oxide photoanode coupled with efficient water oxidation electrocatalysts. Despite decades of research, structure-composition to property relationships are still needed for the design of metal oxide oxygen evolution materials.

This dissertation investigates transition metal oxide materials for the oxygen evolution portion of water splitting devices. Chapter I introduces key challenges for solar driven water splitting. Chapter II elucidates the growth mechanism of tungsten oxide (WO_X) nanowires (NWs), a proposed photoanode material for water splitting. Key findings include (1) a planar defect-driven pseudo-one-dimensional growth mechanism and (2)

morphological control through the supersaturation of vapor precursors. Result 1 is significant as it illustrates that common vapor-phase syntheses of WO_X NWs depend on the formation of planar defects through NWs, which necessitates reconsideration of WO_X as a photoanode. Chapter III presents work towards (1) single crystal WO_X synthesis and characterization and (2) WO_X NW device fabrication. Chapter IV makes use of the key result that WO_X NWs are defect rich and therefore conductive in order to utilize them as a catalyst scaffold for oxygen evolution in acidic media. Work towards utilizing NW scaffolds include key results such as stability under anodic potentials and strongly acidic conditions used for oxygen evolution. Chapter V includes work characterizing nickel oxide/oxyhydroxide oxygen evolution catalysts at near-neutral pH. Key findings include (1) previous reports of anodic conditioning resulting in greater catalytic activity are actually due to incidental incorporation of iron impurities from solution and (2) through intentional iron incorporation via electrochemical co-deposition, catalytic activity is increased ~50-fold over Fe-free catalysts.

This dissertation contains previously published coauthored material.

CURRICULUM VITAE

NAME OF AUTHOR: Adam M. Smith

GRADUATE AND UNDERGRADUATE SCHOOLS ATTENDED:

University of Oregon, Eugene, OR
University of Wisconsin - Madison, Madison, WI
University of Wisconsin - Marathon County, Wausau, WI

DEGREES AWARDED:

Doctor of Philosophy, Chemistry, 2015, University of Oregon
Master of Science, Chemistry, 2012, University of Oregon
Bachelor of Science, Chemical Engineering, University of Wisconsin - Madison

AREAS OF SPECIAL INTEREST:

Materials Chemistry
Electrochemistry
Solar Energy Conversion

PROFESSIONAL EXPERIENCE:

Analytical and Development Lab Intern, Hewlett Packard, Summer 2014
Designed, assembled, and tested prototype sensor platforms.

Research Assistant, Boettcher Research Group, University of Oregon 2011-2015
Materials chemistry research with focus on transition metal oxides for solar water splitting applications. Crystal growth, electrocatalysis, instrument design, jack of all trades.

GK-12 Fellow, National Science Foundation, University of Oregon, 2012-2013
6-Week scientist in residence at Stella-Mayfield Elementary School

Chem-Nano REU, Dr. Juan de Pablo Research Group, Summer 2008
Researched visco-elastic properties of nanomaterial composites

GRANTS, AWARDS, AND HONORS:

NSF GK12 Fellowship, University of Oregon, 2012

Promising Scholar Award, University of Oregon 2010

Colbeck Engineering Award, University of Wisconsin – Madison, 2008

Carol A. Tobakos Memorial Engineering Scholarship Award, University of Wisconsin – Madison , 2007

Departmental Distinction Award in Chemistry, University of Wisconsin – Marathon County, 2006

Greenheck Engineering Scholarship, University of Wisconsin – Marathon County, 2005

Student Leader of the Year, University of Wisconsin – Marathon County, 2004

PUBLICATIONS:

Burke, M. S., Kast, M. G., Trotochaud, L., Smith, A., Boettcher, S. W. Cobalt-iron (oxy)hydroxide oxygen evolution electrocatalysts: The role of structure and composition on activity, stability, and mechanism. Accepted: *Journal of the American Chemical Society*, **2015**.

Athavan, N., Wu, M. Z. B., Archila, K., Kast, M.G., Smith, A.M., Keszler, D.A., John F. Wager, J.F., and Boettcher, S.W., Amorphous In-Ga-Zn-oxide semiconducting thin films deposited from electrochemically-generated aqueous cluster precursor inks, Submitted, **2015**.

Smith, A. M., Trotochaud, L., Burke, M.S. and Boettcher, S.W. Contributions to activity enhancement via Fe incorporation in Ni(oxy)-hydroxide/borate catalysts for near-neutral pH oxygen evolution, *Chemical Communications*, **2014**, DOI: 10.1039/C4CC08670H

Smith, A. M., Kast, M. G., Nail, B. A., Aloni, S. and Boettcher, S.W. A planar-defect-driven growth mechanism of oxygen-deficient tungsten oxide nanowires, *Journal of Materials Chemistry A*, **2013**, DOI: 10.1039/c3ta14163b.

ACKNOWLEDGMENTS

This work was partially supported by the Office of Naval Research, through the Oregon Nanoscience and Microtechnologies Institute. I also acknowledge support from the user program at the Molecular Foundry, Lawrence Berkeley National Laboratory, with funding from the U.S. Department of Energy Office of Science, Office of Basic Energy Sciences under Contract DE-AC02-05CH1123 as well as additional support by the National Science Foundation through CHE-1301461. I acknowledge additional support from the National Science Foundation grant DGE-0742540 as a GK-12 teaching fellow. This work also relied heavily on the Center for Advanced Material Characterization in Oregon (CAMCOR) shared instrument facilities which are supported by grants from the W.M. Keck Foundation, the M.J. Murdock Charitable Trust, ONAMI, the Air Force Research Laboratory (FA8650-05-1-5041), NSF (0923577 and 0421086) and the University of Oregon. I sincerely thank the talented CAMCOR staff, in particular Kurt Langworthy, Josh Razink, Jeff Ditto, Steve Golledge, and Steve Wiemholt for all your help and expertise. Additional thanks go to the TSA student shops, in particular Kris Johnson for his wealth of mechanical knowledge.

I also wish thank my amazing colleagues, without whom I couldn’t have succeeded. In particular I’d like to thank my co-authors: Matt Kast, Ben Nail, Dr. Lena Trotochaud, Micahela Burke, Dr. Athavan Nadarajah and our collaborator at the Molecular Foundry, Shaul “Time To Be Famous” Aloni. I also thank the other Team Catalysis researchers Lisa Enman, Adam Batchellor, Shihui Zou and Hyosang Jeon. A special thanks to Dr. Fuding Lin, Jason Boucher, and Annie Greenaway for many great

scientific and philosophical discussions. Additionally, thanks to all the other Boettcher lab researchers, past, present, and future as well as all the other graduate students I've collaborated or commiserated with throughout the years.

I extend my sincere thanks to my committee members who contributed meaningfully to my scientific and professional development. I also thank my advisor Dr. Shannon Boettcher for continually challenging me. I would like to express my gratitude to Hewlett-Packard for the great summer internship opportunity, with particular thanks to my mentor Dr. Greg Long.

Special thanks go out to Dr. Juan de Pablo for the opportunity to do undergraduate research and to Mr. Bill Heeren, my high school chemistry teacher who inspired me to think with my 'mind's eye'. I additionally thank my undergraduate professors Dr. Theo Koupelis who tried to warn me and Dr. Joel Case who said it would be alright. I would also like to express a heartfelt gratitude to all the other teachers I've had throughout the years, without whom none of this would be possible.

A big thanks to my Wisconsin tribe. Mom and Dad, Jeff and Shandra; you have been there for me through so much. I could not ask for better parents. Thanks to my grandparents, for showing me the value of hard work and a good garden. To all my aunts, uncles, cousins and the rest of my family, you are wonderful and kind folks, even in the face of adversity. A shout out to my chosen family for not stepping on my head: Lynn, Nicky, Josh, Scott, Gabe, Cassidy, John John, The Brothers Stanecki, Kevin and Kat Molter, Annika, DeAnne, Fallah, Jason and all the other freaks and geeks I love so much.

Lastly, thanks to my amazing partner Megan and our wonderful daughter Lilia for staying by my side through the ups and downs of graduate school.

In loving memory of

Jacob Arthur Smith

And

T.J. Mills

Shine on you crazy diamond(s)

TABLE OF CONTENTS

Chapter Page

Chapter Page

LIST OF FIGURES

Figure Page

Figure Page

Figure Page

LIST OF TABLES

Table Page

CHAPTER I

POWER TO THE PEOPLE AND THE STORAGE PROBLEM

Throughout the course of human events there have been few challenges that pose as great of a potential threat to civilization as climate change.[1-10] Despite mounting evidence of anthropomorphic climate change driven primarily through fossil fuel utilization and the dire predictions of increasing atmospheric CO_2 concentrations, few steps have been taken to reduce global consumption of carbon intensive energy sources.[11-17] Through a diverse energy portfolio comprised primarily of renewables, the increase of atmospheric CO_2 could be abated and the potentially catastrophic ramifications averted. In particular, solar energy stands out as a vastly under-utilized energy source, with theoretically extractable solar on the order of ~1000x greater than that needed for human activity.[18] It is well known that the flux of solar energy varies substantially geographically, diurnally and seasonally; making energy storage a significant challenge to the large scale integration of solar devices. One proposed solution involves the capture and conversion of solar energy to chemical fuels (e.g. H_2, CH_3OH etc.), which have significantly larger energy densities than other potential storage strategies such as batteries or capacitors.[19-22] Table 1.1 shows a comparison of energy densities for prominent storage and conventional generation technologies.

Table 1.1. Comparison of Energy Density and Specific Energy of Various Storage Methods

Storage Technology	Energy Density (MJ/L)	Specific Energy (MJ/kg)	Method	Refs
Hydrogen (690 atm)	4.5	142	Chemical	21, 23
Hydrogen (STP)	0.01	142	Chemical	21, 23
Li-Ion (rechargable)	1-2	0.4	Electrochemical	24
Coal (anthrathrite)	39	30	Chemical	25
Gasoline	32	44	Chemical	26
Diesel	38	46	Chemical	26
Alkaline Battery	1.8	0.7	Electrochemical	27, 28
Capacitor	10^{-5} - 10^{-3}	10^{-5}	Electrostatic	20, 29, 30
Compressed Air (300 atm)	0.2	0.5	Mechanical	31
Flywheel	-	0.4	Mechanical	32, 33
Pumped Hydro (100 m)	0.001	0.001	Mechanical	28

Chemical fuel systems such as compressed H_2 and petroleum products have the potential to outperform most other approaches, particularly for use in the transportation sector which requires both high specific energy and high energy density. Solar generated fuels such as compressed hydrogen and methanol have appropriate energy densities and specific energies, making them well suited for the transportation sector which alone accounts for ~16% of CO_2 emissions.[34] Two proposed routes to chemical storage involve hydrogen evolution and carbon dioxide reduction (CDR) as shown in equations 1.1, 1.2 and 1.3.[35-38]

OER (acid) $$2\mathrm{H}_2O(l) \rightarrow O_2(g) + 4H^+(aq) + 4e^- \qquad (1.1.A)$$

HER (acid) $$2H^+(aq) + 2e^- \rightarrow H_2(g) \qquad (1.1.B)$$

And the relevant reactions in basic media:

OER (base) $$4OH^-(aq) \rightarrow 2H_2O(l) + O_2(g) + 4e^- \qquad (1.2.A)$$

HER (base) $$2H_2O(l) + 2e^- \rightarrow H_2(g) + 2OH^- \qquad (1.2.B)$$

The electrochemical reduction of CO_2 to CO is as follows:

OER (acid) $$2\mathrm{H}_2O(l) \rightarrow O_2(g) + 4H^+(aq) + 4e^- \qquad (1.3.A)$$

CDR (acid) $$CO_2(g) + 2H^+(aq) + 2e^- \rightarrow CO(g) + H_2O(l) \qquad (1.3.B)$$

Although liquid fuels generated from CO_2 reduction would be easier to integrate into the existing energy infrastructure, hydrogen remains a promising storage medium. Hydrogen evolution is technologically more mature and the products (H_2 and O_2) can be easily separated spatially and are effectively ready for use.[39-41] Liquefied fuels from CO_2 are currently only viable on a laboratory scale and would require a great deal more basic research to become a viable terra-watt storage technology.[42-44] Additionally, once large-scale H_2 generation is economical, CO_2 methanation via routes such as the Sabatier reaction can be used to produce hydrocarbon fuel stocks.[45-47] Furthermore, fully optimized large scale solar water splitting provides the added benefit of serving as an effective water purification method.[48-50] Potable water is already scarce in developing nations and is an increasingly emerging crisis in industrial nations.[51-55] The generation of H_2 and O_2 from non-potable water (e.g. wastewater, saline water, etc.) and the subsequent combustion for power generation produces high purity water, a prospect that opens exciting possibilities of coupling power generation to water purification and waste management.[56]

Catalyst Materials for OER in Near-Neutral and Basic Media

In both H_2 evolution and CO_2 reduction energy storage strategies, the efficiency of the oxygen evolution half reaction (OER) has a significant impact on the overall conversion efficiency.[57-59] In the case of hydrogen evolution on a Pt electrode, the overpotential is moderate compared with that of OER.[60-62] Such a large kinetic overpotential makes developing new OER electrocatalysts while pursuing a fundamental understanding of their operation key steps toward efficient solar storage technologies.

Although the OER mechanism is not fully understood, it is believed to progress along a series of oxide, hydroxide, oxo, and peroxide intermediates when performed on metal-oxide catalysts in base as illustrated in the scheme shown in figure 1.1.[63, 64] Oxygen evolution involves the transfer of $4e^-$ per O_2 molecule, which makes mechanistic and catalytic studies particularly challenging. Investigation into electrocatalysts for OER has been confounded by the fundamental difficulty of maintaining trace material purity in the strongly acidic or basic conditions commonly employed.[65] Recent work by Boettcher and coworkers demonstrated the complexity of studying OER catalysts due to substantial changes in material composition after prolonged use in basic media.[66, 67] It was found that contrary to many reports of highly active $NiO_X/Ni(OH)_2/NiOOH$ OER catalysts, NiOOH suffers a much larger overpotential and therefore is a poor material for the oxygen evolution reaction. Instead, it was discovered that the incorporation of significant amounts of Fe from electrolyte and even glassware etching results in large improvements in activity. Additionally, it was shown that through the intentional addition of Fe into the Ni system highly active Fe:NiOOH electrocatalysts can be rationally designed.

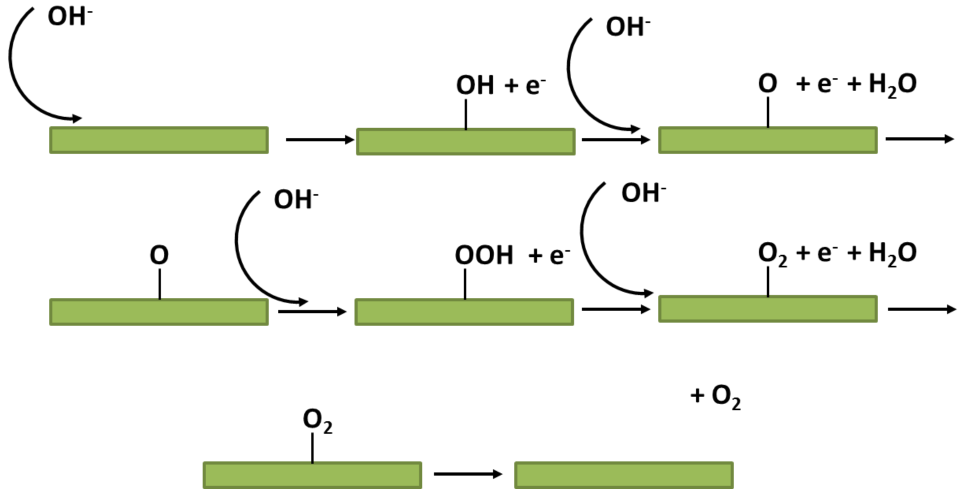

Figure 1.1. Proposed oxygen evolution mechanism on metal-oxide catalysts in base

The role of Fe in the transition metal oxy-hydroxide systems is not yet understood. Corrigan, whose work on the oxy-hydroxide materials centered on battery applications, proposed that an increase in NiOOH conductivity from Fe incorporation was responsible for the observed increase in OER activity.[68] Trotochaud et al., however, demonstrated that that although there was an order of magnitude increase in conductivity with Fe addition, it was not enough to account for the disparity in catalytic activity.[66] Another hypothesis is based on work from Bell and coworkers who observed an increase in turn over frequency (TOF) as the number of effective monolayers of catalyst decreased.[64] They showed that the metal substrates (e.g. Au, Pt etc.) were potentially having an electron withdrawing effect on the CoOOH catalyst, which activates the films. It is possible that Fe in the oxy-hydroxide catalysts films has a similar effect when incorporated, though Trotochaud demonstrated that the TOF dependence on film thickness was decreased in Fe:OOH catalyst films. Although it was suggested that a partial charge transfer may be responsible for some of the observed increase in catalytic activity, the extent and role of this is not yet clear. In conclusion, OER electrocatalysts stand to benefit immensely from rigorous research into their operation, particularly regarding the presence and role of Fe in transition metal oxy-hydroxide catalyst materials.

Materials for OER in Acidic Media

Another challenge in designing OER systems for large-scale integration is material compatibility issues. Materials must not only be stable in the media of interest (e.g. acid, base), but also at strongly oxidizing potentials at which corrosion is particularly common. Although many metal-oxides are stable in basic media, common equipment such as glass can be etched in the concentrated solutions used, particularly those at elevated temperature.[65, 69, 70] Material stability challenges for OER in acid are even more pronounced. Although there are many reports of base-stable OER electrocatalysts, there are few that are stable under acidic conditions.[71, 72]

Among the few acid-stable electrocatalysts, IrO_X remains among the most active despite significant research to find alternatives.[72] In order to achieve large-scale integration of solar-to-fuels systems, costs must be minimized for all system components while maintaining efficiency. A primary disadvantage of utilizing Ir based catalysts is the relative rarity and cost of Ir metal itself. One strategy to combat the high cost of Ir catalysts is to utilize a nanostructured scaffold to maximize the catalytically active surface area. There are few materials that meet the exacting criteria needed for OER in acidic media: stability in acid and under oxidizing conditions, conductive, and easily processable into high surface area nanostructures. One class of materials that satisfy these demanding conditions are the higher oxides of tungsten. Fully stoichiometric tungsten oxide (WO_3) has been proposed as a photoanode material for oxygen evolution due to a visible band gap of ~2.6-2.8 eV, acid stability, and resistance to photocorrosion.[73-75] Additionally, tungsten oxides are known to readily form nanowire (NW) structures under the right conditions.[76-79] Psuedo-1D morphology (i.e. nanowires) have been proposed to circumvent the limitations of the poor minority diffusion lengths common in metal-oxide semiconductors, as pictured in figure 1.2.[80-84]

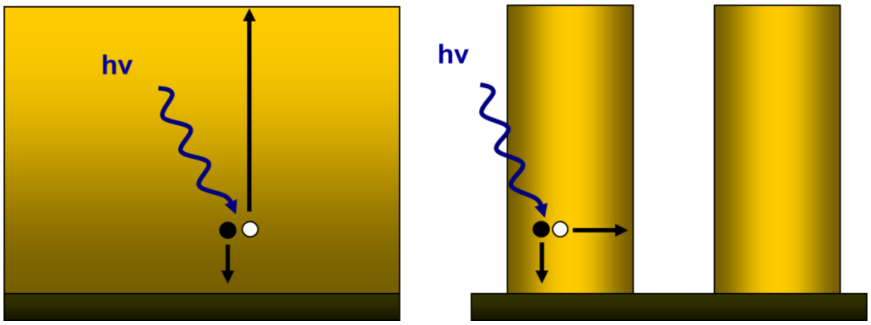

Figure 1.2. Illustration comparing planar and NW morphology

By utilizing semiconducting NWs with diameters less than the diffusion length of the bulk material, it is possible to collect more carriers as they are less likely to be lost to recombination as in bulk diffusion. It is also possible to have similar light absorption with a NW array as a planar film of similar thickness while utilizing less material overall. Interestingly, it was recently found that the 1-D morphology observed in thermally grown NWs was likely due to a defect mediated growth mechanism, and that such structures are inherently defect dense.[85] It has been known for decades that the tungsten/oxygen binary system exhibits a number of distinct phases (e.g. WO_3, W_2O ect.) as well as a plethora of nonstoichiometric phases (e.g. $WO_{2.73}$, $W_{18}O_{49}$, etc.) which vary widely in O:W ratios.[86-88]

At room temperature fully stoichiometric WO_3 is monoclinic and exhibits a mildly distorted ReO_3 structure (figure 1.3).[89] In the bulk, WO_3 is comprised of corner sharing WO_6 octahedra and as the density of oxygen vacancies increase, the structure partially collapses and octahedra coalesce becoming edge sharing (figure 1.4).[90-92] These planar defects were observed to preferentially orient along a class of (10*l*) planes (e.g. (102), (103), etc.) forming what are known as crystallographic shear planes.

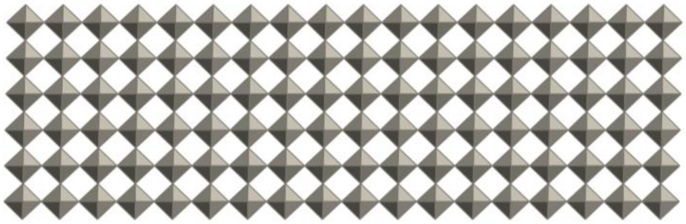

Figure 1.3. Projection along (010) of stoichiometric tungsten oxide

Defects in semiconductor materials are known recombination centers for photo-generated charge carriers.[93-95] Such highly defective structures are likely to be poor photoanode materials and may partially explain observations of poor NW and substoichiometric film photoelectrochemical response in illuminated experiments.[96, 97] Substoichiometric oxides are also conductive, becoming more metallic with increasing nonstoichiometry.[86, 87, 98] This conductivity makes WO_X NW arrays a potential scaffold with rare stability in acidic conditions.

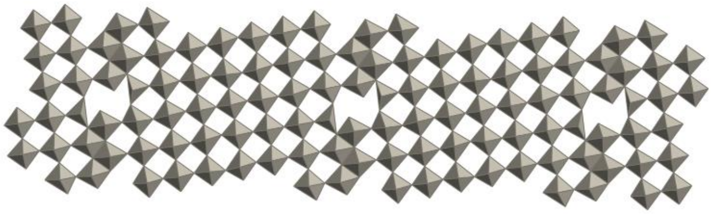

Figure 1.4: Projection along (010) of $W_{20}O_{73}$. Shear planes are visible as clusters of edge sharing WO_6 octahedra

Metal Oxides for Solar Applications

The following body of work will detail research investigating transition metal oxide materials for applications in solar water splitting. Transition metal oxides as a class of materials represent a rich research environment, particularly in the field of sustainable materials chemistry. Metal oxides are often abundant, generally chemically and thermally stable, and exhibit relatively low toxicity. Additionally, metal oxides can often be easily processed using thermal, electrochemical or even solution methods.[99, 100] As a whole, transition metal oxide materials for solar energy capture and storage represent an exciting intersection of basic science and commercial application.

This dissertation contains previously published coauthored material. Portions of Chapter II were previously published with Matt G. Kast, Benjamin A. Nail, Shaul Aloni and Shannon W. Boettcher. Portions of Chapter V were previously published with Lena Trotochaud, Michaela S. Burke and Shannon W. Boettcher.

CHAPTER II

PLANAR-DEFECT-DRIVEN GROWTH MECHANISM OF OXYGEN DEFICIENT TUNSGTEN OXIDE NANOWIRES

Portions of this chapter were previously published as Smith, A. M.; Kast, M. G.; Nail, B. A.; Aloni, S.; Boettcher, S. “Planar-Defect-Driven Growth Mechanism of Oxygen Deficient Tungsten Oxide Nanowires” in the Journal of Materials Chemistry A, 2014, 2, 6121. A.M.S. wrote the publication, synthesized samples and performed characterization. M.G.K. performed XPS analysis. B.A.N. aided in the construction of the reactor as well as growth optimization. S.A. performed TEM analysis on nanowire cross-sections. S.W.B. provided editorial assistance and served as principle investigator.

.

Introduction

The controlled synthesis of nanostructured metal oxides is important for their use in a wide range of applications. Of particular interest are one-dimensional (1D) nanowire structures exhibited by many metal oxides.[1-4] Tungsten oxides can be grown with a range of nanostructures and have applications in energy, sustainability, and electronics.[5, 6] With a band gap of 2.6-2.8 eV, WO_3 is a potential n-type semiconductor for solar water splitting.[7-9] Tungsten oxides are used in electrochromics (e.g. for smart windows), heterogeneous oxidation catalysts, gas sensing probes, pH sensors and field emitters.[10-14] Understanding the growth mechanism of tungsten oxide NWs is important to rationally design them for applications and to improve the general understanding of oxide nanowire growth.

At room temperature stoichiometric WO_3 adopts a monoclinic crystal structure comprised of corner-sharing WO_6 octahedra resembling distorted cubic $ReO_{3.}$[15] Upon mild reduction, O vacancies are formed and coalesce to form substoichiometric planar defects referred to as crystallographic shear planes.[16-18] The defect planes are composed of edge-sharing W-O octahedra within the monoclinic WO_3 lattice.[19-21] In bulk systems, substoichiometric defects can be oriented along the (102), (103) or (104) crystallographic planes. Randomly spaced defects are known as Wadsley defects.[19] If the defect planes are periodically ordered they form one of two homologous series of Magneli phases. The first homologous series gives rise to compositions of the form W_nO_{3n-1} where the defect planes are ordered along (102) for n ranging from 30 to 19 (e.g. $WO_{2.97}$ to $WO_{2.94}$); n is the number of octahedra between defects. When the planar defects are aligned along the (103) planes, a second homologous series of the form W_nO_{3n-2} is observed for integer n from 25 to 15 (e.g. $WO_{2.92}$ to $WO_{2.87}$).[21]

In general, 1D nanowire growth is the result of anisotropic material deposition, with relatively fast growth along one axis. Such asymmetry has been achieved in various ways. Burton, Cabera and Frank showed that screw dislocations produce a stepped surface where the growth rate can be enhanced and thus yield 1D structures.[22] Jin and coworkers showed that screw-dislocation-driven growth provides a powerful mechanism for metal oxide NW and nanotube synthesis. Under low supersaturation conditions, NWs and nanotubes were produced while at high supersaturation, bulk deposition and layer-by-layer (LBL) growth was observed.[4, 23] Ellis and Wagner found 1D growth can proceed via a vapor-liquid-solid (VLS) mechanism.[24] In VLS, vapor species are absorbed by a liquid catalyst that becomes supersaturated and a solid precipitates at the solid-liquid interface. The catalyst droplet defines the size of the NWs synthesized by the VLS method and is carried at the leading edge during growth. The catalyst typically remains at the growth front unless removed by another process.[25] Colloidal/hydrothermal techniques also can yield 1D materials by controlling solution temperature and heating rate.[26-28] Ligands are often added to control the surface energy and hence promote or inhibit the growth rate of certain crystal faces.[29] Surface-energy-controlled growth is also thought to play a role in vapor-phase syntheses of 1D nanostructures in the metal-organic chemical vapor deposition (MOCVD) growth of GaAs nanowires by selected area epitaxy.[30]

The synthesis of one-dimensional tungsten oxide “micro-needle” structures have been reported as early as the 1940’s.[16-18] More recently, Gu *et al.* reported that tungsten oxide NWs form on a metallic tungsten tip heated to 700 °C in the presence of trace oxygen.[1] A vapor-solid (VS) growth mechanism was proposed, although a driving force favoring 1D structures over other morphologies was not discussed. Komjima *et al.* also proposed a solid-phase growth mechanism for NW growth, where imperfections/unevenness of the W film serve as NW nucleation sites during film oxidation.[31] In contrast, Liu *et al.* proposed a VLS mechanism for tungsten oxide NW growth on 500 nm sputtered W films coated with a 5-nm-thick Au or Ni film in an Ar/H_2

atmosphere.[32] Although thin films of Au form liquid droplets at elevated temperatures which catalyze, for example, Si NW growth, [24] no evidence for residual catalyst particles on the tips of the tungsten oxide nanowire surfaces were found in the published SEM images. Cui *et al.* propose that tungsten oxide nanowires form via the gas-phase nucleation of nanosized crystals/grains from a supersaturated vapor which then join the growing NW preferentially along the (010) growth direction.[33] This hypothesis is based on the observation of sub-micron granules on the NW surface, however these have also been observed by others upon annealing at temperatures above 500 °C in sufficient oxygen.[34] In another study, Thangala et al. suggested that highly oxygen deficient WO_2 species propagated at the tip of the NW, directing the 1D growth.[35] Defects associated with oxygen deficiency were also suggested to play a role in branching of tungsten oxide structures by Zhou *et al.* synthesized by thermal evaporation of W powder under vacuum and Ar flow.[36] Among published accounts of tungsten oxide NW syntheses, growth along the (010) direction has been commonly observed. Additionally, the presence of stacking faults in high-resolution transmission electron microscopy (HRTEM) and streaking from planar defects can be seen in previous reports of NW synthesis,[37-41] although a clear correlation between substoichiometry and morphology has not been drawn.

Herein we present evidence for a planar-defect-driven growth mechanism of substoichiometric tungsten oxide NWs based on electron microscopy, X-ray photoelectron spectroscopy (XPS), and X-ray diffraction (XRD) analysis of samples grown under a variety of conditions. We find that NW growth requires the presence of a metallic W film that reduces vapor species and yields oxygen deficient defects parallel to the NW growth direction. The addition of O_2 prevents the formation of planar defects and inhibits the formation of NWs, indicating that the substoichiometric defects provide the surface energy disparity that drives anisotropic growth. By controlling supersaturation via the temperature gradient, we find that NW growth only occurs at low supersaturation (and hence slower growth rates). The results provide insight into the synthesis of tungsten oxide nanostructures and indicate a fundamental relationship between planar defects, substoichiometric composition and NW morphology that may generally apply to oxide nanostructures.

Methods

Growth Substrates

Si wafers (Sb-doped (100)-oriented n-type, 0.007-0.02 Ω-cm, SUMCO) were cleaned with piranha solution at 60 °C for 10 min and then with 20:1 buffered HF oxide etch for 10 min (J. T. Baker). After rinsing in 18.3 MΩ water, the wafers were stored in 200 proof ethanol prior to W deposition. ~40-nm-thick W films were deposited in a magnetron sputter system (Denton Discovery 3014) at 60 W power with 30 standard cubic centimeters per minute (SCCM) Ar for 60 s with a 3” metallic W target (99.95%, Alfa Aesar). W-coated substrates were cut to size and rinsed with ethanol and dried immediately before growth. WO_3-coated substrates were produced by oxidizing W-films in air at 500 °C for 30 min.

Synthesis of Tungsten Oxide Nanostructures

Growth was performed in a horizontal 1” diameter tube reactor composed of a three-zone furnace with a custom-built temperature controller (figure 2.1). The reaction pressure was maintained at 500 mTorr using a MKS 253B throttle valve coupled with a MKS Baratron 10 Torr capacitance manometer and continuous operation of a mechanical vacuum pump. Ar and O_2 reaction gases were introduced using mass flow controllers (STEC/MKS). Tungsten trioxide powder (99.9%, Fluka) was oxidized in air at 700 °C for 12 hr prior to use. A quartz boat was loaded with 0.1 g WO_3 powder and positioned in the upstream zone. For all runs the reactor was evacuated to 4 mTorr before being backfilled with transport gas at 500 mTorr for 30 min prior to the heating steps. Prior to each run, leak rates were measured to be less than 3×10^{-3} SCCM of air. The heating steps and gas flow rates were controlled using LabView (National Instruments).

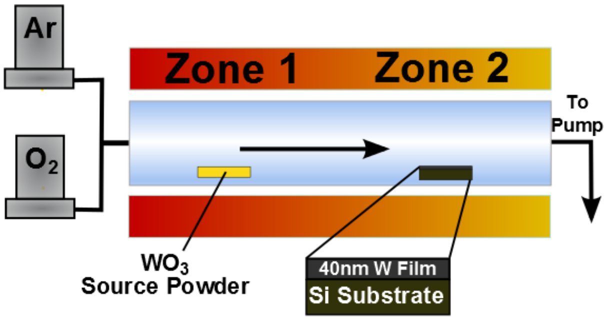

Figure 2.1. Oxide reactor schematic

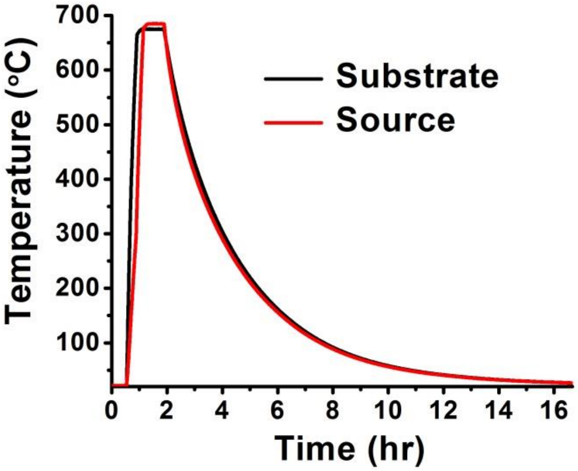

Figure 2.2 Experimental NW growth temperature profile with source and substrate temperatures in red and black respectively.

To synthesize tungsten oxide NWs, W-film substrates were loaded 12 cm downstream from the WO_3 source. After evacuation, the reactor was purged with 10 SCCM of Ar gas. To prevent deposition during the ramp-up to the growth temperature, substrates were preheated to 200 °C before heating substrate and source zones to 675 °C and 685 °C, respectively. This process maintained the substrate at a higher temperature than the source during the heating steps constraining $T_{Substrate} > T_{Source}$ for the duration of the ramp-up phase and inhibits material deposition below target reaction temperatures. Similarly, the source zone is closer to the exterior of the furnace, resulting in a slightly faster cooling rate. This geometry prevents deposition from the source to substrate during cooling. All growths were carried out for 1 hr, after which the reactor was allowed to cool to room temperature naturally (figure 2.2). For some of the experiments, the NWs were then oxidized by annealing at 400, 500, 550 or 600 °C in air for 30 min.

Polycrystalline tungsten oxide films were synthesized under several growth conditions, including: (1) replacing the W substrate with a WO_3 film with all other reaction parameters as described in the NW synthesis above, (2) increasing the source temperature to 700 °C, or (3) by introducing ultra high purity O_2 gas (Air Liquide America Specialty Gases) at 5 SCCM, 2 SCCM, 1 SCCM and 0.1 SCCM O_2 flow rates (250, 100, 50 and 5 mTorr P_{O2} respectively) mixed with Ar to maintain a constant total volumetric flow of 10 SCCM.

Characterization

The mass of WO_3 deposited was measured using a TGA Q500 microbalance by weighing the substrate before and after growth. Scanning electron microscope (SEM) images were acquired with a Zeiss Ultra-55 with an in-lens secondary electron detector and an accelerating voltage of 3 keV. Cross-sectional images were collected from cleaved samples mounted perpendicular to the electron beam. Transmission electron microscopy (TEM) analysis of the NWs was performed in bright-field mode on an FEI Titan 80-300 microscope using a 300 keV accelerating voltage. Whole NWs were imaged on 300 mesh lacey carbon/Cu TEM grids (Ted Pella). The Formvar backing was first removed by submersion in chloroform for 10 s. NWs were transferred by wetting the NW array with ethanol and sliding the grid across the surface of the substrate. NW cross-sections for

TEM analysis were prepared by focused-ion-beam (FIB) milling using a FEI Helios Dual-Beam instrument equipped with an Autoprobe 200 (Omniprobe, Oxford Instruments). NWs were first transferred to a Si wafer with a thermal oxide by sliding the sample linearly across the Si. A ~50 nm carbon contrast layer was deposited by thermal evaporation. Following C deposition, samples were mounted and thin bead of Pt deposited using the electron gun over the region of interest (figure 2.3.A). A second Pt protecting layer was then deposited using the ion gun (figure 2.3.B). The area around the region of interest was milled (figure 2.3.C) and subsequently thinned using the contrast between the two different Pt films to indicate the region of interest. Thinning was performed at decreasing accelerating voltages until the sample became electron transparent (figure 2.3.D and insert) to prevent beam damage and re-deposition of ablated materials. After mounting on a silicon half-TEM grid (Dune Sciences, Eugene, OR), NW samples were stored under vacuum until TEM imaging.

The thickness of W growth substrates was measured using X-ray reflectivity (XRR) on a Bruker AKS D8 Discover diffractometer. Reflectivity measurements were acquired at three spots on the sputtered W films and modeled using Bede Refs (Bede Scientific, UK).

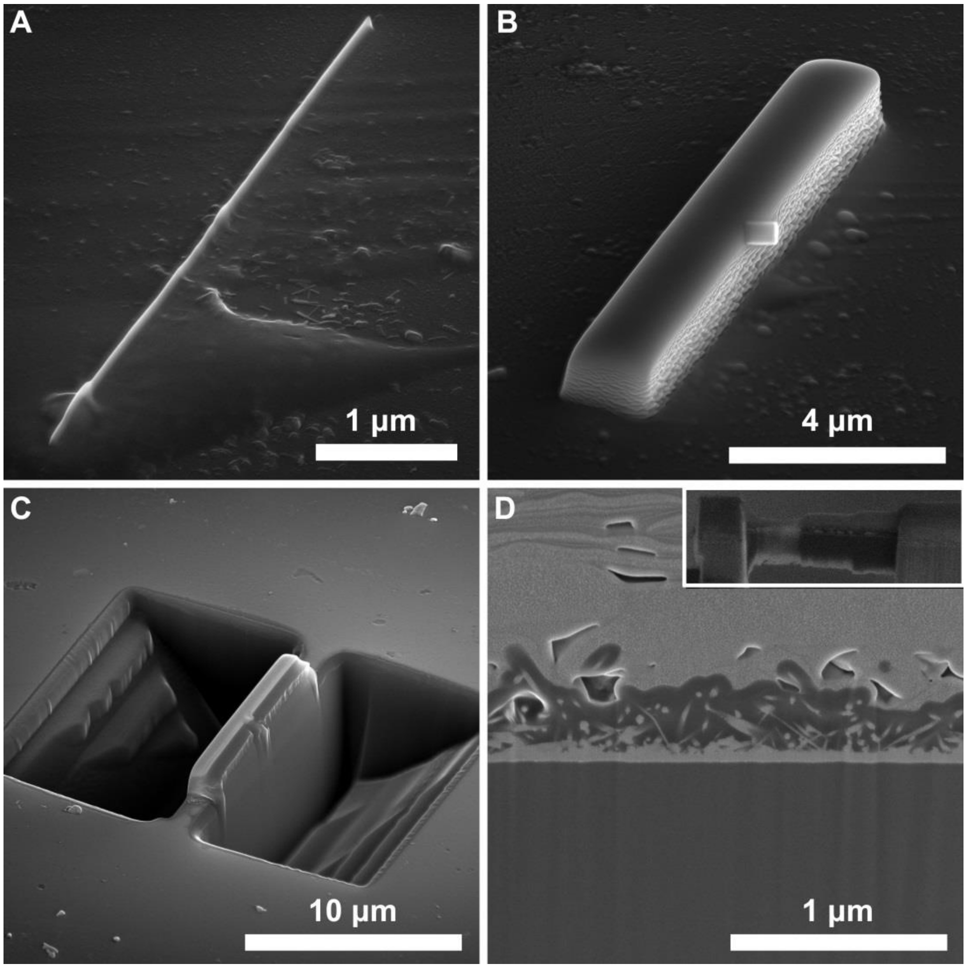

Figure 2.3. SEM images of the steps in the preparation of a representative cross-sectional NW sample. (A) Deposition of Pt bead over region of interest using the electron beam (previously coated with a blanket layer of C). (B) Larger Pt protecting layer deposited using the ion-beam. (C) Ion milling of sample. (D) Sample thinning showing presence of NWs in cross section and partially electron transparent sample (inset).

X-ray diffraction (XRD) patterns were collected on a Scintag XDS 2000 diffractometer equipped with an Inel CPS 120 linear detector with a collection time of 16 hr. X-ray photoelectron spectroscopy (XPS) was performed on an ESCALAB 250 (ThermoScientific) equipped with a monochromatic Al Kα X-ray source set at 150 W with a 500 um spot size. The W4f and Au4f regions were scanned 15 times with a pass energy of 20 eV. Data analysis was performed using ThermoScientific Avantage v4.75 software. A “Smart” fit was employed to subtract the backgrounds of all spectra. Approximately 1 nm of Au was thermally evaporated on all the samples and all binding energies were calibrated by setting the Au4f7/2 peak to 84.0 eV. Two peaks were used to fit the W4f7/2 and W4f5/2 peaks for each tungsten environment. During peak fitting the following constraints were set; the binding energy of the W4f5/2 peak for a given environment was set to 2.18 ± 0.1 eV higher than that of the W4f7/2, the height of the W4f5/2 was set to 75% of the height of the W4f7/2 peak, the FWHM of all W4f peaks for a given sample were constrained to be equal, the Lorentzian-Gaussian % (LG) was constrained to be equal for all W peaks for a given sample. An unconstrained W5p3/2 peak was included in the fit (location, height and FWHW unconstrained, LG constrained as mentioned before) at ~ 41.5 eV as this peak overlaps with the W4f peaks at higher binding energies.

The ratio of the areas of the W4f$_{7/2}$ peaks assigned to the W^{+6} and W^{+5} (lower binding energy) was used to determine the ratio of W^{+6} to W^{+5} in samples. We note that the ~1.4 eV shift to lower binding energies is consistent with the expected shift between W^{+6} and W^{+5} and is too small to be a shift between W^{+6} and W^{+4} species.[42, 43]To test for the presence of W^{+4} species an additional set of peaks for the W^{+4} environment were used, which always resulted in poorer fits or the W^{+4} peak heights converging to zero. To calculate the O to W ratio (R$_{O/W}$) and subsequent stoichiometry an average environment of 3 O atoms for each W^{+6} and 2.5 O for W^{+5} was assumed.[44] The atomic % of the W4f peaks were used in equation 2.1:

$$R_{O/W} = \frac{\left(3 \cdot W^{6+} + 2.5 \cdot W^{5+}\right)}{\left(W^{6+} + W^{5+}\right)} \qquad (2.1)$$

To estimate the error in the W:O ratios, the standard deviation between three spots on each sample was used (e.g. ± 0.01).

For some experiments, tungsten oxide growth substrates were used instead of W. To ensure the WO_3 substrate was fully oxidized from the initial W film, the stoichiometry was measured after air annealing using XPS analysis. Figure 2.4 shows that the spectra can be fitting well without introducing a W^{5+} component, indicating a fully oxidized growth substrate.

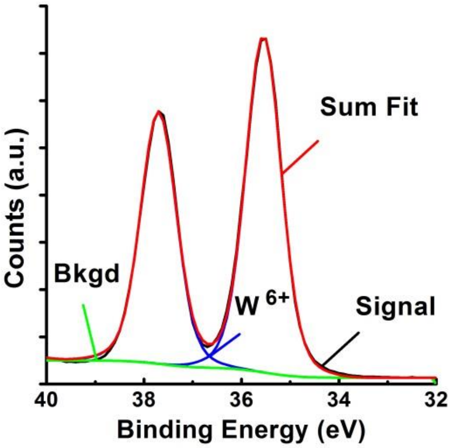

Figure 2.4. XPS analysis of oxidized WO_3 growth substrate.

Results and Discussion

Synthesis and characterization of NWs

Tungsten-oxide NWs were reproducibly synthesized on ~0.25 cm^2 W-coated Si using a low ∆T of 10 ºC and pure Ar process gas. These conditions are similar to those previously reported to result in NW formation.[45-47] Tungsten-oxide vapor species are produced via sublimation of the WO_3 powder source and transported downstream via the carrier gas. We found that 42 µg of material was deposited during the 1 hr growth by directly weighing the sample before and after using a microbalance. This is in contrast with a mass increase of 3 µg (due only to oxidation of the W substrate) for a source-free control. A dense forest of NWs is formed (figure 2.5.A and B). The NW lengths are 0.2 - 1.5 µm and the diameters are 5 - 25 nm. Powder XRD is a common characterization technique but it is difficult to differentiate between oxidized and reduced tungsten oxides due to the lack of long-range order in the NWs. We measured several strong peaks that can be attributed to (010) and (022) reflections in a number of tungsten oxides (figure 2.5.C). The absence of peaks associated with W suggests oxidation of the metallic W substrate during NW growth. The W^{6+} to W^{5+} ratio was measured using XPS and used to calculate an average O to W ratio of 2.88 ± 0.01 (i.e. ~$WO_{2.9}$) indicating the presence of one or more reduced phases (figure 2.5.D).

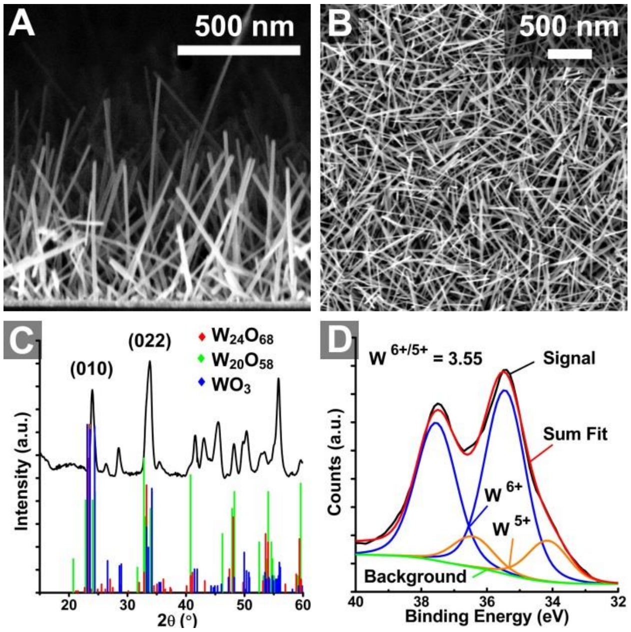

Figure 2.5. Morphology and composition analysis of as-synthesized tungsten-oxide NWs. The SEM images were collected (A) in cross-section and (B) from a top-down perspective. (C) Experimental XRD pattern with reference patterns for possible oxide phases. (D) XPS spectra indicating an overall composition of ~$WO_{2.9}$.

Because oxygen substoichiometry in bulk tungsten oxides leads to extended planar defects, the as-synthesized NWs are also likely contain them. To study these defects, HRTEM and selected-area electron diffraction (SAED) experiments were performed on intact NWs and on FIB-prepared radial NW cross-sections. The d-spacings obtained by analysis of these images are in agreement with NW growth along the (010) direction associated with the family of monoclinic tungsten oxides (figure 2.6). Stacking faults due to O substoichiometry are evident along the growth direction by the mismatched stacking of atomic planes within the body of the NWs (white box figure 2.6). These herring-bone-like linear structures, that often span the entire length of the wire, suggest the presence of multiple superimposed crystallographic domains bounded by planar defects.[36, 48, 49] The large number of defects is observed independent of sample rotation, further suggesting that the linear structures are a result of intersecting defect planes. Evidence of planar defects is also found in SAED patterns (figure 2.6 inset). Streaking of the diffraction spots perpendicular to the NW axis indicates the presence of unequally spaced planar defects parallel to the growth direction.[50] As discussed above these planar defects order along the (102), (103) or (104) directions in bulk samples, which are all perpendicular to the proposed (010) growth direction.

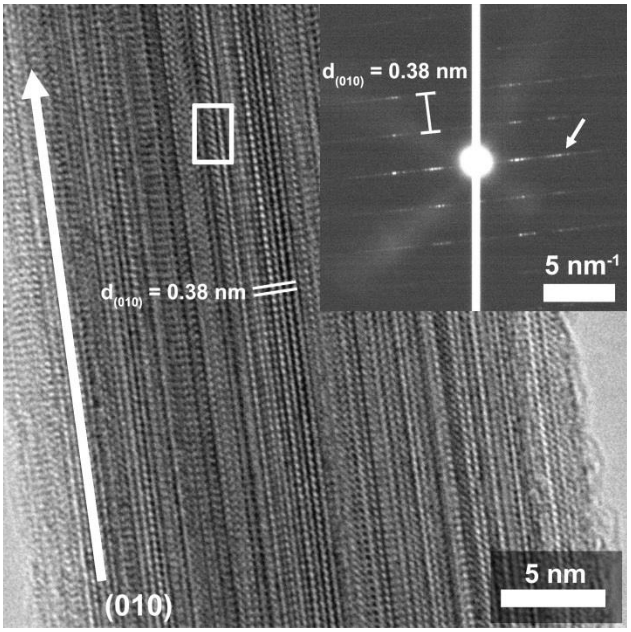

Figure 2.6. Side-on HRTEM image of individual NW containing stacking faults (white box emphasizing one stacking fault) with accompanying SAED pattern (inset) showing characteristic streaking associated with planar defects (white arrow). The labeled lattice spacing of 0.38 nm is consistent with the (010) spacing of the common tungsten oxide phases (eg. $W_{20}O_{58}$, WO_3, ect.).

To probe the behavior of the defect planes within the volume of the NWs and determine how planar defects direct 1D growth, we performed HRTEM on electron transparent radial cross-sections of single NWs prepared by FIB milling. The radial HRTEM cross-sectional image shows a structure comprised of crystalline domains a few nm in size (indicated by the white arrows in figure 2.7) separated by defect planes. The interplanar spacings in both cross-sections are identical within measurement error and consistent with the (200) and (002) spacings of the monoclinic WO_3 structure.

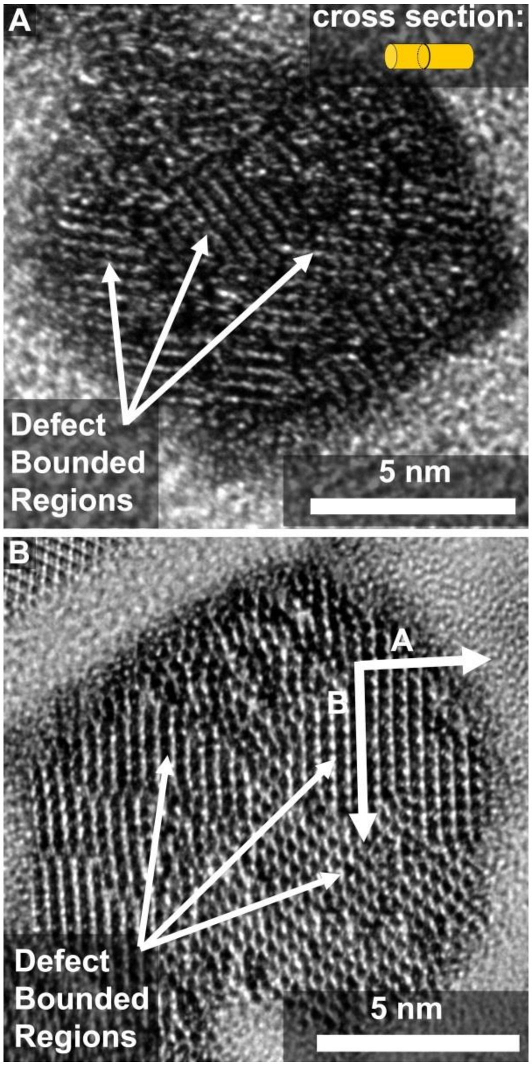

Figure 2.7. Radial cross-sectional HRTEM analysis of single NWs. (A) and (B) show HRTEM images of two different NW cross-sections prepared by FIB milling. The white arrows show regions bounded by planar defects. The arrows A and B indicate (200) and (002) directions with d spacings of 0.38 ± 0.02 nm and 0.39 ± 0.04 nm respectively.

The images suggest that individual NWs contain a variable number of shear planes at a number of intersecting angles. This seemingly random orientation of defects within NWs is likely due to the distribution of defect-nucleation events during the early stages of NW growth. These cross-sectional images support the hypothesis that the bounding defect planes result in an anisotropic energy surface where material is preferentially deposited along the (010) axis.

To determine whether or not the defects originate within the W film, cross sections of NW arrays were prepared by FIB milling (figures 2.8 and 2.3). Fast Fourier transform (FFT) analysis of selected regions show characteristic streaking perpendicular to the NW long axis similar to figure 2.6. This pattern allows us to compare the crystallographic orientation between the wire and the film. Region 1 is of an isolated NW whose FFT shows streaking only perpendicular to the NW axis. As the NW is followed into the substrate, analysis of region 2 indicates that, in addition to planar defects associated with the NW, there are defects running nearly parallel to the Si substrate that can be associated with a similar defect structure in the oxidized W film. Near the base of the NW, the FFT of region 3 still shows some weak streaking associated with defect planes in the NW and thus indicates that the NWs originate well within the substrate film. This suggests that the NW growth originates from defects within the substrate film and not by deposition on a seed layer. There is no indication of metallic W, further showing that the W substrate is oxidized during growth.

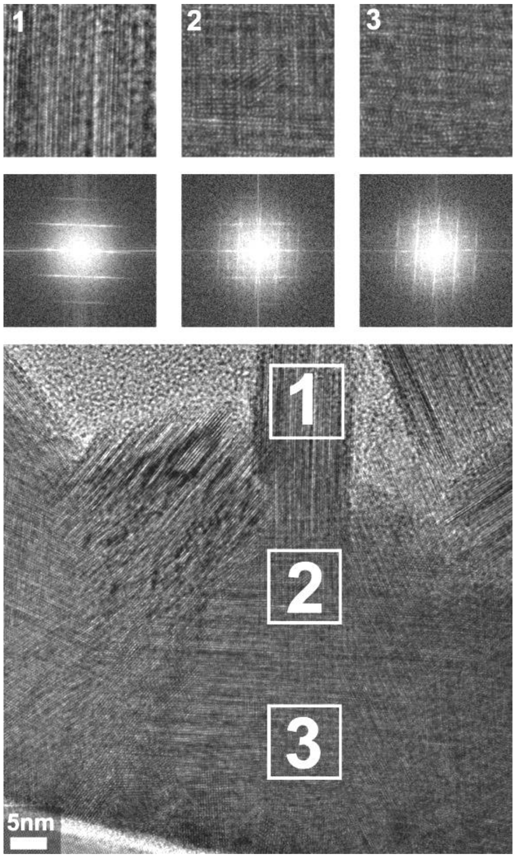

Figure 2.8. HRTEM image and FFT analyses of the base of a NW array showing the origination of the defects from within the substrate film.

Effect of Oxygen Gas on Nanostructure Morphology and Composition

Oxygen is present in all vapor phase tungsten oxide NW syntheses, either from the use of tungsten oxide starting materials, as an intentionally added reactant, or by air leaking into the system.[1, 40, 41, 51] The role of O_2 on the tungsten oxide NW growth and morphology remains poorly understood. O_2 can oxidize reduced tungsten oxides, and therefore can shift the equilibrium toward higher oxides. If the O_2 concentration is sufficiency high during growth, then substoichiometric defects will not form. Therefore NW growth should be inhibited by sufficient O_2. To test this hypothesis, a series of growths with the controlled addition of O_2 gas were performed. During the growth, 5, 2, 1 and 0.1 SCCM of O_2 gas were introduced along with sufficient amounts of Ar to maintain a total flow rate of 10 SCCM. At O_2 partial pressures above 50 mTorr (O_2 flow rates of 1, 2 and 5 SCCM), the NW morphology was completely inhibited and polycrystalline films were observed (figure 2.9.A). These films were found to have an overall composition of WO_3 based on XPS analysis (figure 2.10.A).

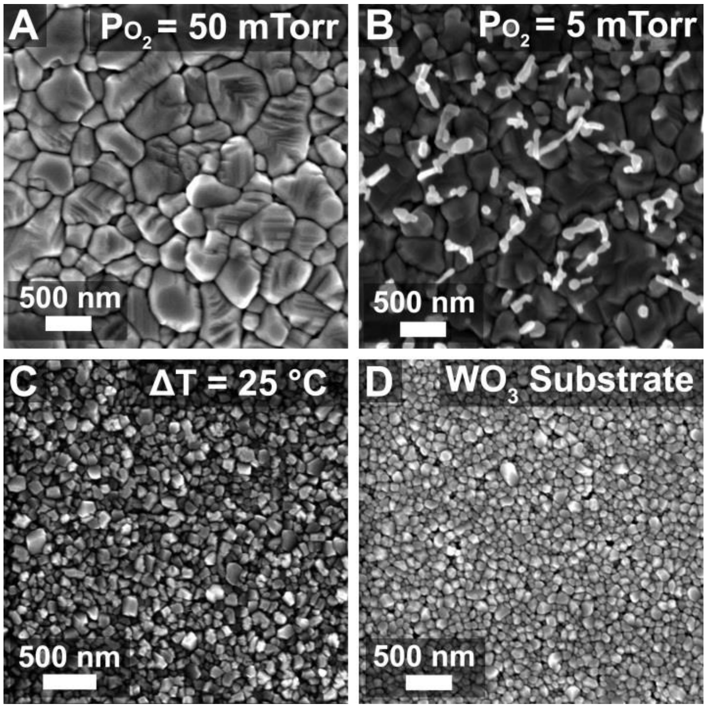

Figure 2.9. SEM micrographs of the tungsten oxide films grown under various conditions. (A) Growth with P_{O2} = 50 mTorr in Ar carrier gas with ΔT = 10 °C. (B) P_{O2} = 5 mTorr O_2 in Ar with ΔT = 10 °C. (C) Growth in pure Ar with ΔT = 25 °C (high supersaturation). (D) Growth on WO_3 substrate in pure Ar with ΔT = 10 °C.

At the lowest O_2 partial pressure of 5 mTorr (obtained at the 0.1 SCCM flow rate), the NW morphology was still inhibited although the presence of some quasi-1D structures are seen (figure 2.9.B). In this case the fraction of W^{5+} was below the XPS detection limit, indicating stoichiometric WO_3 (figure 2.10.B). This result suggests that there is a threshold O_2 activity where the formation of substoichiometric species is suppressed and polycrystalline film morphology is favored over NW growth. It was also observed that if the leak rate into the reactor exceeded ~10^{-3} SCCM, NW growth was similarly inhibited. This illustrates the extreme sensitivity of the tungsten oxygen system to the partial pressure of oxygen gas and is consistent with a model for NW growth based on defect-mediated morphology control.

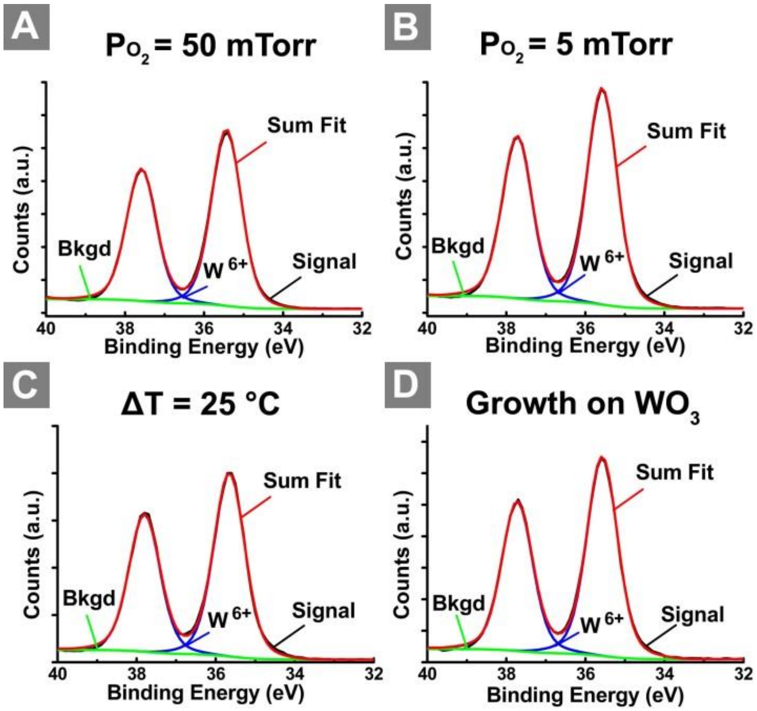

Figure 2.10. XPS analysis of nanostructure composition. (A) Growth with P_{O2} = 50 mTorr in Ar carrier gas. (B) Growth with P_{O2} = 5 mTorr in Ar carrier gas. (C) High supersaturation growth with ΔT = 25 °C. (D) Growth on WO_3 substrate.

XRD analysis of the nanostructured films was performed on a Scintag XDS 2000 diffractometer with an Inel CPS 120 linear detector and a 16 hr collection time. The XRD patterns were background subtracted and smoothed in Inel Peakoc software. Figure 2.11 illustrates the similarity of the XRD patterns even from films with different stoichiometry.

Effect of W Film on Nanowire Growth

The presence of metallic W precursor substrates is a common motif in previous reports of NW growth, with some reports suggesting that W serves as seed nuclei for the NW morphology.[31, 37-41, 46, 51, 52] W is unlikely to directly act as a seed due to significant differences in the cubic tungsten structure and that of monoclinic tungsten oxides. Because metallic W can reduce tungsten oxides,[44, 53] W likely reduces the oxide vapor species to produce the initial substoichiometric tungsten oxide needed for the formation of the planar defects and thus NWs. To test this hypothesis, the reductive capacity of the film was removed by oxidizing the W-film at 500 °C for 30 min in air. XPS of the oxidized film shows that the film is WO_3.

Growth on the WO_3 substrate (under identical conditions to those that yielded nanowires on W) resulted in a polycrystalline film (figure 2.9.D) with the WO_3 composition (figure 2.10.D). In previous NW growth studies where metallic W is not used as a precursor, other reducing agents such as H_2, C_2H_2 or carbon materials are used.[37, 54-56] It is likely these reactants serve a similar role as W by partially reducing tungsten oxide species and initiating the substoichiometric defects necessary for the formation of NWs. They may also act to reduce the O_2 partial pressure in the reactor to levels below the threshold needed to form NWs.

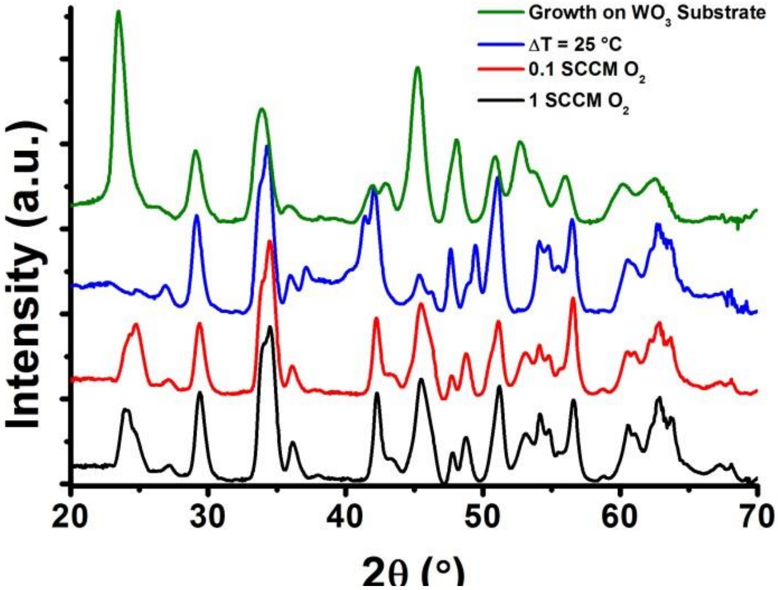

Figure 2.11. XRD analysis of nanostructured tungsten oxide films. Samples characterized include films grown with 1 SCCM O_2 (black), with 0.1 SCCM O_2 (red), under larger supersaturation with $T_{Source} - T_{Sub}$ = 25 °C (blue), and on WO_3 substrate (green).

Effect of Supersaturation on Nanostructure Morphology

If planar defects bounding the NW edges produce the anisotropic energy surface responsible for asymmetric material deposition, it should be possible to overcome such a kinetic barrier. To test this hypothesis, the supersaturation of vapor species, determined by the difference between source and substrate temperature, was increased. NW growth is observed only for a small supersaturation, with a source temperature of 685 °C and substrate temperature of 675 °C, as shown above. When the supersaturation is increased with a source-substrate temperature difference of 25 °C, NWs do not grow. A larger degree of supersaturation corresponds to a greater vapor phase chemical potential, which presumably results in the indiscriminate material deposition responsible for the polycrystalline morphology shown in figure 2.9.C. The increase in material addition is also apparent in an increase in deposition rate to 101 µg over a 1 hr growth. XPS analysis shows no W^{5+} species present, although it is likely that only surface species are measured due to the small sampling depth (~10 nm) of XPS (figure 2.10.C). [57]

At large supersaturation, therefore, the reductive capacity of the metallic W film is overwhelmed by the arriving flux of tungsten oxide and indiscriminate deposition similar to that on the WO_3 film is observed. We note that in tube furnace deposition systems (as used here) the actual supersaturation at the substrate, while dependent on the temperature gradient, is also likely a complex function of the source-substrate distance, gas flow rate, and system pressure. Deposition-evaporation processes also likely occur along the length of the tube walls, which results in a tungsten oxide vapor pressure above the substrate that is likely much less than that above the source. These factors likely explain the large variation in reported temperature gradients and other reaction conditions under which tungsten oxide nanowires have been synthesized previously. [35, 36, 45-47]

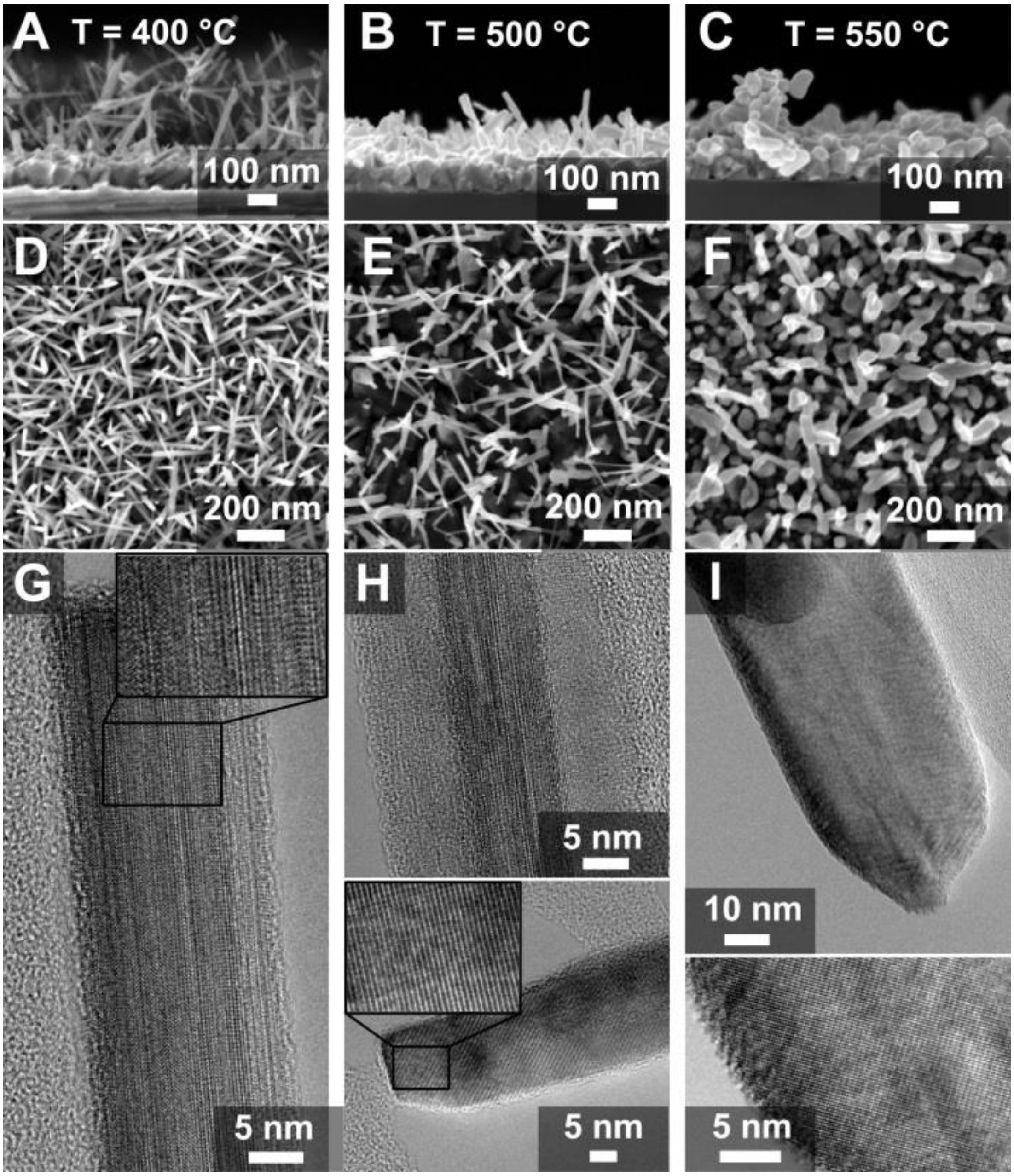

Figure 2.12. SEM and TEM analysis of annealed NWs. (A-C) Cross-sectional and (D-F) plan-view SEM images of NW films annealed in air at 400, 500 and 550 °C for 30 min. (G) NW annealed at 400 °C containing similar defects as unannealed NWs. (H) NW annealed at 500 °C suggesting the oxidation/amorphization of the shell of the nanowire, with the interior still showing defects. (I) NW annealed at 550 °C showing lack of defects.

Effect of NW Oxidation on Defect Concentration and Morphology

For some applications (e.g. water-splitting photoanodes) defect-free fully oxidized WO_3 that retains a 1-D morphology is required. To understand the effect of eliminating the defects on the nanostructure morphology, the NW films were oxidized by annealing at 400, 500 and 550 °C in air for 30 min. After oxidation at 400 °C, the NW morphology is retained with defects still visible in the TEM images (figures 2.12.A, D, G). After annealing at 500 °C, NWs begin to deform and coalesce (figures 2.12.B, E). These NWs have fewer planar defects, with some exhibiting core-shell structures where the core appears to retain the planar defects while the shell appears to largely lack them (figure 2.12.H). NW films oxidized at 550 °C lose most of the 1-D morphology (figures 2.12.C, F) and are crystalline without planar defects.

Composition analysis by XPS is consistent with the TEM analysis. The 400 °C and 500 °C annealed samples had an average stoichiometry of $WO_{2.96}$ and $WO_{2.97}$ with an experimental error of ± 0.01 in the oxygen stoichiometry for all samples (figures 2.14.A and B, and figure 2.15). After annealing at 550 °C and 600 °C, small W^{5+} peaks could still be incorporated in the fits indicating an average composition of $WO_{2.99}$ and $WO_{3.00}$ respectively (figure 2.15.C). However, defects were not observed in the TEM images (figure 2.12.I) and it is difficult to distinguish a low degree of substoichiometry in the TEM. NWs annealed at 600 °C are fully oxidized WO_3 and exhibit a complete collapse of their nanowire morphology (figures 2.13 and 2.14.D).

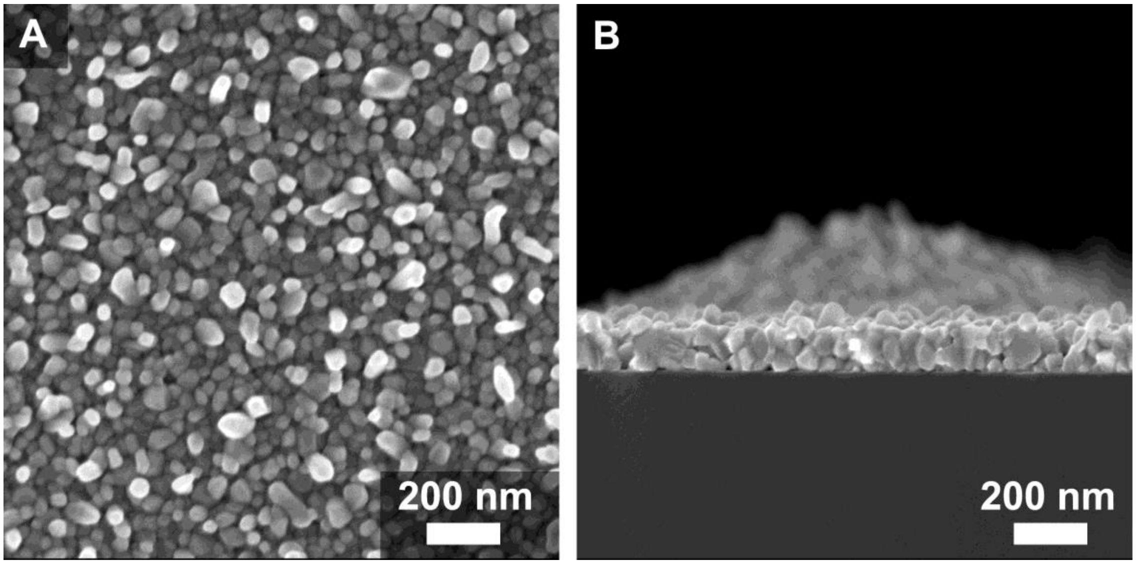

Figure 2.13. SEM images of the NW films annealed at 600 °C. (A) Planar and (B) cross-sectional images showing collapse of 1D nanostructures.

These results indicate that the reincorporation of O into substoichiometric NWs via oxidation in air (to eliminate the planar defects) drives a change from a 1-D nanowire to a particulate morphology. This is consistent with stoichiometric WO_3 lacking sufficiently high surface energy anisotropy to preference 1-D morphology. These results also show that with careful oxidation the defects can be minimized while retaining some 1-D structure.

Additionally, normalized intensities of the experimental XPS spectra are compared in Figure 2.15. The additional signal in the valley between the $W4f_{7/2}$ and $W4f_{5/2}$ peaks and in the shoulders are indicative of W^{+5} species and illustrates the ability to experimentally differentiate between more and less oxidized samples, even at small differences in substoichiometry. For the NW samples annealed at 550 °C and 600 °C, the W^{+5} features are less pronounced, making a significant distinction between substoichiometry difficult.

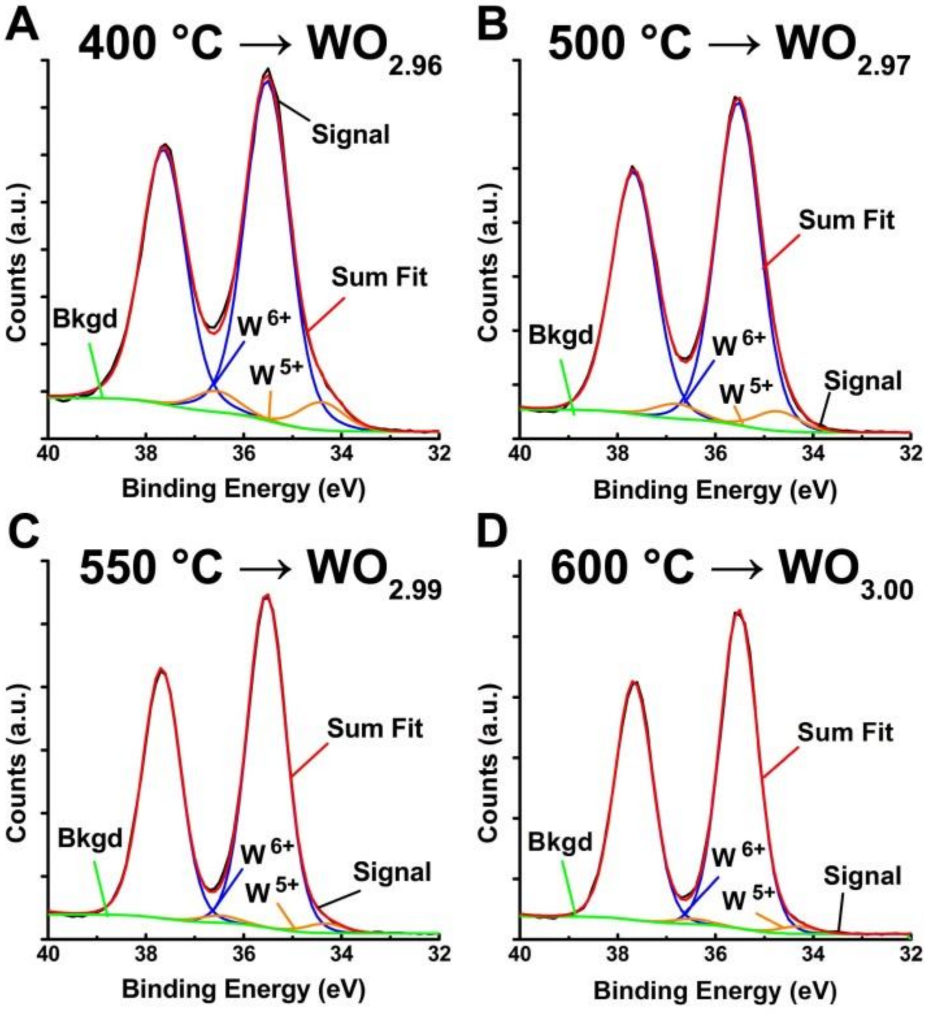

Figure 2.14. Compositional analysis of NWs with annealing temperature with the XPS peak-fitting results listed. The error in the measured stoichiometry is ± 0.01, based on the standard deviation of three independent measurements at different locations for each sample.

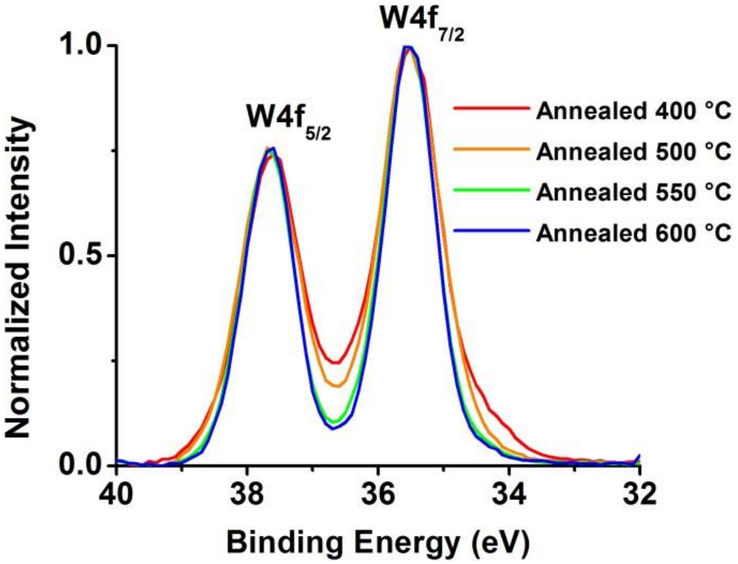

Figure 2.15. Normalized and background subtracted experimental XPS spectra of thermally oxidized NW samples.

NW Growth Model

All the data collected for the various growth regimes as well as the post-growth oxidation are consistent with the following NW growth model. Vapor species sublime and transport to the cooler substrate downstream where deposition occurs (figure 2.16.A). At the temperatures associated with vapor phase growth, metallic tungsten is oxidized by the tungsten oxide vapor species (which are correspondingly reduced) resulting in a defect-rich substoichiometric tungsten oxide film. As more material is deposited, planar defects coalesce and those oriented away from the Si support emerge to form the nascent NW array. Vapor species continue to deposit on the reduced substrate and material addition occurs preferentially along the NW axis with defects propagating along the NW length. When a larger supersaturation is used (figure 2.16.B) polycrystalline growth is observed. The vapor species have a higher chemical potential, deposit at a faster rate, and thus overcome the anisotropic energy surface imposed by the planar defects. Finally, when the reducing capacity of the W film is removed by oxidation or introduction of O_2 reaction gas, planar defects are unable to form and polycrystalline growth is also observed (figure 2.16.C).

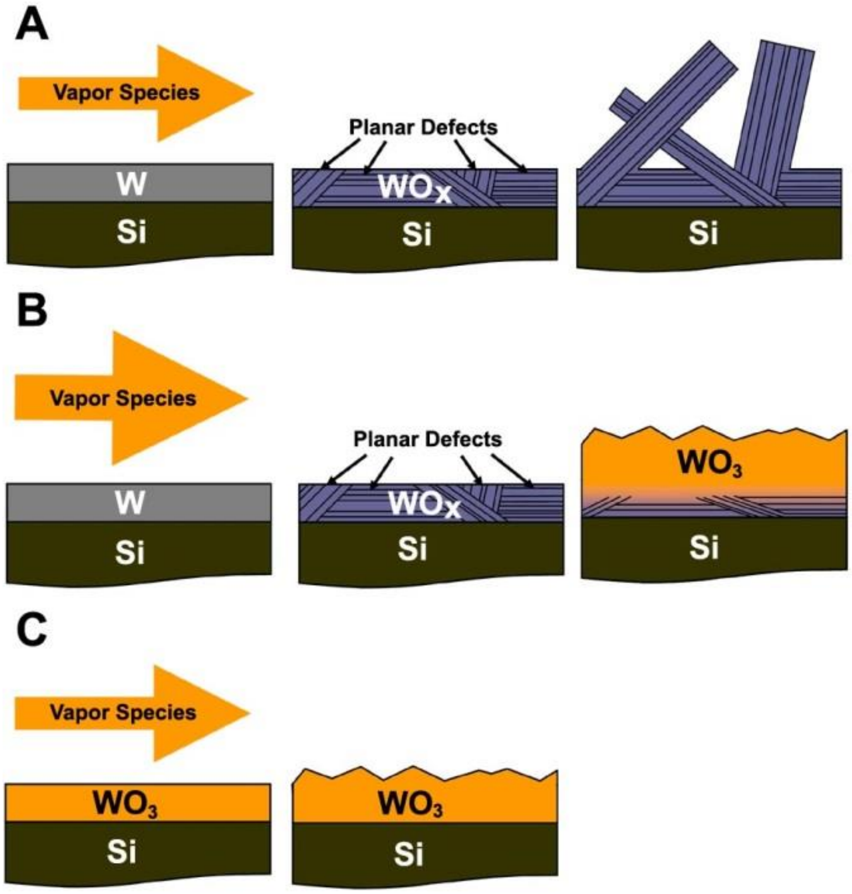

Figure 2.16. Schematic of proposed growth mechanism. (A) NW synthesis illustrating defect-driven growth. (B) Growth of polycrystalline films under increased supersaturation or oxygen partial pressure. (C) Growth of polycrystalline films on WO_3 substrates.

Conclusion and Bridge

We studied the role of substoichiometric planar defects in the formation of tungsten oxide NWs. A simple physical-vapor-deposition route was used to grow the NWs on a metallic W substrate from WO_3 source powder. By directly imaging defects and measuring stoichiometry as a function of key growth parameters, we provide evidence for planar-defect-directed NW growth. We show that the tungsten substrate is needed to reduce vapor species and initiate planar defects. If the reducing capacity of the substrate is removed by oxidizing the tungsten film, defects are not formed and NWs do not grow. Similarly, addition of O_2 prevents the formation of planar defects and NW growth is suppressed. Increasing the supersaturation has a similar effect on morphology by increasing the deposition rate resulting in indiscriminate growth. Upon oxidation in air, the substoichiometric NWs tend to convert to isotropic particulates, implying a significant difference in surface energy between substoichiometric NWs and oxidized crystallites. Taken together, this data shows that composition and morphology are strongly connected in tungsten-oxide nanostructures suggesting that a direct route to stoichiometric WO_3 NWs is not possible using traditional vapor-phase syntheses (i.e. via the mechanisms found here).

The presence of defects in as-synthesized NW structures has implications for proposed applications. Charge carrier recombination occurs at defects in semiconductors, reducing the minority carrier lifetime and thus the efficacy of substoichiometric tungsten oxide NWs as a solar material.[58, 59] There is also evidence that substoichiometry has a negative effect on NW electrochromism.[34] Conversely, substoichiometry may improve ZT, the thermoelectric figure of merit, by increasing the electrical conductivity while simultaneously increasing phonon scattering.[53, 60, 61] Finally, planar defects are found in many transition metal oxides including those of Ti, Nb, Mo and V.[16, 62, 63] The planar-defect-driven mechanism of NW formation presented here may be general in nature and provide insight into the synthesis of other transition metal oxide nanostructures.

In chapters III and IV, device application of tungsten oxide materials is investigated. Chapter III details work towards synthesis, fabrication, and characterization of WO_3 and WO_X single crystals and WO_X NW devices. Chapter IV presents work utilizing the key finding that the common thermal synthetic route of WOX NWs yields substoichiometric and therefore conductive materials. Work towards employing reduced NWs as acid-stable OER catalyst scaffold is presented.

CHAPTER III

TOWARDS TUNSGTEN OXIDE SINGLE CRYSTAL AND NANOWIRE DEVICES

Introduction

It has been well established that nanostructured materials can exhibit significant differences in chemical and physical properties in comparison to those of the bulk material.[1-5] Of particular interest for water splitting systems are micro and nanostructured semiconductor materials including semiconducting metal-oxides.[6-12] Among the many metal-oxide materials investigated for solar water splitting, tungsten oxides have been investigated due to an optical band gap of ~2.6 eV and tendency to form nanowires.[13-16] In order to fully utilize nanostructured oxide devices, a fundamental understanding in the ways in which they differ from the bulk is necessary. In contrast to the numerous reports of nanostructured tungsten oxide materials, there are relatively few reports of tungsten-oxide single-crystals, likely due to the difficulty of crystal growth from a melt caused by tungsten oxide's tendency to sublime. Methods of single crystal growth generally date from the 1960's and involve hermetically sealing oxide powder in a vessel and heating to ~800-1300 °C.[17-20] It is important to note that while tungsten oxide powder is known to be a vivid yellow, in each case the resulting crystals are described as green-blue or blue-black, indicating that such crystals were likely substoichiometric. Such oxygen deficiency is well known to be accompanied by the formation of planar defects through the bulk material.[21, 22] The presence of substoichiometric defects significantly affects the properties of tungsten oxide and therefore it is of great importance to develop synthetic routes to both reduced and fully stoichiometric single crystals. This chapter includes work towards understanding the synthesis of both WO_3 and WO_{3-X} single crystals, as well as the growth of WO_X nanowire arrays on W foil. Additionally it describes progress towards the fabrication of both single crystal and nanowire devices and electrical characterization, in particular efforts to produce ohmic contacts with oxide devices.

Methods

Single Crystal Devices

Tungsten oxide powder was produced by oxidizing high-purity metallic tungsten powder (99.9% 12 µm, Sigma Aldrich) in an alumina crucible at 900 °C overnight. The resulting powder was sealed in ~3 in quartz ampoules, either hermetically, with a ~ 0.2 mm pinhole in one end, or with one side open to ambient. Ampoules were annealed at 1050 °C for 2 weeks after which they were allowed to cool to room temperature. Powder X-ray diffraction (XRD) patterns of the samples were collected on a Philips X’Pert PANalytical X-ray diffractometer by grinding single crystals and adhering the resulting powder to a slide using hydrocarbon grease (Apiezon).To prepare the single crystals, they were first polished followed by thermal deposition of Ti/Au contacts. The polishing method involved imbedding a crystal in mounting wax and using an initial 1200 grit sand paper to generate a level facet, followed by a series of 3, 1, 0.25 and 0.1 micron diamond slurry polishes.

The contacts were produced by masking the polished crystal with a 25µm x 25µm windowed transmission electron microscopy (TEM) grid and thermally evaporating 50 nm of Ti metal to produce an ohmic contact to the WO_3 crystal. While still under vacuum 100 nm of Au was thermally deposited in order to create a protecting layer to prevent the formation of an insulating TiO_2 native oxide from exposure to atmosphere. Electrical characterization was performed using a microprobe station and multimeter to measure current-voltage responses. A diagram of the single crystal device geometry is shown in figure 3.1.

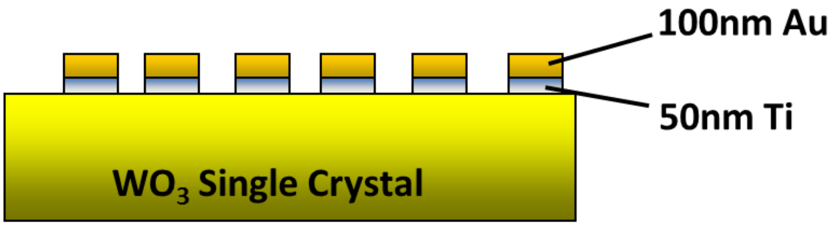

Figure 3.1. Diagram illustrating single crystal device geometry

Nanowire Devices

Nanowires used to make devices were thermally grown by heating metallic tungsten foil (99.98% 0.002”, ESPI Metals, Ashland, OR) to 700 °C in air for 3 hours, after which samples were allowed to cool to room temperature. Nanowire films were characterized by both scanning electron microscopy (SEM) and powder XRD. Scanning micrographs were taken on a Zeiss Ultra-55 with an in-lens secondary electron detector and an accelerating voltage of 3 keV. Nanowires were deposited onto thermally oxidized Si with a ~100 nm SiO_2 insulating oxide. The nanowire substrates were sonicated in ethanol for 30 seconds.

The resulting solution was spun-deposited onto the Si wafer at 4000 rpm for 30 seconds and allowed to dry. Electrical contacts to the NWs were produced using a 50 µm x 50 µm windowed TEM grid as an evaporation mask to thermally deposit 50 nm of Ti followed by 100 nm of Au. A diagram detailing the proposed NW device geometry is shown in figure 3.2.

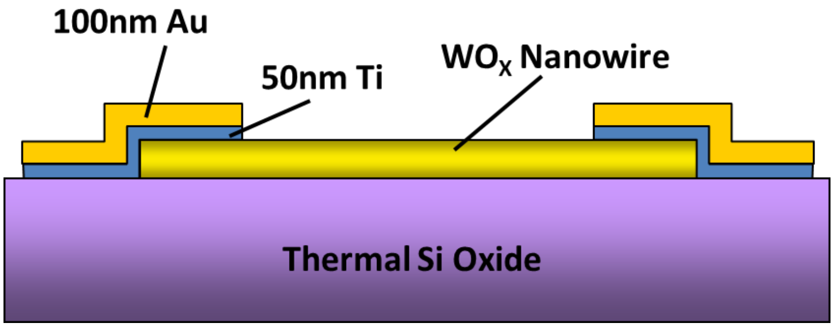

Figure 3.2. Diagram illustrating single nanowire device geometry.

Results and Discussion

Single Crystal Devices

Ampoules in which a pinhole was left open to atmosphere produced stoichiometric yellow WO_3 crystals (figure 3.3.A). Growths using hermetically sealed ampoules produced blue-black WO_{3-x} crystals (figure 3.3.B). Ampoules for which one side was left unsealed yielded no crystals and resulted in significant loss of material to sublimation. Without an excess of oxygen, heating transition metal oxides can exhibit oxygen loss and result in substoichiometry with the oxides of tungsten a particularly dramatic example. The addition of a pinhole to the ampoule allows some degree of oxygen diffusion into the ampoule, preventing the formation of oxygen deficient crystal. Measured patterns of stoichiometric and oxygen deficient single crystals are compared in figure 3.4. It is interesting to note that to the best of the author's knowledge, this is the first example of yellow, fully stoichiometric WO_3 single crystals in literature.

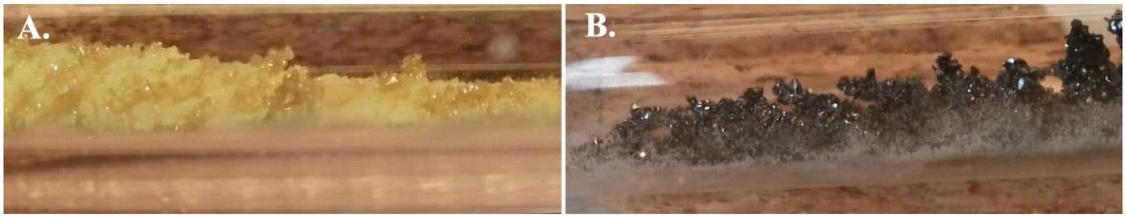

Figure 3.3. Photographs of single crystal results (A) yellow stoichiometric WO_3 single crystals (B) blue-green WO_{3-x} single crystals.

It is important to note that the characterization of oxygen deficient tungsten oxides is difficult due to the wide range of non-stoichiometry exhibited. While the XRD patterns in figure 3.4 imply that the yellow crystals grown in this study are fully stoichiometric, it is possible that a very small degree of oxygen deficiency may still be present, and is in some regards quite likely to facilitate the very small oxygen deficiency thought to impart WO_3 n-type dopants.[23-27] In order to investigate tungsten oxide single crystals and nanowires using EBIC, devices with an ohmic contact and a rectifying contact need to be constructed. Ohmic contacts were attempted first, as a quality ohmic contact is also necessary to determine if a metal-semiconductor contact is rectifying. An illustration of device geometry is depicted in figure 3.1 and an optical microscope image of a polished crystal with Ti/Au contacts is shown in figure 3.5.

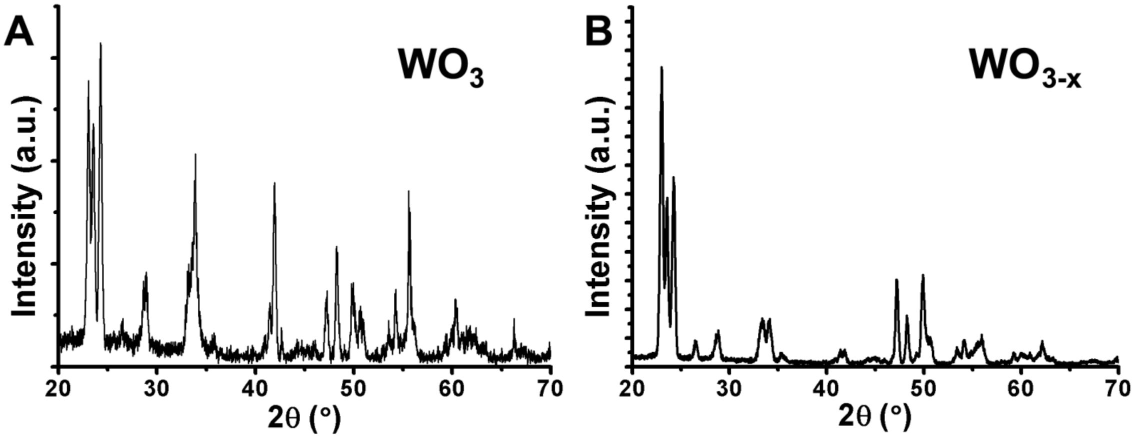

Figure 3.4. Comparison of powder XRD patterns from ground single crystals of (A) yellow stoichiometric WO_3 and (B) blue-black substoichiometric WO_{3-x}

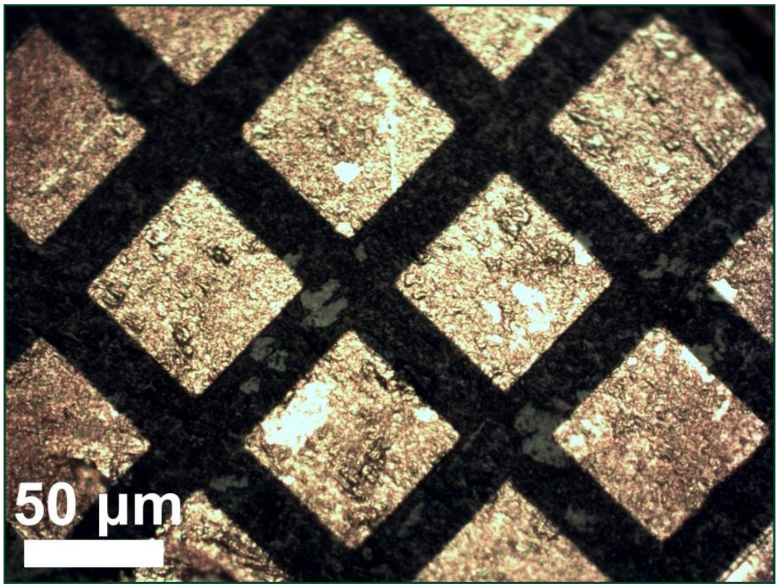

Figure 3.5. WO_3 single crystal device showing polished crystal and 50 µm x 50 µm Ti/Au contacts.

To insure that the contacts produced were ohmic, the current-voltage characteristics of the ingle crystal device were measured. The measured I-V curve is shown in figure 3.6, indicating a contact with a reasonably ohmic response. Although there is some nonlinearity at negative applied potential, the contact is likely sufficient for final devices. In order to produce a functional device for EBIC measurements, a rectifying contact is also required. Au contact devices were attempted but didn’t exhibit diode behavior, though other metals may produce a rectifying junction.

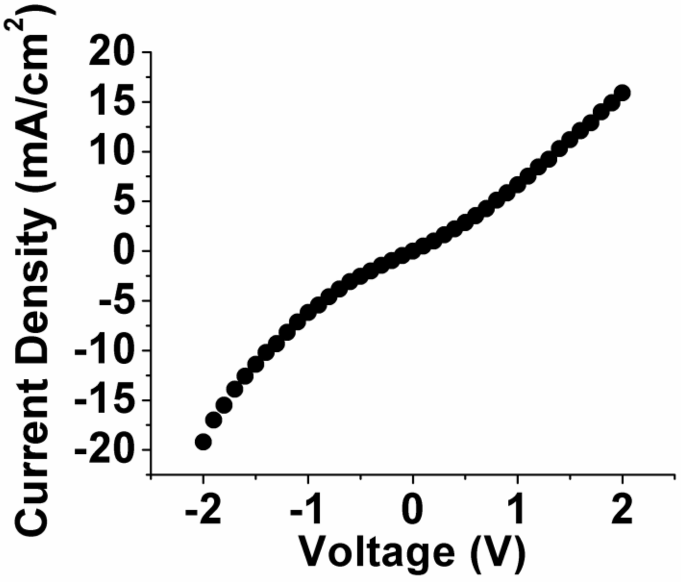

Figure 3.6. Current-voltage measurement of single WO_3 crystal device

Nanowire Devices

As deposited nanowires were ~30 μm long and ~2 μm in diameter as shown in the SEM image in figure 3.7. Nanowires grow as a dense array at a variety of angles from the metallic W substrate (seen at the bottom of the image) and are found to be significantly oxygen deficient when characterized via XRD (figure 3.8).

NW arrays can best be indexed as $W_{18}O_{49}$ ($WO_{2.72}$), though it is important to note that characterizing an ensemble of NWs yields an average XRD pattern. There is likely some variation in the stoichiometry between individual NWs, a fact that confounds phase identification in oxygen deficient systems, particularly those with preferentially oriented nanostructures.

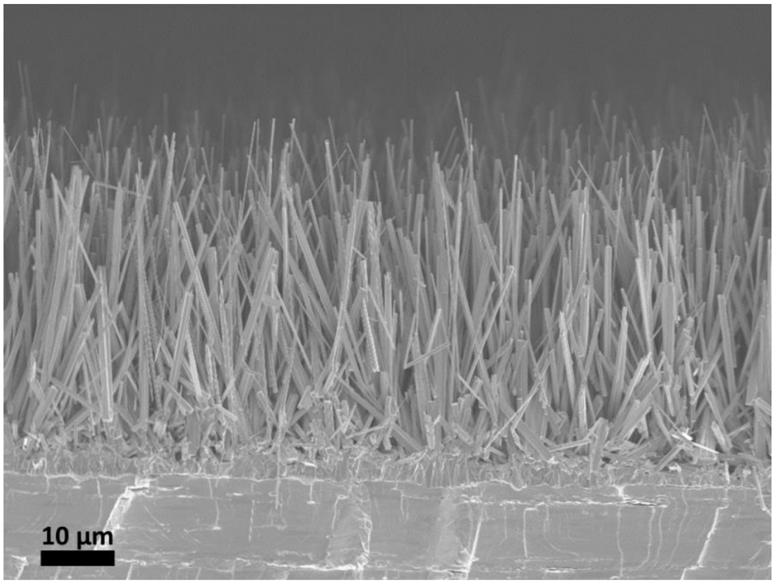

Figure 3.7. Scanning electron micrograph of as-deposited WO_X nanowires grown on W foil.

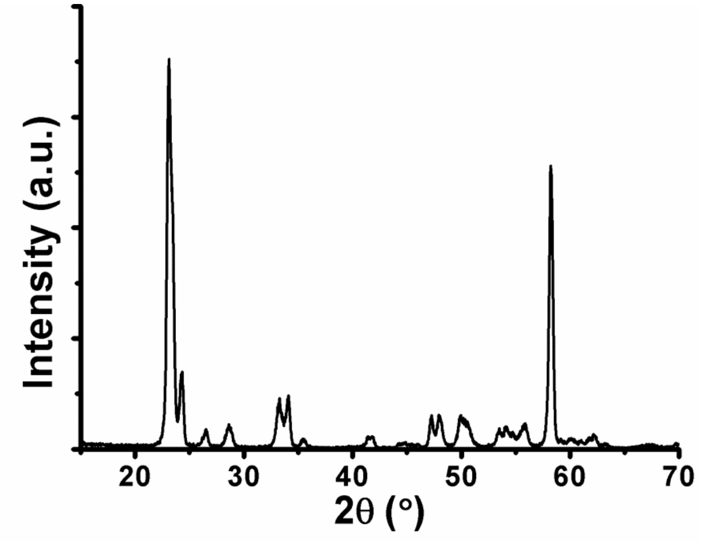

Figure 3.8. XRD pattern of NW array grown on W foil.

NWs can be detached from the substrate by sonicated in EtOH for several minutes. NW suspensions in EtOH are dark blue-black and can be deposited using a number of solution methods. Drop casting NW suspensions on SiO_2 substrates result a density of NWs not suitable for device fabrication due to overlapping and bundling of individual wires, presumably caused by dewetting processes. By spin depositing the suspension, an effective distribution of NWs can be produced for masking and subsequent deposition of contacts as shown in the optical image in figure 3.9. After masking and evaporation of Ti/Au contacts, samples were imaged via optical microscopy as seen in figure 3.10. NWs that were found to be bridging two contacts were chosen as devices for current-voltage characterization.

Figure 3.9. Optical image (100x magnification) of tungsten oxide nanowires deposited on SiO_2 substrate from EtOH suspension.

An optical image of a representative nanowire device is shown in figure 3.10. The NWs span a gap of ~25 μm between the two Ti/Au contacts. The I-V measurement in figure 3.11 demonstrates the ability to make nanowire contacts with an ohmic response. For both the single crystal and nanowire systems, creating effective rectifying contacts remains an important step in device preparation for EBIC studies.

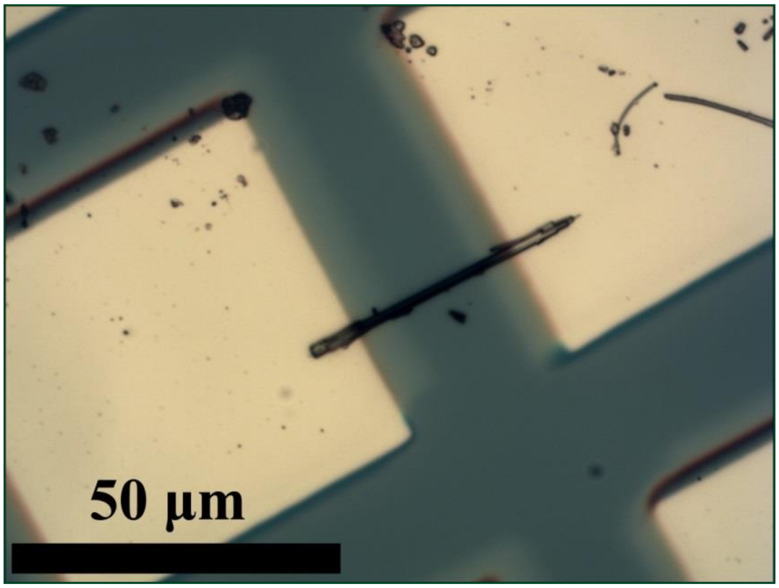

Figure 3.10. WO_X single nanowire device with 50 µm x 50 µm Ti/Au contacts.

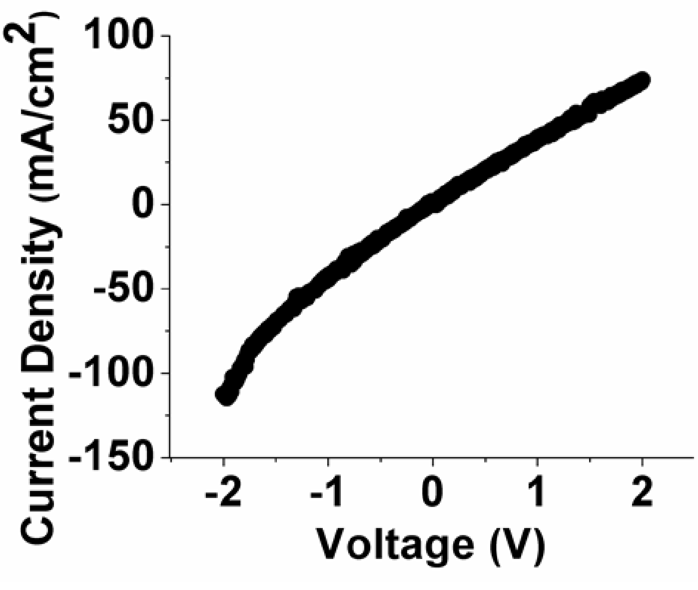

Figure 3.11. Current-voltage measurement of WO_X single nanowire device.

Conclusions and Bridge

The present work demonstrates progress towards both single crystal and individual nanowire devices for advanced characterization (e.g. EBIC). Both stoichiometric and oxygen deficient single crystal synthetic routes were developed. Polished crystals were patterned with Ti/Au contacts and their current-voltage behavior measured. Devices with Ti contacts were found to be ohmic. Additionally, ~30 µm long NWs were synthesized from a metallic W foil substrate and a deposition method for well distributed NWs on insulating substrates were developed. Additionally, single NW devices were fabricated by deposition of Ti/Au contacts and were found to exhibit a ohmic response. In order to realize the initial goal of rectifying devices, additional work is necessary to optimize metal-crystal/NW contacts. In particular, a method for dissimilar metallic contacts on the same device will need to be developed, likely utilizing electron beam lithographic techniques. In the following chapter, work toward using conductive tungsten oxide nanowire arrays is presented.

CHAPTER IV

TOWARDS NANOSTRUCTURED TUNGSTEN OXIDE CONDUCTIVE CATALYST SUPPORTS FOR OXYGEN EVOLUTION IN ACIDIC MEDIA

Introduction

Solar water splitting is a promising route to store solar energy through the generation of hydrogen gas.[1-3] The overall reaction for water splitting entails the evolution of both hydrogen and oxygen as shown in the half-reaction equations 4.1 and 4.2 for acidic media.

OER $$2\mathrm{H}_2O(l) \rightarrow O_2(g) + 4H^+(aq) + 4e^- \quad (4.1)$$

HER $$2H^+(aq) + 2e^- \rightarrow H_2(g) \quad (4.2)$$

The oxygen evolution reaction (OER) suffers from a significant kinetic over potential which inhibits the overall efficiency of water splitting, which could be in part alleviated with the presence of a catalyst.[4-6] Despite decades of research, few OER catalysts have been demonstrated that are stable in acidic media under the oxidizing conditions that occur during OER.[7-10] The highest acidic OER activity is exhibited by IrO_X, which is a rare, precious metal with a low volume annual production of only ~3000 kg. [11]

By utilizing a surface are conductive scaffold and sub-monolayer equivalent of IrO_X catalyst (figure 4.1), significant progress could be made toward a scalable OER catalyst system for acidic media. IrO_X can be derived from electrochemical oxidation of metallic Ir, which can be deposited by physical vapor deposition methods such as electron beam evaporation and sputtering. A high surface area conductive substrate also allows the effective utilization of electrochemical deposition of IrO_X nanoparticles.[12] In particular, the tungsten oxide system has been shown to readily form nanowire arrays.[13-15] Additionally, tungsten oxide is thought to be stable is strongly acidic conditions as indicated in the Pourbaix diagram in figure 4.2.[16, 17]

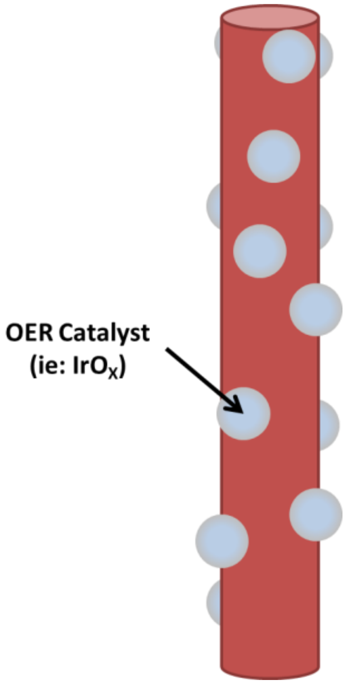

Figure 4.1. Illustration of catalyst loaded nanowire

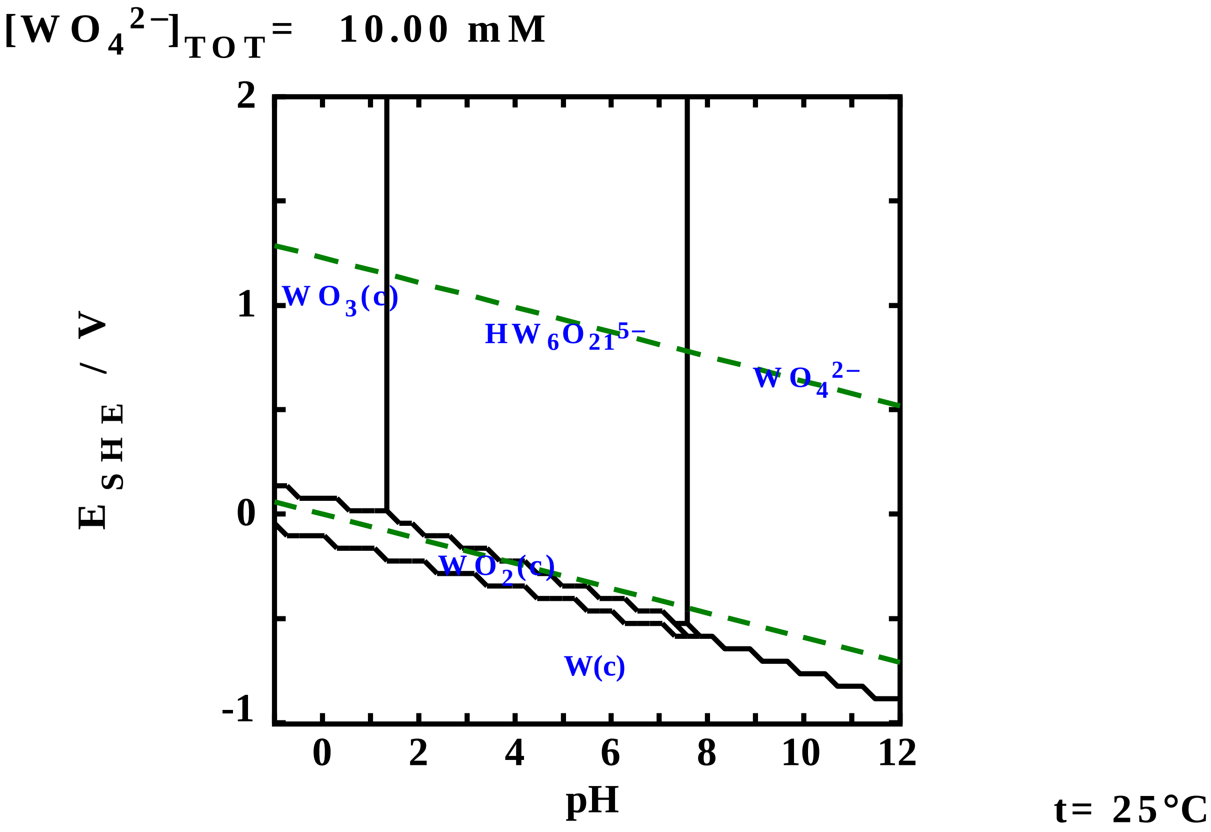

Figure 4.2. EH-pH diagram of tungsten oxide system demonstrating thermodynamic stability in acidic media

Nanowires grown thermally tend to form via a planar defect propagation mechanism and were found to be oxygen deficient (figure 4.3).[18] Substoichiometric tungsten oxides are known to be conductive and could therefore serve as an electrochemical substrate.[19-21] Additionally WO_X materials exhibit wide bandgaps of ~2.6 eV, making them viable for incorporation on planar photo-active systems. In the present work, results as to the viability of tungsten oxide nanowire systems as an acid stable scaffold support for IrO_X OER catalysts are reported.

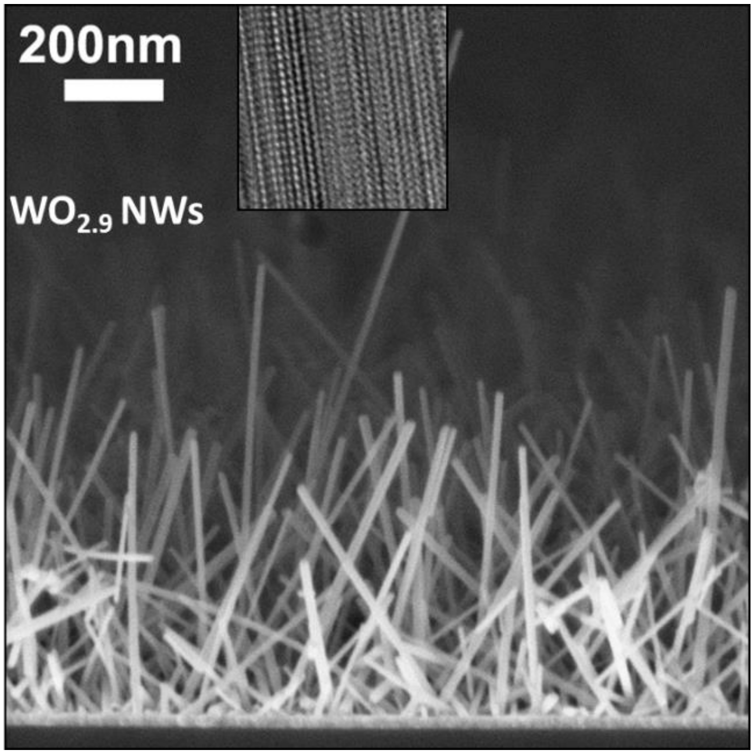

Figure 4.3. Scanning and transmission electron micrographs of WO_X nanowire array

Methods

Reduced tungsten oxide nanowires were synthesized as previously reported.[18] Briefly, nanowires are grown by sublimating WO_3 powder which is transported by Ar carrier gas and deposited on a metallic W coated Si substrate. The source and substrate are heated to 685 °C and 675 °C, respectively, for 1 h after which the samples were allowed to cool to room temperature.

The acid stability of NW arrays was investigated through an accelerated aging study in hot H_2SO_4. As-deposited NWs were immersed in 1 M H_2SO_4 at 60 °C for ~16 h after which samples were remove, gently rinsed with H_2O and allowed to dry before characterization with SEM.

The ability of NWs to withstand the anodic potentials present during OER is important for the application of NW arrays as scaffold materials and was investigated by fabricating a NW substrate electrode. As-deposited NW substrates were cleaved to produce a ~5 mm x 5 mm sample on the back of which was formed a ohmic contact to the n^{++} Si by scoring with an InGa eutectic coated diamond scribe. A tinned copper contact wire was bonded to this contact with silver paint (0.0002 Ωcm volume resistivity, Ted Pella) and allowed to dry. The electrode was then attached to a borosilicate glass tube with epoxy and the wire encased to prevent contact with solution. The electrode geometry is illustrated in figure 4.4.

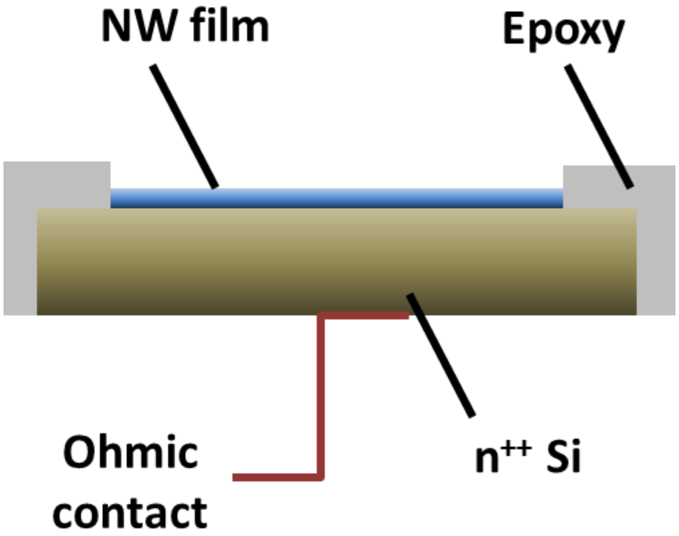

Figure 4.4. Diagram illustrating NW electrode geometry for electrochemical experiments

Samples were anodized at 1.5 V vs SCE in 1 M high purity H_2SO_4 electrolyte (>95% TraceSELECT, Fluka) for 16 h using a 3-electrode setup as illustrated in figure 4.5. After anodization, samples were removed from solution, rinsed with H_2O and allowed to dry before SEM characterization.

Catalyst/scaffold devices were fabricated by coating as-deposited NW arrays with ~30 nm metallic Ir (99.9% 3-6 mm pieces, Kurt J. Lesker) via electron beam evaporation. Electrodes were made using a similar method as described for anodization experiments above. Metallic Ir was electrochemically converted to IrO_X. Samples were cycled 200 times from -0.5 to 1.5 V vs SCE at 50 mV/s in high purity H_2SO_4 while bubbling high purity O_2 (Air Liquide America Specialty Gases) and rapid stirring.

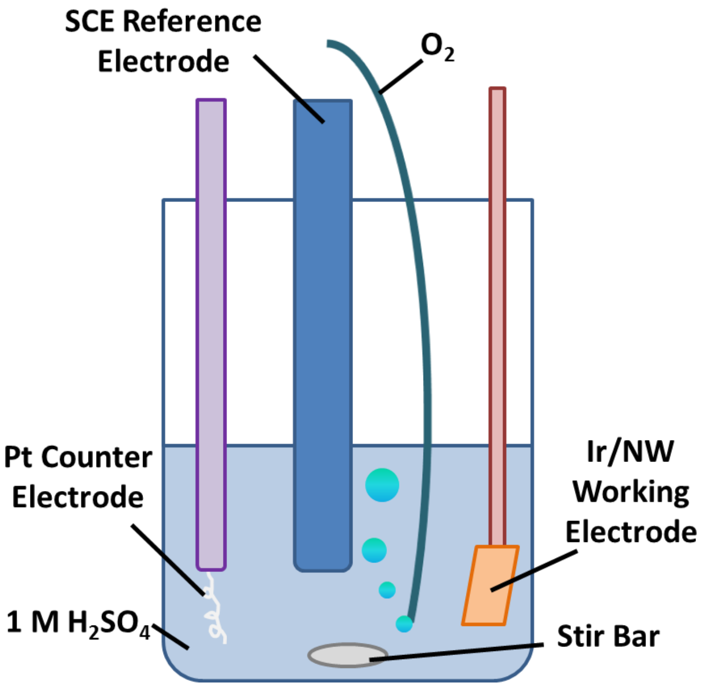

Figure 4.5. Three electrode cell for electrochemical experiments

Planar Ir samples were similarly cycled for comparison to Ir/NW devices. 50 nm metallic Ir was deposited with Ti (99.995% pellets, Kurt J. Lesker) as an adhesion layer on glass slides. Electrodes were fabricated by contacting a ~ 1 cm^2 surface with silver paint followed by encapsulation in epoxy.

Nanowire samples were imaged using a Zeiss Ultra-55 with an in-lens secondary electron detector and an accelerating voltage of 3 keV.

Results and Discussion

As-deposited NWs were ~10-20 nm in diameter and ~0.5-1 μm in length as shown in figure 4.6.A. NW arrays maintain these dimensions after aging in 1 M H_2SO_4 at 60 °C for 16 h as indicated by the micrograph in figure 4.6.B.

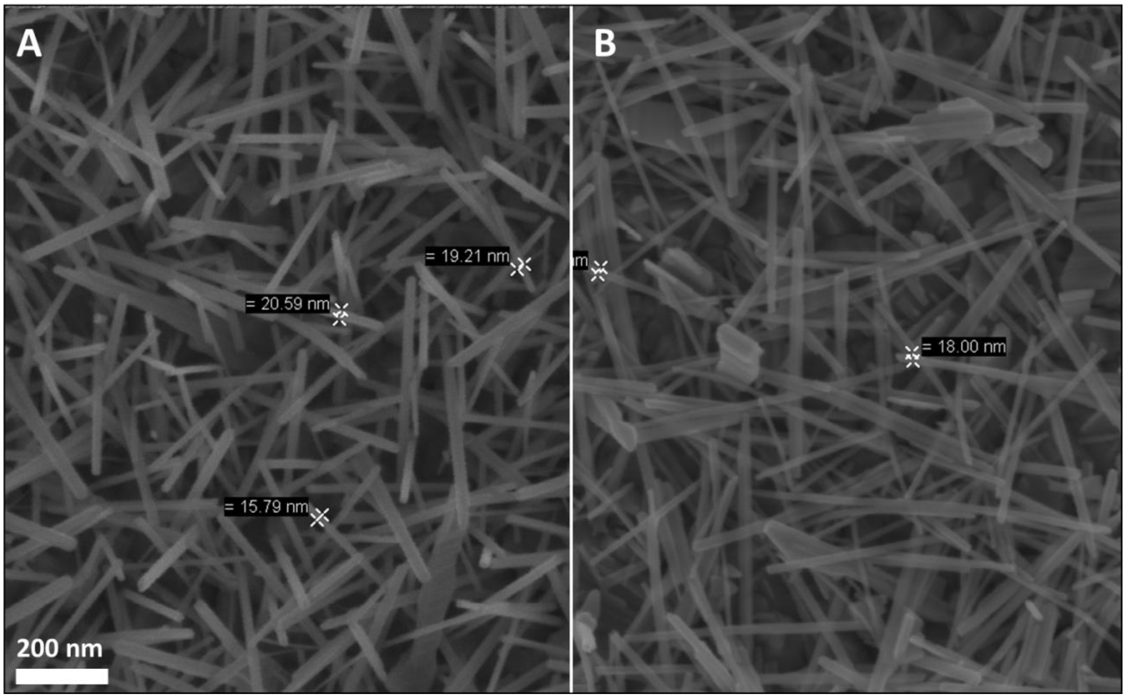

Figure 4.6. Scanning electron micrographs of as-deposited NWs (A) and after 16 h in 60 °C 1 M H_2SO_4 (B).

NWs were also shown to be stable at oxidizing potentials in acidic media. Figure 4.7 shows a post-anodization NW array. NWs held at 1.5 V vs SCE in 1 M H_2SO_4 exhibited no degradation after 16 h. This key result suggests that WO_X nanowires are indeed a promising scaffold system for acid OER.

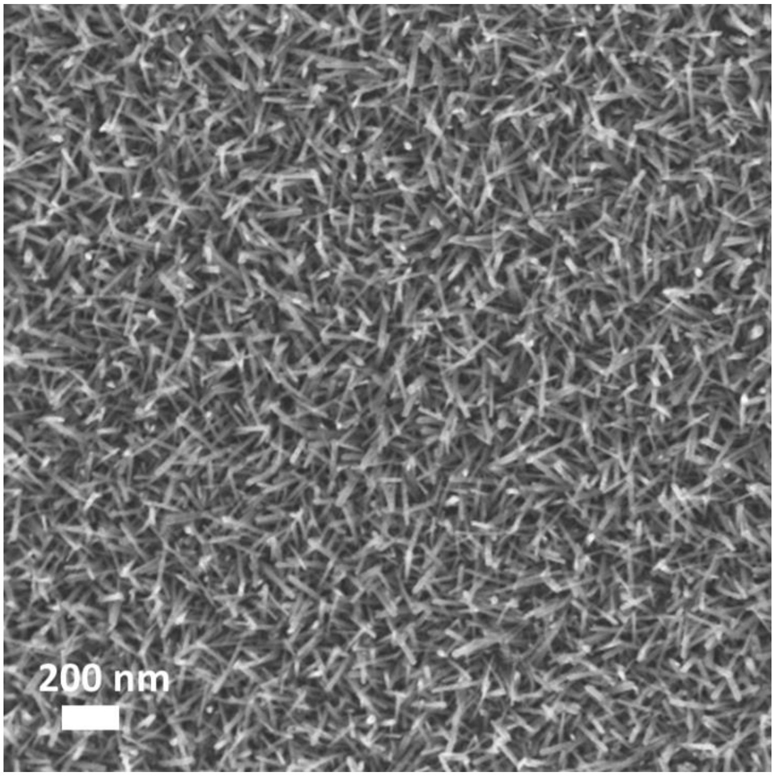

Figure 4.7. Micrograph of NW array after held at 1.5 V vs SCE for 16 h in 1 M H_2SO_4

The electrochemical conversion of metallic Ir to IrO_X (the catalytically active species) has been used to generate OER catalysts films. Figure 4.8 shows the conversion from metallic Ir to IrO_X through cycling between oxidizing and reducing conditions several hundred times on a control planar substrate. As cycling progresses, the OER current can be seen to increase with additional cycling. It is also interesting to note the decrease in HER current as the metallic Ir is oxidized.

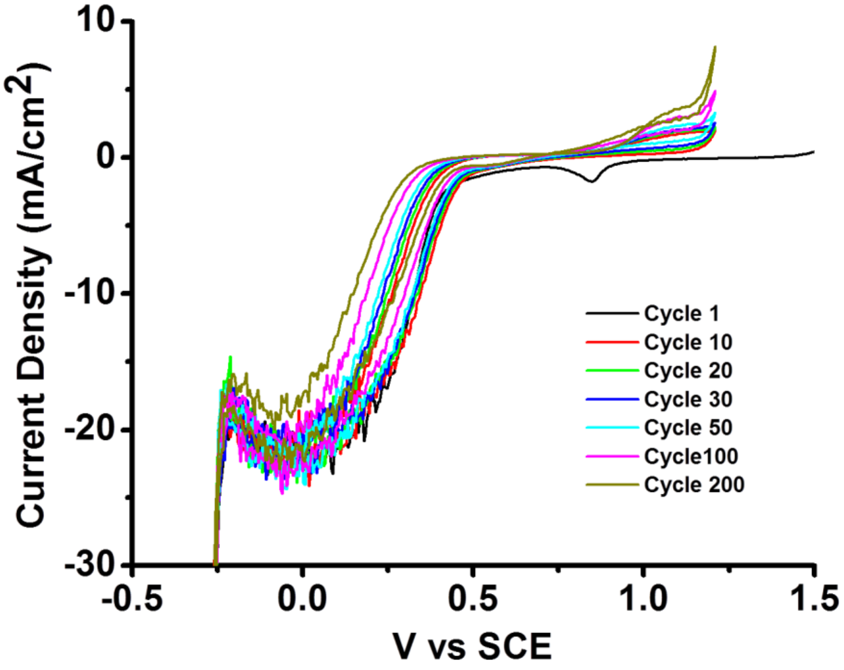

Figure 4.8. Electrochemical conversion of metallic Ir to IrO_X OER catalyst

Electron beam deposited Ir (~30 nm) on a NW array can be seen in the micrograph in figure 4.9. Although the NWs as deposited were ~ 10-20 nm in diameter the resulting structures post-deposition indicate a diameter of ~ 100 nm.

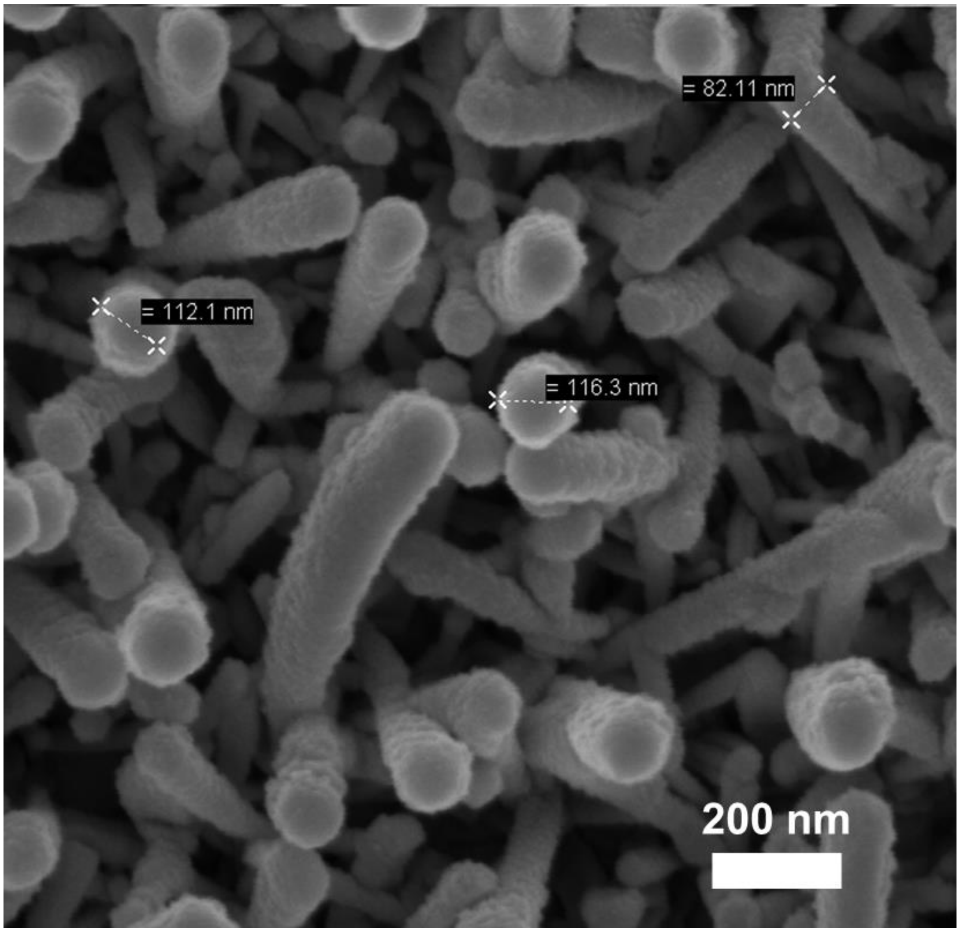

Figure 4.9. Micrograph of ~30 nm metallic Ir as-deposited on WO_X NW scaffold

Electrochemically conditioned Ir:NW electrodes exhibited an initial increase in OER activity when cycled ~10 times (figure 4.10). After ~20 cycles, electrodes began to degrade as indicated in the decrease in OER activity. Scaffold arrays were significantly degraded after ~30 cycles and exhibited similar response through 200 cycles.

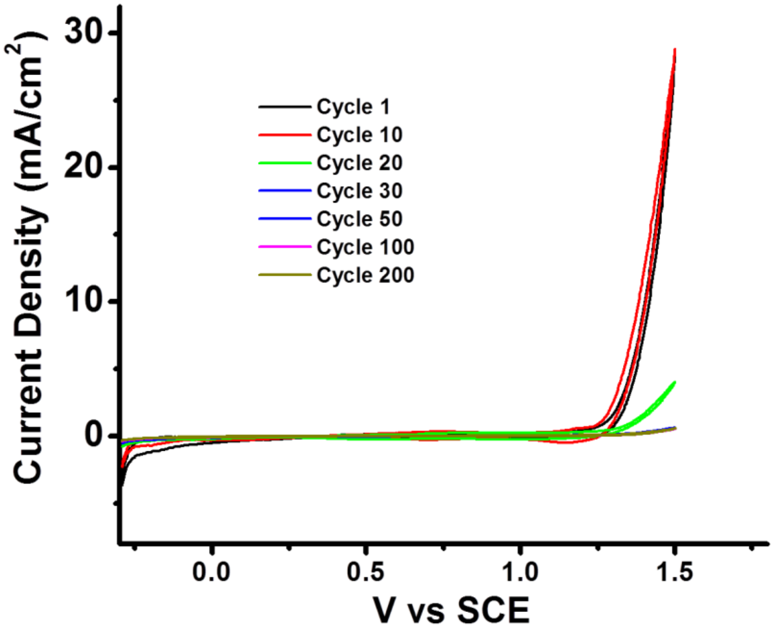

Figure 4.10. Electrochemical cycling of Ir:NW scaffold in 1 M H_2SO_4

An SEM image of a post-200 cycle NW array is shown in figure 4.11. It is clear that the NW morphology is substantially degraded after electrochemical cycling, with the electrode exhibiting a matted surface. It is possible that NWs are degraded during the Ir electron beam deposition. This may explain the apparent disparity in NW diameter before and after evaporation observed in figures 4.9 and 4.11. Alternatively, the morphological collapse could be a result of the electrochemical cycling itself. Even in acidic conditions, tungsten oxide is not thermodynamically stable at reducing potentials, and a WO_2 phase predominates (figure 4.2). By utilizing an alternative synthetic method for IrO_X decorated NWs, particularly deposition from nanoparticle solutions, these challenges could be overcome.

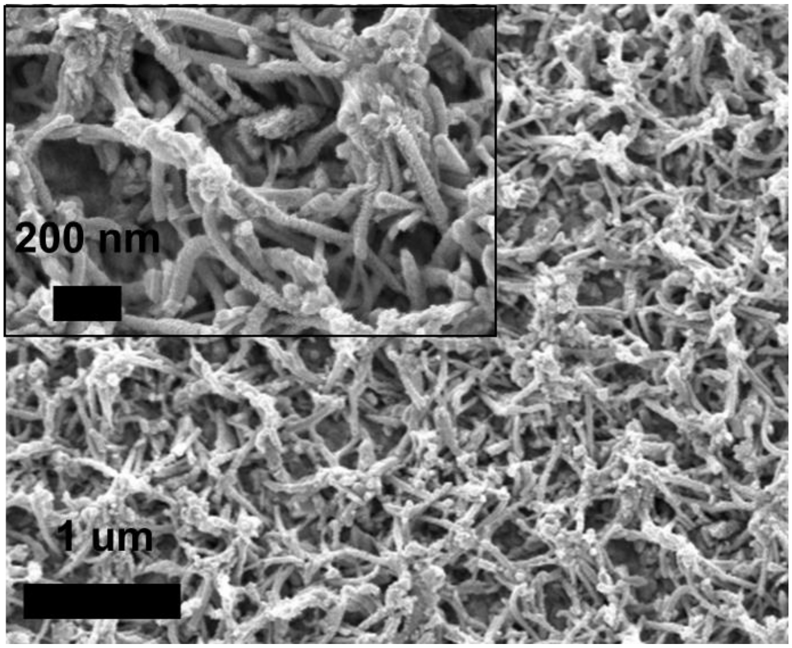

Figure 4.11. Micrograph of a collapsed post-electrochemically conditioned IrO_X:NW scaffold

Conclusions and Bridge

In the present work it was shown that tungsten oxide nanowires stable during accelerated aging studies at elevated temperatures in acidic media. Also, NW arrays maintain their high surface area morphology after being exposed to the oxidation potentials found during OER for extended periods. These key results imply that WO_X NWs may be suitable for use as a conductive scaffold for OER catalysis in acid. Additionally, decoration with metallic Ir and subsequent electrochemical conversion to IrO_X on NWs was attempted. Although the electrochemical conditioning resulted in the partial collapse of the NW morphology, other methods of catalyst decoration could still be used, such as electrochemical deposition of IrO_X nanoparticles synthesized via the method described by Mallouk et al.[12]

In order to meet the demands of an inexpensive and efficient solar water splitting device, it is likely that multiple approaches to OER need to be taken. In particular, OER catalysts that function in neutral or near-neutral are promising from a material compatibility standpoint. In the following chapter work is presented elucidating the effect of incidental Fe on the activity Ni-borate catalysts in near-neutral pH. Additionally, the rational design of Fe:Ni-borate catalysts is discussed.

CHAPTER V

CONTRIBUTIONS TO ACTIVITY ENHANCEMENT VIA Fe INCORPORATION IN Ni(OXY)HYDROXIDE/BORATE CATALYSTS FOR NEAR-NEUTRAL pH OXYGEN EVOLUTION

Portions of this chapter were previously published as Smith, A. M.; Trotochaud, L.; Burke, M. S.; Boettcher, S. W. "Contributions to Activity Enhancement via Fe Incorporation in Ni-(oxy)hydroxide/Borate Catalysts for Near-Neutral pH Oxygen Evolution" in Chemical Communications, 2015, **51**, 5261-5263. A.M.S. wrote the publication, synthesized samples and performed characterization. L.T. developed many of the methods used. M.S.B. helped with XPS collection and analysis. S.W.B. provided editorial assistance and served as principle investigator.

Introduction

The need for solar energy storage has been thoroughly reported.[1-3] Electrolytic and photoelectrochemical water splitting to produce hydrogen fuel and oxygen are two routes to scalable energy storage. Both methods could benefit from improvements in oxygen evolution reaction (OER) catalysts, as the OER suffers from substantial overpotential losses (300-400 mV) compared to the hydrogen evolution reaction (<50 mV).[3-5] Despite the considerable number of reported OER catalysts, identifying the catalytically relevant species/active-sites and increasing activity through rational design remain challenges/opportunities.[6-11]

Ni- based catalysts have been shown to be among the most active in basic conditions.[7, 12-16] Although Ni-based catalysts have been investigated for some time, Trotochaud et. al. recently showed that the incidental incorporation of Fe impurities from electrolytes are in fact completely responsible for the high catalytic performance of NiOOH in base, with Fe-free NiOOH having very poor electrocatalytic activity.[13, 17] Incidental Fe incorporation and subsequent increase in OER activity was observed by Corrigan in the 1980s for the $Ni(OH)_2$/NiOOH system.[18, 19] Louie *et. al.* also studied mixed Ni–Fe-(oxy)hydroxide films and found that the activity was maximized and relatively constant for 10–60% Fe.[20] Of potential interest for OER catalysts integrated with semiconductors in photochemical water-splitting devices are those that function in near-neutral conditions, as they may offer more flexibility in the semiconductor materials used which must also be stable in the electrolyte.[21] Ni-(oxy)hydroxide/borate (NiO_x-B_i) catalysts were reported and studied by Nocera and coworkers which function in near-neutral pH of ~9 and have reasonably high activity. These films were locally comprised of NiOOH structural fragments and the catalytic activity was observed to increase after anodic conditioning. The improvement was attributed to changes in Ni oxidation state and film structure.[22-24]

Here we study the effect of incidental and intentional Fe incorporation on NiO_x-B_i catalyst film activity in near-neutral borate buffers. We show that both incidental Fe incorporation via anodic conditioning in a borate buffer and intentional Fe co-deposition result in increases in OER activity compared to as-prepared catalyst films. Additionally, when NiO_x-B_i films are conditioned under rigorously Fe-free conditions, no increase in catalytic activity is observed implying that Fe is critical for film activation.

Methods

Film Deposition

NiO_x-B_i films were synthesized via anodic electrodeposition as reported previously.[22, 23] Catalyst films were electrodeposited from 0.4 mM $Ni(NO_3)_2$ solutions buffered to pH = 9.2 with a 0.1 M borate supporting electrolyte on gold-coated glass electrodes at 0.909 V vs. SCE (not corrected for series resistance) in a three electrode configuration without stirring. The electrodes were ~ 1 cm^2 in area. Prior to deposition, solutions were purged with N_2 for ~15 min and subsequently filtered with 0.45 um syringe filter. Borate buffer for deposition was produced from 0.1 M boric acid, respectively (99% purity ACS grade with < 10 ppm Fe for low Fe and Fe-free experiments, or 99.99% purity with < 100 ppm Fe for high Fe experiments) and adjusted to pH 9.2 with KOH (semiconductor grade with < 0.2 ppm Fe for "low Fe and Fe-free" experiments and ACS grade with < 10 ppm Fe for high Fe experiments). All electrochemical experiments were performed with a Biologic SP-200 potentiostat

Ni-Fe-(oxy)hydroxide)/borate co-deposited samples were similarly synthesized from buffered deposition solutions comprised of 0.36 mM $Ni(NO_3)_2$ and 0.04 mM $FeCl_2$ with 0.1 M borate buffer as supporting electrolyte (figures 5.1 and 5.2). Ni/borate deposition solutions were purged with N_2 for 15 min before the addition of Fe solutions, after which the combined Ni/Fe solutions were purged for an additional ~10 min and subsequently filtered. Purging was to prevent dissolved O_2 from oxidizing Fe^{2+} to Fe^{3+} which leads to the precipitation of FeOOH in the deposition solution. Film loading was also measured using quartz-crystal microgravity measurements (figure 5.3).

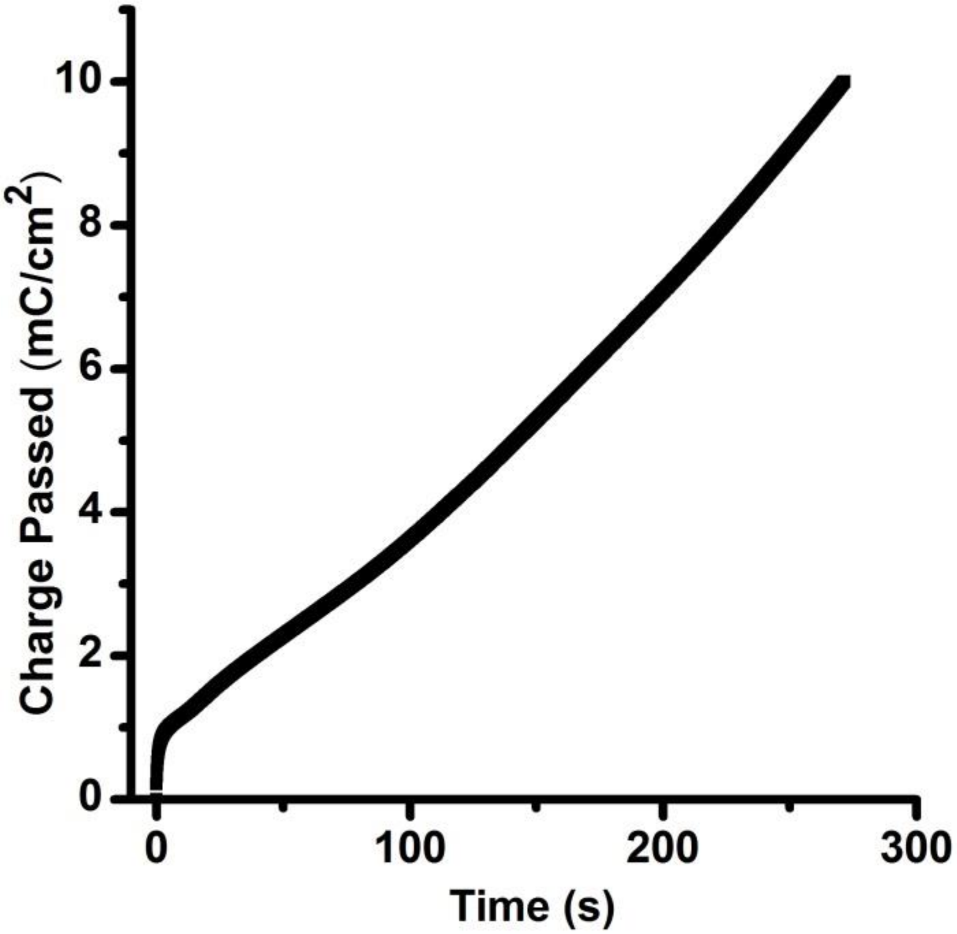

Figure 5.1. Representative charge-time trace of Ni-(oxy)hydroxide/borate 10 mC/cm^2 anodic deposition.

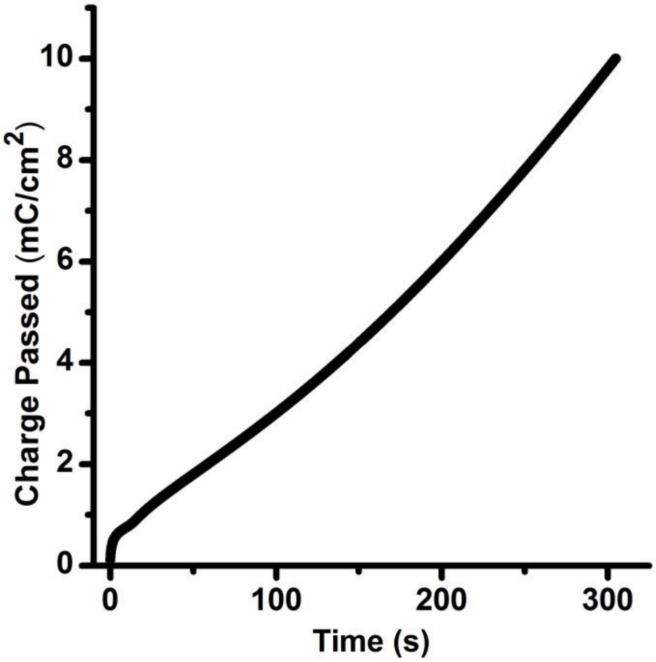

Figure 5.2. Representative 9:1 Ni-Fe-(oxy)hydroxide/borate 10 mC/cm^2 anodic deposition.

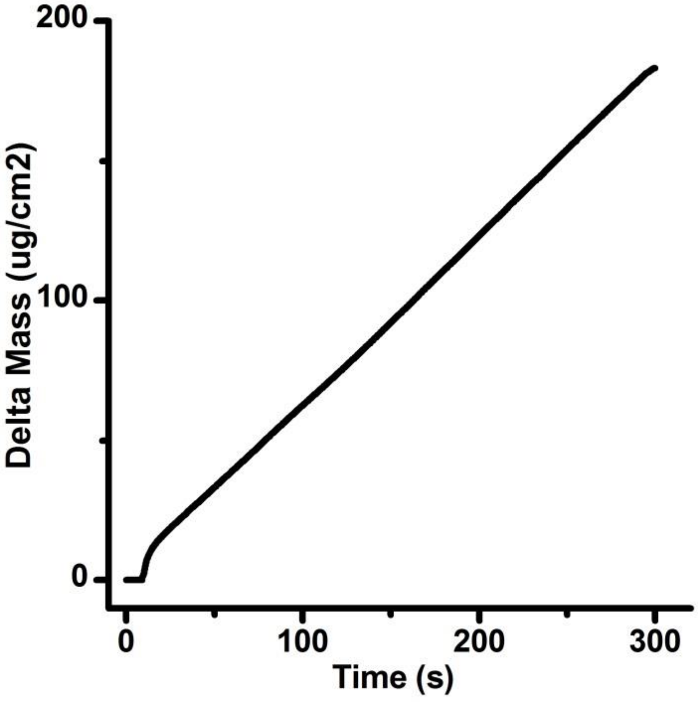

Figure 5.3 Quartz-crystal microbalance measurement of change in mass as a function of anodic deposition time.

Anodic Conditioning

All catalyst electrodes were removed from the deposition solution, rinsed in high-purity borate buffer and immediately conditioned at 0.856 V vs SCE (not corrected for series resistance) in 0.5 M buffer (99% purity ACS grade with < 10 ppm Fe for low Fe and Fe-free experiments, and 99.99% purity with <100 ppm Fe for high Fe experiments) in a three-electrode electrochemical cell without stirring.

Fe-free electrolyte was produced by purifying 0.5 M borate buffer using $Ni(OH)_2$. Briefly, ~ 2 g $Ni(NO_3)_2$ was dissolved in ~ 4 mL H_2O after which ~20 mL of 1 M high purity KOH was added to precipitate $Ni(OH)_2$. The slurry was then centrifuged and the supernatant decanted. The resulting $Ni(OH)_2$ was then rinsed 3x with high purity KOH (pH = 10.3). Potassium borate electrolyte solution was added to the $Ni(OH)_2$ to remove Fe and mechanically agitated for 10 min. The electrolyte was subsequently centrifuged, decanted, and stored for later use. Rigorously Fe-free experiments were performed in a Teflon electrochemical cell. Trace Ni species (~ 2.2 µM as estimated below) are dissolved in the purified Fe-free electrolyte solution due to the small solubility of $Ni(OH)_2$ used to absorb Fe.

Film Characterization

Scanning electron micrographs of catalyst films were taken on a Zeiss Ultra-55 with an in-lens secondary electron detector and at an accelerating voltage of 5 keV and a magnification of 50 k times. Samples were rinsed and dried at 60 °C prior to imaging. Cyclic voltammograms (CV) were collected starting at 0.756 V vs SCE and scanned between -0.004 V vs SCE to 1.15 V vs SCE at 10 mV/s for three cycles. CV measurements were performed in a three-electrode cell with a Pt counter electrode isolated with a medium porosity glass frit and were not stirred. CV data was corrected for uncompensated series resistance using impedance spectroscopy and calculated at minimum impedance and near-zero phase-angle achieved at high frequency. Typical values for the uncompensated resistance were 10-20 ohms.

Electrochemical experiments (excluding chronopotentiometric Tafel measurements) were performed without stirring. This was done to minimize the influence of Ni-deposition during conditioning in $Ni(OH)_2$ purified electrolyte and kept consistent across experiments to provide an accurate comparison of film activity.

Turn over frequency (TOF) measurements were taken at intervals after conditioning at 0.856 V vs. SCE. Water oxidation current was measured at 400 mV overpotential (corrected for iR drop) and normalized to the number of active sites via anodic peak integration assuming 1 e^- per Ni site and is consistent with microbalance experiments.

Tafel analysis was performed on films after 2 hr of uninterrupted conditioning. Samples were held at various current densities for 10 min before stepping to higher current densities. The measured potential was corrected for uncompensated series resistance and the last 30 data points at each current density were averaged. Tafel data were normalized to the number of electrochemically active Ni sites. Since Ni is deposited from Fe-free electrolyte solutions when the film is held at anodic potentials, the number of Ni sites as a function of analysis time was approximated from a linear interpolation of the number of Ni sites determined from post-conditioning and post-Tafel CVs.

Ex situ X-ray photoelectron spectroscopy was performed on an Escalab 250 (Thermoscientific) using a non-monochromated Mg source with flood charge neutralization at 200 W, 75 eV pass energy, and a 500 µm spot size. Data analysis was performed using ThermoScientific Avantage v4.75 software. A “Smart” fit was employed to subtract the backgrounds of all spectra and Mg satellite peaks were subtracted. All binding energies were calibrated to the Au4f$_{7/2}$ peak at 84.0 eV. Two peaks were used to fit the Fe 2p$_{1/2}$ and Fe 2p$_{3/2}$ (figure 5.4) peaks and two peaks were used for each Ni environment to fit the Ni 2p$_{1/2}$ and Ni 2p$_{3/2}$ (figure 5.5) peaks. During peak fitting the following constraints were set; the binding energy of the Fe 2p$_{1/2}$ peak was set to 13.6±0.1 eV higher than that of the Fe 2p$_{3/2}$, the height of the Fe 2p$_{1/2}$ was set to 50% of the height of the Fe 2p$_{3/2}$ peak, the FWHM of Fe peaks for a given sample were constrained to be equal, and the Lorentzian-Gaussian % (LG) was constrained to be equal for all Fe peaks. Similarly for the Ni XPS analysis, the binding energy of the Ni 2p$_{1/2}$ peak was set to 17.49±0.1 eV higher than that of the Ni2p$_{3/2}$, the height of the Ni 2p$_{1/2}$ was set to 50% of the height of the Ni 2p$_{3/2}$ peak, the FWHM of Ni peaks for a given sample were constrained to be equal, and the Lorentzian-Gaussian % (LG) was constrained to be equal for all Ni peaks.

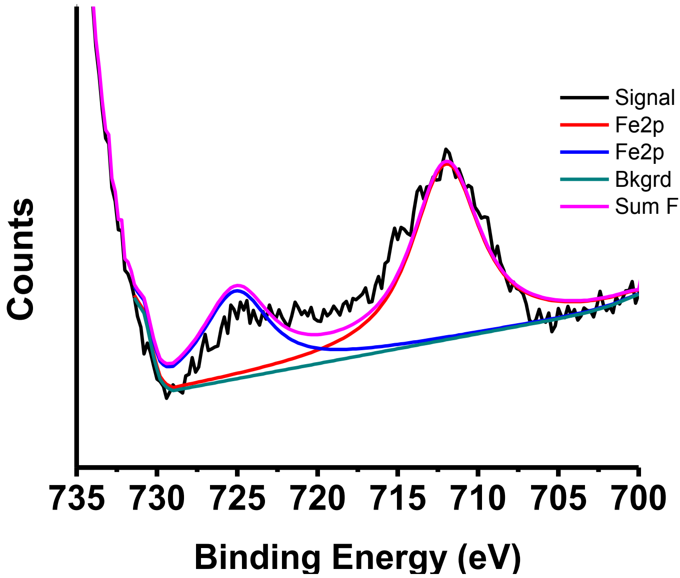

Figure 5.4. Representative Fe 2p XPS spectra sample with peak fitting

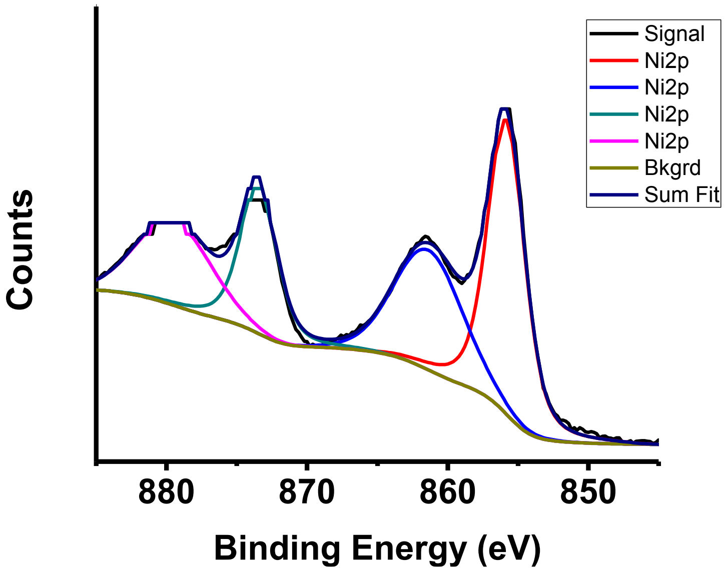

Figure 5.5. Representative Ni 2p XPS spectra with peak fitting.

Film stability was assessed by conditioning films on quartz-crystal substrates and measuring frequency changes via a microbalance. Films were found to be stable during anodic conditioning. Films were partially degraded at cathodic potentials during voltammetry and re-deposited when held at anodic potentials. We estimate the equilibrium concentration of Ni^{2+} species to be ~2.2 µM at pH 9.2 from a K_{sp} value of $5.48x10^{-16}$ for $Ni(OH)_2$, which accounts for the film dissolution observed after voltammetric cycling.

Results and Discussion

Both NiO_X-Bi and $NiFeO_X$-Bi catalyst films were morphologically similar to other electrodeposited first row transition metal hydroxides (figures 5.6 and 5.7, respectively)[17, 25-27] As-deposited films exhibited relatively low OER activity as illustrated by cyclic voltammetry (figure 5.8.A, red). Additionally, no Fe was detectable via X-ray photoelectron spectroscopy (XPS) in the as-deposited NiO_x-B_i films (figure 5.8.A, inset).

As previously reported, significant increases in water-oxidation current were observed after anodic polarization in borate electrolyte (figure 5.8.A). NiO_x-B_i films were conditioned at 0.856 V vs. SCE for 2, 5, 15, 30 and 120 min in 0.5 M potassium borate buffer solutions at pH 9.2 and subsequently characterized via voltammetry after each conditioning interval in the conditioning cell.

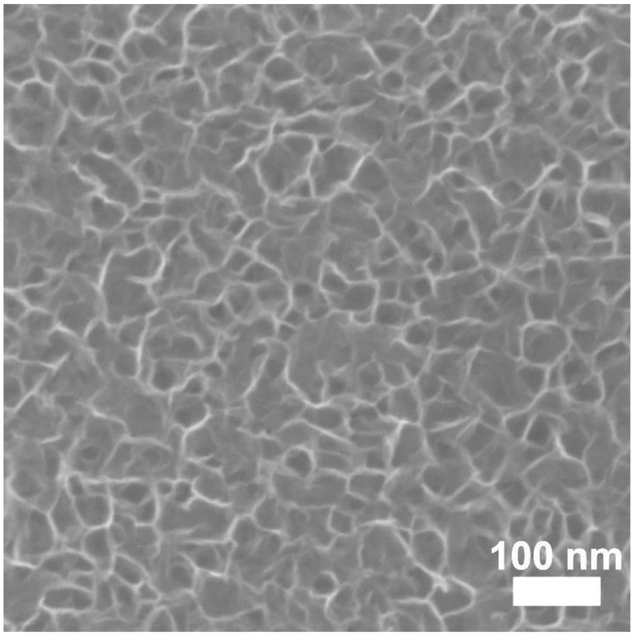

Figure 5.6. Micrograph of as-deposited Ni-(oxy)hydroxide/borate film produced after passing 10 mC/cm^2

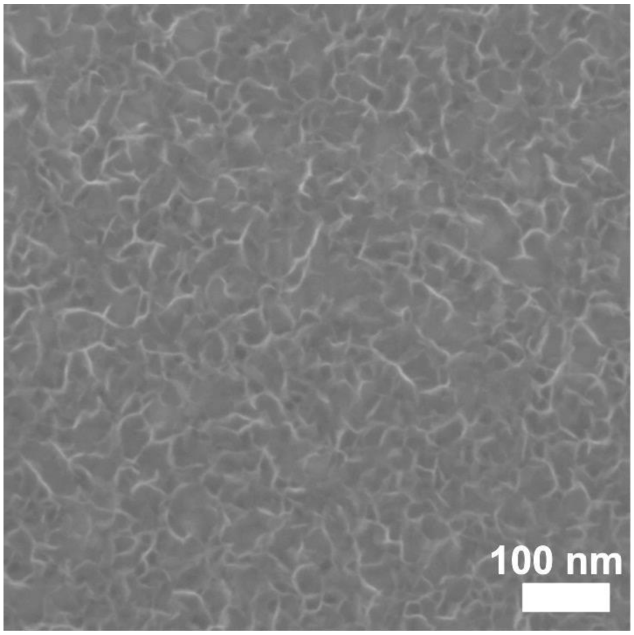

Figure 5.7. Micrograph of as-deposited Ni-Fe-(oxy)hydroxide/borate film produced after passing 10 mC/cm^2

It is important to note that the hysteresis between forward and reverse scans is an artifact of the non-stirred conditions necessary for comparison with Fe-free experiments (see below). After conditioning for 2 hr, NiO_x-B_i samples were characterized via XPS and found to contain 14% Fe (relative to Ni). This suggests that the increased activity corresponds to Fe incorporated incidentally from the borate electrolyte during conditioning, which was found to contain trace Fe impurities at ~1 ppm via the supplier lot analysis and diluted to 0.5 M. The enhancement in catalytic activity may be due to a combination of both the observed compositional changes and the structural changes previously reported. [23]

The increase in OER activity due to conditioning is also dependent on the concentration of trace Fe species in the conditioning electrolyte. NiO_x-B_i samples were similarly synthesized and conditioned in a borate buffer electrolyte solution containing ~0.1 ppm trace Fe prepared from precursors obtained from a different supplier. Again, an increase in OER current is observed in cyclic voltammograms (figure 5.8.B). Additionally, no Fe is detected via XPS in as-prepared films and after 2 hrs of conditioning in the higher-purity electrolyte, catalyst films are found to contain 5% Fe (figure 5.8.B and inset).

To further illustrate the role of Fe impurities in the observed increase in OER activity, NiO_x-B_i films were conditioned in rigorously Fe-free borate electrolyte solutions.

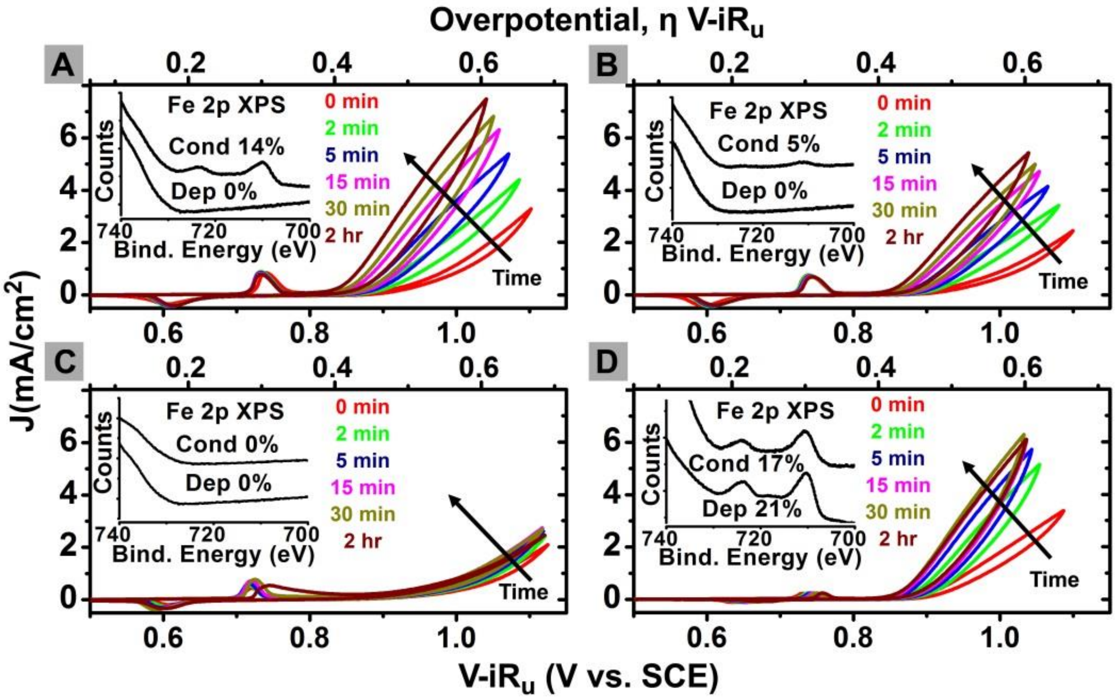

Figure 5.8. Electrochemical and XPS characterization of Ni-(oxy)hydroxide/borate films. (A) Catalyst anodically conditioned in ~1 ppm Fe containing borate electrolyte, (B) catalyst conditioned in ~0.1 ppm Fe containing electrolyte, (C) catalyst film conditioned in Fe-free borate electrolyte and (D) co-deposited Ni-Fe-(oxy)hydroxide/borate film conditioned in ~1 ppm Fe electrolyte.

Fe-free borate buffer solutions were produced from further purifying high-purity borate buffer solutions with a high-purity $Ni(OH)_2$ powder absorbent following the method of Trotochaud et. al., who showed that Fe has a strong affinity for $Ni(OH)_2$.[17] By agitating a slurry of high-purity $Ni(OH)_2$ powder in an electrolyte, trace Fe is removed. The use of $Ni(OH)_2$ as an absorbent, however, introduces soluble Ni^{2+} into the pH ~9.2 electrolyte. For films conditioned/tested in the purified Fe-free electrolyte, background deposition of NiO_x-B_i was observed which increases the amount of catalyst on the electrode with time as seen in figure 5.9.

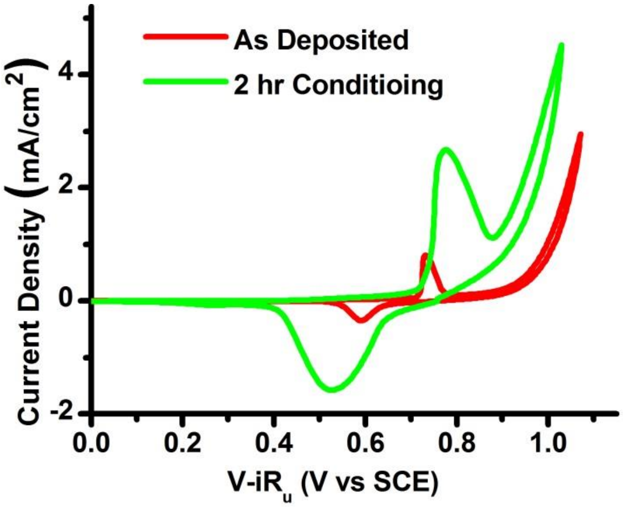

Figure 5.9. Cyclic voltammograms of as-deposited and post-conditioning Fe-free films in $Ni(OH)_2$ purified electrolyte. Note increase in Ni peak areas due to deposition from Ni species.

To minimize this effect the electrolyte was, in all cases, not stirred during conditioning at 0.856 V vs. SCE. By not stirring, hysteresis is introduced into CV data (figure 5.8); however, this effect is seen across all films and non-stirred experiments show similar behavior as stirred experiments (figure 5.10).

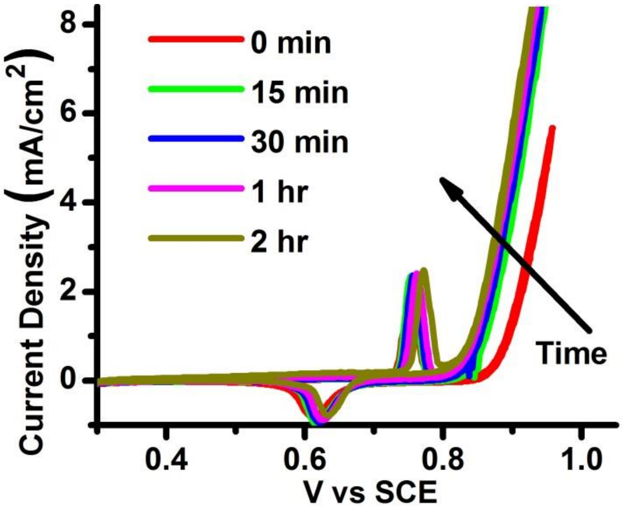

Figure 5.10. Cyclic voltammograms of Ni-(oxy)hydroxide/borate film conditioned and measured under stirred conditions.

Cyclic voltammograms show significantly lower OER activity with the absence of Fe impurities in the conditioning electrolyte (figure 5.6.C). The activity of the film is essentially unchanged during the course of the 2 h conditioning experiment in the purified electrolyte, and Fe is not found via XPS analysis in those films (figure 5.6.C inset). The small increase in OER current after conditioning that is observed is likely due to additional Ni deposition from the purified electrolyte which increases total catalyst loading as seen in figure 5.9. This data further support the hypothesis that the observed OER activity is correlated to Fe content in the catalyst films in near-neutral pH, as it is in basic pH. Catalyst films were found to be stable at OER potentials via microgravity measurements (figure 5.11). Films were somewhat degraded at cathodic potentials present during voltammetry. Material was subsequently partially re-deposited when the electrode was held at anodic potentials.

To directly increase catalyst performance, Fe was intentionally incorporated into catalyst films via anodic co-deposition from a mixed solution of $Ni(NO_3)_2/FeCl_2$. From a solution with a Ni:Fe ratio of 9:1, as-deposited films had a ratio of 3.8:1, i.e. 21% Fe (figure 5.8.D inset), which implies Fe is preferentially deposited over Ni at anodic potentials. Although Ni-Fe-(oxy)hydroxide/borate $NiFeO_x$-B_i films improved after short conditioning, the intentional incorporation of Fe reduced the need for anodic conditioning in electrolyte solutions (figure 5.8.D) from > 2 hr to less than 30 min.

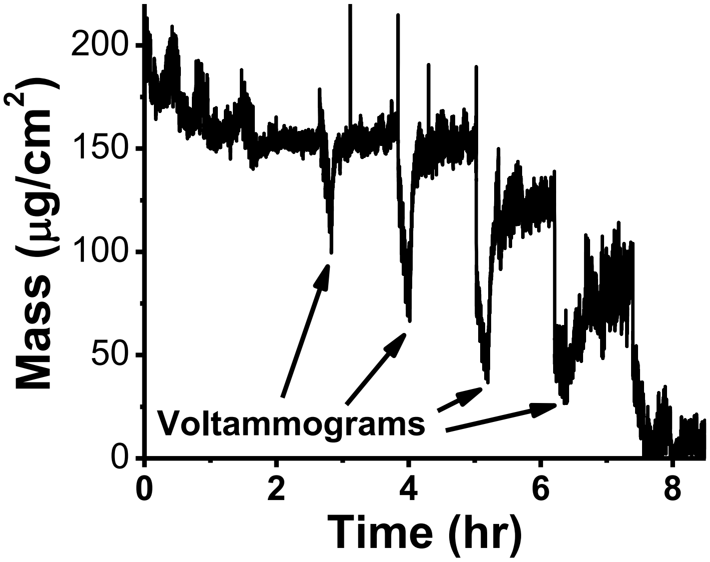

Figure 5.11. Quartz-crystal microbalance measurement of change in mass as a function of time conditioned at 0.856 V vs. SCE. Arrows indicate film degradation and subsequent re-deposition during voltammetric characterization.

The data in figure 5.8 are normalized only to geometric area and do not take into account the amount of catalyst on the electrode surface. Films deposited from the mixed Ni-Fe solutions show a substantially smaller pre-OER Ni$^{2+/3+}$ wave in the voltammetry compared to those deposited from the Ni-only precursors. To compare the intrinsic activity of the catalysts we compare the turn over frequencies (TOF), calculated at an overpotential of 400 mV and normalized to the number of Ni atoms in the film (figure 5.12.A). To estimate the number of Ni we integrate the pre-OER oxidation wave in the voltammetry and assume 1 e$^-$ per Ni center, which is in good agreement with the ~1.1 e$^-$ per Ni determined via microbalance measurements assuming the film was composed entirely of NiOOH. We note that this simplification thus likely slightly underestimates intrinsic film activities as previous studies have found ~1.6 e$^-$ per Ni.[23] The TOF of rigorously Fe-free NiO_x-B_i films remains constant with conditioning. The TOF for Ni films in electrolyte containing Fe-impurities increases after several minutes at anodic potentials and eventually levels off after several hours. Catalyst films where Fe was intentionally incorporated not only have initially substantially higher TOFs, but also show increases in TOF over the first 30 min. The remaining OER activity dependence for $NiFeO_x$-B_i with conditioning may be attributed to film rearrangement.[23] The absolute TOF (figure 5.13) for the Ni-Fe films (~1.4 s^{-1}) is substantially higher than that for the Ni films, even after anodic conditioning (~0.3 s^{-1}).

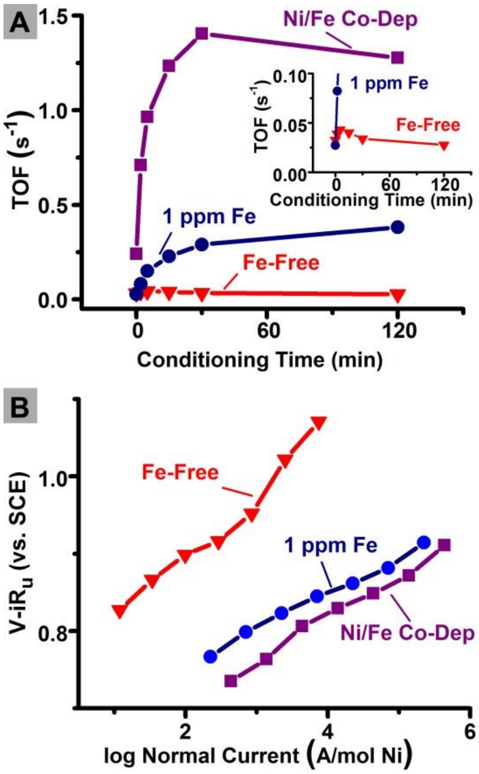

Figure 5.12. TOF and Tafel analysis of catalyst films. (A) TOF as a function of time conditioned at 0.856 V vs. SCE in electrolyte with trace Fe impurities (blue), rigorously Fe-free (red) and Ni/Fe co-deposited films (purple), (B) Tafel plot of catalyst films conditioned for 2 hr in regular purity electrolyte (blue), Fe-free electrolyte (red), and unconditioned Ni/Fe co-deposited catalyst films.

Further evidence that the presence of Fe plays a key role in the observed activity of NiO_x-B_i catalyst films is seen in a Tafel plot comparison (figure 5.12.B). Tafel slopes were calculated from points in the linear regime up to a current density of $10^{-2.5}$ A/cm^2. The Tafel slope of NiO_x-B_i conditioned for 2 hr was 46 mV/decade while for the films conditioned in rigorously Fe-free electrolyte it was 78 mV/decade. Unconditioned Ni/Fe co-deposited films had similar catalytic activity as conditioned NiO_x-B_i with a Tafel slope of 56 mV/decade, suggesting similar a OER mechanism involving Fe in both. Due to deposition of trace Ni from the electrolyte solution during both conditioning and chronopotentiometric experiments, Tafel data were normalized to the number of electrochemically active Ni centers to provide a comparison across samples. To minimize deposition during conditioning the solution was not stirred, although the solution was stirred during Tafel measurements to facilitate bubble release from the film surface.

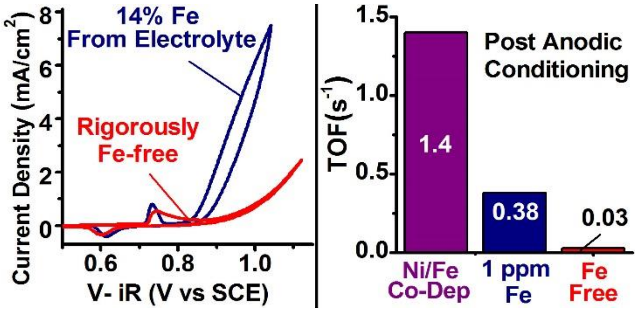

Figure 5.13. Summary of finding with comparison of cyclic voltammograms of Fe-incorporated and Fe-free films (A), and comparison of TOF between Fe-co-deposited, Fe-impurity and Fe-free films (B).

Conclusions

In summary, we have demonstrated that the OER activity in NiO_x-B_i catalysts can be significantly enhanced through the introduction of Fe (figure 5.13). If sufficiently Fe-free conditions are used such that Fe incorporation is not observed *via* XPS, the OER activity is inhibited. This work is important for the application of NiO_x-B_i catalysts, as the higher activity $NiFeO_x$-B_i phases can now be directly targeted, thus reducing reliance on electrolyte Fe impurities and anodic conditioning to form the active phase.

In this body of work, research on a variety of metal-oxide materials has been presented. Chapter I introduced the need for solar energy storage and water splitting as promising strategy. Chapter II presented a defect mediated growth mechanism for thermally deposited tungsten oxide nanowires This result has consequences for the application of WO_X as a photoanode material, as defects well known centers for parasitic recombination. Chapter III described work toward the fabrication of tungsten oxide devices for advanced characterization. In chapter IV, the key result of chapter II that thermally deposited NWs are highly defective and therefore conductive is used to design a new acid stable OER catalyst scaffold. In conclusion, this work has shown that through expanding the fundamental understanding of metal oxide systems, new approaches to material applications can be forged.

REFERENCES CITED

Chapter I

1. C. Parmesan and G. Yohe, *Nature (London, U. K.)*, 2003, **421**, 37-42.

2. P. M. Cox, R. A. Betts, C. D. Jones, S. A. Spall and L. J. Totterdell, *Nature (London)*, 2000, **408**, 184-187.

3. C. A. Deutsch, J. J. Tewksbury, R. B. Huey, K. S. Sheldon, C. K. Ghalambor, D. C. Haak and P. R. Martin, *Proc. Natl. Acad. Sci. U. S. A.*, 2008, **105**, 6668-6672.

4. J. Hansen, M. Sato, R. Ruedy, K. Lo, D. W. Lea and M. Medina-Elizade, *Proc. Natl. Acad. Sci. U. S. A.*, 2006, **103**, 14288-14293.

5. R. J. Norby, E. H. DeLucia, B. Gielen, C. Calfapietra, C. P. Giardina, J. S. King, J. Ledford, H. R. McCarthy, D. J. P. Moore, R. Ceulemans, P. De Angelis, A. C. Finzi, D. F. Karnosky, M. E. Kubiske, M. Lukac, K. S. Pregitzer, G. E. Scarascia-Mugnozza, W. H. Schlesinger and R. Oren, *Proc. Natl. Acad. Sci. U. S. A.*, 2005, **102**, 18052-18056.

6. J. L. Sarmiento, T. M. C. Hughes, R. J. Stouffer and S. Manabe, *Nature (London)*, 1998, **393**, 245-249.

7. S. D. Smith, T. E. Huxman, S. F. Zitzer, T. N. Charlet, D. C. Housman, J. S. Coleman, L. K. Fenstermaker, J. R. Seemann and R. S. Nowak, *Nature (London)*, 2000, **408**, 79-82.

8. J. Hansen, I. Fung, A. Lacis, D. Rind, S. Lebedeff, R. Ruedy, G. Russell and P. Stone, *J. Geophys. Res., D: Atmos.*, 1988, **93**, 9341-9364.

9. S. Solomon, G.-K. Plattner, R. Knutti and P. Friedlingstein, *Proc. Natl. Acad. Sci. U. S. A.*, 2009, **106**, 1704-1709.

10. M. Cao and F. I. Woodward, *Nature (London)*, 1998, **393**, 249-252.

11. D. J. Rogers and S. E. Randolph, *Science*, 2000, **289**, 1763-1766.

12. D. J. Hofmann, J. H. Butler and P. P. Tans, *Atmos. Environ.*, 2009, **43**, 2084-2086.

13. J. G. Canadell, Q. C. Le, M. R. Raupach, C. B. Field, E. T. Buitenhuis, P. Ciais, T. J. Conway, N. P. Gillett, R. A. Houghton and G. Marland, *Proc. Natl. Acad. Sci. U. S. A.*, 2007, **104**, 18866-18870.

14. S. Luyssaert, E. D. Schulze, A. Borner, A. Knohl, D. Hessenmoller, B. E. Law, P. Ciais and J. Grace, *Nature*, 2008, **455**, 213-215.

15. O. Hoegh-Guldberg, P. J. Mumby, A. J. Hooten, R. S. Steneck, P. Greenfield, E. Gomez, C. D. Harvell, P. F. Sale, A. J. Edwards, K. Caldeira, N. Knowlton, C. M. Eakin, R. Iglesias-Prieto, N. Muthiga, R. H. Bradbury, A. Dubi and M. E. Hatziolos, *Science (Washington, DC, U. S.)*, 2007, **318**, 1737-1742.

16. E. A. G. Schuur, J. G. Vogel, K. G. Crummer, H. Lee, J. O. Sickman and T. E. Osterkamp, *Nature (London, U. K.)*, 2009, **459**, 556-559.

17. P. D. Noyes, M. K. McElwee, H. D. Miller, B. W. Clark, L. A. Van Tiem, K. C. Walcott, K. N. Erwin and E. D. Levin, *Environ. Int.*, 2009, **35**, 971-986.

18. *World energy assessment : overview : 2004 update*, New York, NY : United Nations Development Programme, Bureau for Development Policy, New York, NY, 2004.

19. C. Liu, F. Li, L.-P. Ma and H.-M. Cheng, *Adv. Mater.*, 2010, **22**, E28-E62.

20. R. P. Deshpande, *Capacitors*, New York : McGraw-Hill Education, 2015.

21. *Chemical Rubber Company handbook of chemistry and physics*, 1978.

22. R. A. Huggins, *Advanced batteries : materials science aspects*, New York London : Springer, New York [London], 2009.

23. H. Barthelemy, *Int. J. Hydrogen Energy*, 2012, **37**, 17364-17372.

24. Z. S. Wronski, *Int. Mater. Rev.*, 2001, **46**, 1-49.

25. S. L. Coleman, *Quality of coal resources of Northwest Georgia*, Atlanta? : Georgia Geologic Survey, Environmental Protection Division, Dept. of Natural Resources, Atlanta?], 1986.

26. S. Parkash, *Petroleum fuels manufacturing handbook : including specialty products and sustainable manufacturing techniques*, New York : McGraw-Hill, New York, 2010.

27. T. R. Crompton, *Battery reference book*, Oxford, England
Boston : Newnes, Oxford, England
Boston, 3rd ed. edn., 2000.

28. R. M. Dell and D. A. J. Rand, *J. Power Sources*, 2001, **100**, 2-17.

29. M. Jayalakshmi and K. Balasubramanian, *Int. J. Electrochem. Sci.*, 2008, **3**, 1196-1217.

30. W. J. Sarjeant, J. Zirnheld and F. W. MacDougall, *IEEE Trans. Plasma Sci.*, 1998, **26**, 1368-1392.

31. *Creating baseload wind power systems using advanced compressed air energy storage concepts*, Golden, CO : National Renewable Energy Laboratory, Golden, CO, 2006.

32. *Flywheel energy storage*, Washington, D.C. : U.S. Dept. of Energy, Office of Energy Efficiency and Renewable Energy, Washington, D.C., 2003.

33. *Conceptual design of a flywheel energy storage system : final report*, Albuquerque, N.M. : Dept. of Energy, Sandia Laboratories, Springfield, Va. : For sale by the National Technical Information Service, Albuquerque, N.M. : [Springfield, Va.], 1979.

34. C. Le Quere, M. R. Raupach, J. G. Canadell, G. Marland, L. Bopp, P. Ciais, T. J. Conway, S. C. Doney, R. A. Feely, P. Foster, P. Friedlingstein, K. Gurney, R. A. Houghton, J. I. House, C. Huntingford, P. E. Levy, M. R. Lomas, J. Majkut, N. Metzl, J. P. Ometto, G. P. Peters, I. C. Prentice, J. T. Randerson, S. W. Running, J. L. Sarmiento, U. Schuster, S. Sitch, T. Takahashi, N. Viovy, G. R. van der Werf and F. I. Woodward, *Nat. Geosci.*, 2009, **2**, 831-836.

35. A. J. Bard and M. A. Fox, *Acc. Chem. Res.*, 1995, **28**, 141-145.

36. T. Bak, J. Nowotny, M. Rekas and C. C. Sorrell, *Int. J. Hydrogen Energy*, 2002, **27**, 991-1022.

37. A. J. Traynor and R. J. Jensen, *Ind. Eng. Chem. Res.*, 2002, **41**, 1935-1939.

38. A. J. Morris, G. J. Meyer and E. Fujita, *Acc. Chem. Res.*, 2009, **42**, 1983-1994.

39. M. G. Walter, E. L. Warren, J. R. McKone, S. W. Boettcher, Q. Mi, E. A. Santori and N. S. Lewis, *Chem. Rev. (Washington, DC, U. S.)*, 2010, **110**, 6446-6473.

40. Y. Tachibana, L. Vayssieres and J. R. Durrant, *Nat. Photonics*, 2012, **6**, 511-518.

41. T. Hisatomi, J. Kubota and K. Domen, *Chem. Soc. Rev.*, 2014, **43**, 7520-7535.

42. I. Ganesh, *Mater. Sci. Appl.*, 2011, **2**, 1407-1415.

43. R. J. Jensen and J. L. Lyman, 1999.

44. M. Jitaru, *J. Univ. Chem. Technol. Metall.*, 2007, **42**, 333-344.

45. K. P. Brooks, J. Hu, H. Zhu and R. J. Kee, *Chem. Eng. Sci.*, 2007, **62**, 1161-1170.
46. S. K. Hoekman, A. Broch, C. Robbins and R. Purcell, *Int. J. Greenhouse Gas Control*, 2009, **4**, 44-50.

47. K. R. Sridhar, C. S. Iacomini and J. E. Finn, *J. Propul. Power*, 2004, **20**, 892-901.

48. I. Navarro-Solis, L. Villalba-Almendra and A. Alvarez-Gallegos, *Int. J. Hydrogen Energy*, 2010, **35**, 10833-10841.

49. A. M. A. El-Bassuoni, J. W. Sheffield and T. N. Veziroglu, *Int. J. Hydrogen Energy*, 1982, **7**, 919-923.

50. J. Kim and W. Choi, *Energy Environ. Sci.*, 2010, **3**, 1042-1045.

51. J.-S. Thomas and B. Durham, *Desalination*, 2003, **156**, 21-28.

52. C. Yu, *Nature (London, U. K.)*, 2011, **470**, 307.

53. D. W. Schindler and W. F. Donahue, *Proc. Natl. Acad. Sci. U. S. A.*, 2006, **103**, 7210-7216.

54. J. A. Foley, R. DeFries, G. P. Asner, C. Barford, G. Bonan, S. R. Carpenter, F. S. Chapin, M. T. Coe, G. C. Daily, H. K. Gibbs, J. H. Helkowski, T. Holloway, E. A. Howard, C. J. Kucharik, C. Monfreda, J. A. Patz, I. C. Prentice, N. Ramankutty and P. K. Snyder, *Science (Washington, DC, U. S.)*, 2005, **309**, 570-574.

55. C. J. Vorosmarty, P. Green, J. Salisbury and R. B. Lammers, *Science (Washington, D. C.)*, 2000, **289**, 284-288.

56. H. Park, C. D. Vecitis and M. R. Hoffmann, *Prepr. Ext. Abstr. ACS Natl. Meet., Am. Chem. Soc., Div. Environ. Chem.*, 2008, **48**, 1076.

57. A. Harriman, I. J. Pickering, J. M. Thomas and P. A. Christensen, *J. Chem. Soc., Faraday Trans. 1*, 1988, **84**, 2795-2806.

58. R. D. Britt, *Adv. Photosynth.*, 1996, **4**, 137-164.

59. J. Rossmeisl, Z. W. Qu, H. Zhu, G. J. Kroes and J. K. Norskov, *J. Electroanal. Chem.*, 2007, **607**, 83-89.

60. J. R. McKone, S. C. Marinescu, B. S. Brunschwig, J. R. Winkler and H. B. Gray, *Chem. Sci.*, 2014, **5**, 865-878.

61. L. A. Kibler, *ChemPhysChem*, 2006, **7**, 985-991.

62. S. Trasatti, *Adv. Electrochem. Sci. Eng.*, 1992, **2**, 1-85.

63. R. L. Doyle and M. E. G. Lyons, *Phys. Chem. Chem. Phys.*, 2013, **15**, 5224-5237.

64. B. S. Yeo and A. T. Bell, *J. Am. Chem. Soc.*, 2011, **133**, 5587-5593.

65. G. K. Schweitzer, *The aqueous chemistry of the elements*, Oxford
New York : Oxford University Press, Oxford
New York, 2010.

66. L. Trotochaud, S. L. Young, J. K. Ranney and S. W. Boettcher, *J. Am. Chem. Soc.*, 2014, **136**, 6744-6753.

67. A. M. Smith, L. Trotochaud, M. S. Burke and S. W. Boettcher, *Chem. Commun.*, 2015, **51**, 5261-5263.

68. D. A. Corrigan, *J. Electrochem. Soc.*, 1987, **134**, 377-384.

69. T. J. O'Keeke, *Pourbaix Diagrams*, Elsevier Ltd.

70. C. Iliescu, B. Chen and J. Miao, *Sens. Actuators, A*, 2008, **143**, 154-161.

71. Y. Lee, J. Suntivich, K. J. May, E. E. Perry and Y. Shao-Horn, *J. Phys. Chem. Lett.*, 2012, **3**, 399-404.

72. C. C. McCrory, S. Jung, J. C. Peters and T. F. Jaramillo, 2013.

73. P. P. González-Borrero, F. Sato, A. N. Medina, M. L. Baesso, A. C. Bento, G. Baldissera, C. Persson, G. A. Niklasson, C. G. Granqvist and A. Ferreira da Silva, *Appl. Phys. Lett.*, 2010, **96**, 061909.

74. C. G. Granqvist, *Sol. Energy Mater. Sol. Cells*, 2000, **60**, 201-262.

75. H. Zheng, J. Z. Ou, M. S. Strano, R. B. Kaner, A. Mitchell and K. Kalantar-zadeh, *Adv. Funct. Mater.*, 2011, **21**, 2175-2196.

76. G. Y. Chen, V. Stolojan, D. C. Cox, C. Giusca and S. R. P. Silva, 2006.

77. C.-C. Liao, F.-R. Chen and J.-J. Kai, *Sol. Energy Mater. Sol. Cells*, 2006, **90**, 1147-1155.

78. K. Hong, M. Xie, R. Hu and H. Wu, *Appl. Phys. Lett.*, 2007, **90**, 173121/173121-173121/173123.

79. M. Remškar, J. Kovac, M. Viršek, M. Mrak, A. Jesih and A. Seabaugh, *Adv. Funct. Mater.*, 2007, **17**, 1974-1978.

80. T. Lana-Villarreal, D. Monllor-Satoca, R. Gomez and P. Salvador, *Electrochem. Commun.*, 2006, **8**, 1784-1790.

81. K. X. Wang, Z. Yu, V. Liu, M. L. Brongersma, T. F. Jaramillo and S. Fan, *ACS Photonics*, 2014, **1**, 235-240.

82. V. Lefv̈re, *Nanotechnology Science and Technology : Nanowires : Properties, Synthesis and Applications*, New York, NY, USA Nova Science Publishers, Inc., New York, NY, USA
New York, 2012.

83. S. W. Boettcher, J. M. Spurgeon, M. C. Putnam, E. L. Warren, D. B. Turner-Evans, M. D. Kelzenberg, J. R. Maiolo, H. A. Atwater and N. S. Lewis, *Science (Washington, DC, U. S.)*, 2010, **327**, 185-187.

84. R. A. Pala, A. J. Leenheer, M. Lichterman, H. A. Atwater and N. S. Lewis, *Energy Environ. Sci.*, 2014, **7**, 3424-3430.

85. A. M. Smith, M. G. Kast, B. A. Nail, S. Aloni and S. W. Boettcher, *J. Mater. Chem. A*, 2014, **2**, 6121-6129.

86. G. D. Rieck, *Tungsten and its compounds*, Pergamon Press, Oxford; New York, 1967.

87. E. S. W.-D. Lassner, *Tungsten : properties, chemistry, technology of the element, alloys, and chemical compounds*, Kluwer Academic/Plenum Publishers, New York, 1999.

88. J. G. Allpress, R. J. D. Tilley and M. J. Sienko, *J. Solid State Chem.*, 1971, **3**, 440-451.

89. S. Tanisaki, *J. Phys. Soc. Jpn.*, 1960, **15**, 573-581.

90. A. Magneli, *Pure Appl. Chem.*, 1978, **50**, 1261-1271.

91. R. J. D. Tilley, *Mater. Res. Bull.*, 1970, **5**, 813-823.

92. A. Magneli, *Acta Crystallogr.*, 1953, **6**, 495-500.

93. K. Lips, P. Kanschat and W. Fuhs, *Sol. Energy Mater. Sol. Cells*, 2003, **78**, 513-541.

94. W. M. Bullis and H. R. Huff, *J. Electrochem. Soc.*, 1996, **143**, 1399-1405.

95. Q. Xu, M. H. Gray and J. W. P. Hsu, *J. Appl. Phys.*, 1997, **82**, 748-755.

96. X. Liu, F. Wang and Q. Wang, *Phys. Chem. Chem. Phys.*, 2012, **14**, 7894-7911.

97. K.-S. Ahn, S.-H. Lee, A. C. Dillon, C. E. Tracy and R. Pitts, *J. Appl. Phys.*, 2007, **101**, 093524.

98. A. Georg, W. Graf and V. Wittwer, *Sol. Energy Mater. Sol. Cells*, 1998, **51**, 353-370.

99. S. Ramanathan, *Thin Film Metal-Oxides*, Dordrecht : Springer, Dordrecht New York, 2009.

100. C. N. R. Rao, *Transition metal oxides*, New York : VCH, New York, 1995.

Chapter II

1. G. Gu, B. Zheng, W. Q. Han, S. Roth and J. Liu, *Nano Lett.*, 2002, **2**, 849-851.

2. Z. R. Dai, J. L. Gole, J. D. Stout and Z. L. Wang, *J. Phys. Chem. B*, 2002, **106**, 1274-1279.

3. M. H. Huang, Y. Wu, H. Feick, N. Tran, E. Weber and P. Yang, *Adv. Mater.*, 2001, **13**, 113-116.

4. F. Meng, S. A. Morin and S. Jin, *J. Am. Chem. Soc.*, 2011, **133**, 8408-8411.

5. H. Zheng, J. Z. Ou, M. S. Strano, R. B. Kaner, A. Mitchell and K. Kalantar-zadeh, *Adv. Funct. Mater.*, 2011, **21**, 2175-2196.

6. X. Liu, F. Wang and Q. Wang, *Phys. Chem. Chem. Phys.*, 2012, **14**, 7894-7911.

7. G. Hodes, D. Cahen and J. Manassen, *Nature*, 1976, **260**, 312-313.

8. E. L. Miller, B. Marsen, B. Cole and M. Lum, *Electrochem. Solid-State Lett.*, 2006, **9**, G248-G250.

9. K. R. Reyes-Gil, C. Wiggenhorn, B. S. Brunschwig and N. S. Lewis, *J. Phys. Chem. C*, 2013, **117**, 14947-14957.

10. H. Chen, N. Xu, S. Deng, J. Zhou, Z. Li, H. Ren, J. Chen and J. She, *J. Appl. Phys.*, 2007, **101**, 114303.

11. D. H. Koo, M. Kim and S. Chang, *Org. Lett.*, 2005, **7**, 5015-5018.

12. B. Deb, S. Desai, G. U. Sumanasekera and M. K. Sunkara, *Nanotechnology*, 2007, **18**, 285501.

13. C. Fenster, A. J. Smith, A. Abts, S. Milenkovic and A. W. Hassel, *Electrochem. Commun.*, 2008, **10**, 1125-1128.

14. J. Liu, Z. Zhang, Y. Zhao, X. Su, S. Liu and E. Wang, *Small*, 2005, **1**, 310-313.

15. S. Tanisaki, *J. Phys. Soc. Jpn.*, 1960, **15**, 573-581.

16. G. Hagg and A. Magneli, *Ark. Kemi, Mineral. Geol.*, 1944, **19A**, 14 pp.

17. A. Magneli, *Ark. Kemi*, 1949, **1**, 223-230.

18. A. Magneli, *Nature*, 1950, **165**, 356-357.

19. J. G. Allpress, R. J. D. Tilley and M. J. Sienko, *J. Solid State Chem.*, 1971, **3**, 440-451.

20. J. S. Anderson and R. J. D. Tilley, *Surf. Defect Prop. Solids*, 1974, **3**, 1-50.

21. A. Magneli, *Informal Proc. Buhl Intern. Conf. Mater., Pittsburgh*, 1964, 109-122.

22. W. K. Burton, N. Cabrera and F. C. Frank, *Philos. Trans. R. Soc. London, A*, 1951, **243**, 299-358.

23. S. A. Morin, M. J. Bierman, J. Tong and S. Jin, *Science*, 2010, **328**, 476-480.

24. R. S. Wagner and W. C. Ellis, *Appl. Phys. Lett.*, 1964, **4**, 89-90.

25. N. Wang, Y. Cai and R. Q. Zhang, *Mat. Sci. Eng. R*, 2008, **60**, 1-51.

26. L. E. Greene, M. Law, J. Goldberger, F. Kim, J. C. Johnson, Y. F. Zhang, R. J. Saykally and P. D. Yang, *Angew. Chem. Int. Ed.*, 2003, **42**, 3031-3034.

27. Z. Y. Yuan and B. L. Su, *Colloids Surf., A*, 2004, **241**, 173-183.

28. G. Wang, X. Shen, J. Horvat, B. Wang, H. Liu, D. Wexler and J. Yao, *J. Phys. Chem. C*, 2009, **113**, 4357-4361.

29. J. Zhu, S. Wang, S. Xie and H. Li, *Chem. Commun.*, 2011, **47**, 4403-4405.

30. J. N. Shapiro, A. Lin, D. L. Huffaker and C. Ratsch, *Phys. Rev. B*, 2011, **84**.

31. Y. Kojima, K. Kasuya, K. Nagato, T. Hamaguchi and M. Nakao, *J. Vac. Sci. Technol., B*, 2008, **26**, 1942.

32. F. Liu, L. Li, F. Mo, J. Chen, S. Deng and N. Xu, *Cryst. Growth Des.*, 2010, **10**, 5193-5199.

33. S. M. Cui, G. H. Lu, S. Mao, K. H. Yu and J. H. Chen, *Chem. Phys. Lett.*, 2010, **485**, 64-68.

34. C.-C. Liao, F.-R. Chen and J.-J. Kai, *Sol. Energy Mater. Sol. Cells*, 2007, **91**, 1258-1266.

35. J. Thangala, S. Vaddiraju, R. Bogale, R. Thurman, T. Powers, B. Deb and M. K. Sunkara, *Small*, 2007, **3**, 890-896.

36. J. Zhou, Y. Ding, S. Z. Deng, L. Gong, N. S. Xu and Z. L. Wang, *Adv. Mater.*, 2005, **17**, 2107-2110.

37. S. Wang, Y. He, J. Zou, P. Cao, Y. Jiang, B. Huang, C. Liu and P. Liaw, *J. Cryst. Growth*, 2007, **303**, 574-579.

38. K. H. Liu, W. L. Wang, Z. Xu, L. Liao, X. D. Bai and E. G. Wang, *Appl. Phys. Lett.*, 2006, **89**, 221908.

39. Y. Li, Y. Bando and D. Golberg, *Adv. Mater.*, 2003, **15**, 1294-1296.

40. K. Liu, D. T. Foord and L. Scipioni, *Nanotechnology*, 2005, **16**, 10-14.

41. F. Xu, S. D. Tse, J. F. Al-Sharab and B. H. Kear, *Appl. Phys. Lett.*, 2006, **88**, 243115.

42. A. Temmink, O. Anderson, K. Bange, H. Hantsche and X. Yu, *Thin Solid Films*, 1990, **192**, 211-218.

43. K. Senthil and K. Yong, *Nanotechnology*, 2007, **18**.

44. E. S. W.-D. Lassner, *Tungsten : properties, chemistry, technology of the element, alloys, and chemical compounds*, Kluwer Academic/Plenum Publishers, New York, 1999.

45. B. Cao, J. Chen, X. Tang and W. Zhou, *J. Mater. Chem.*, 2009, **19**, 2323-2327.

46. H. Zhang, T. T. Xu, M. Tang, T.-h. Her and S.-y. Li, *J. Vac. Sci. Technol., B: Nanotechnol. Microelectron.: Mater., Process., Meas., Phenom.*, 2010, **28**, 310-315.

47. D. Y. Lu, J. Chen, S. Z. Deng, N. S. Xu and W. H. Zhang, *J. Mater. Res.*, 2011, **23**, 402-408.

48. M. I. d. Hertog, C. Cayron, P. Gentile, F. Dhalluin, F. Oehler, T. Baron and J. L. Rouviere, *Nanotechnology*, 2012, **23**, 025701.

49. T. Suzuki, H. Wakabayashi, Y. Nishi and M. Fujimoto, *J. Ceram. Soc. Jpn.*, 2002, **110**, 86-91.

50. R. J. D. Tilley, *Crystals and crystal structures*, John Wiley, Hoboken, NJ, 2006.

51. P. M. Parthangal, R. E. Cavicchi, C. B. Montgomery, S. Turner and M. R. Zachariah, *J. Mater. Res.*, 2011, **20**, 2889-2894.

52. A. Ponzoni, E. Comini, G. Sberveglieri, J. Zhou, S. Z. Deng, N. S. Xu, Y. Ding and Z. L. Wang, *Appl. Phys. Lett.*, 2006, **88**, 203101/203101-203101/203103.

53. G. D. Rieck, *Tungsten and its compounds*, Pergamon Press, Oxford; New York, 1967.

54. R. Azimirad, P. Khosravi and A. Z. Moshfegh, *J. Exp. Nanosci.*, 2012, **7**, 597-607.

55. G. Y. Chen, V. Stolojan, D. C. Cox, C. Giusca and S. R. P. Silva, 2006.

56. X. Zhang, L. Gong, K. Liu, Y. Cao, X. Xiao, W. Sun, X. Hu, Y. Gao, J. Chen, J. Zhou and Z. L. Wang, *Adv. Mater.*, 2010, **22**, 5292-5296.

57. P. Van der Heide, *X-ray photoelectron spectroscopy : an introduction to principles and practices*, Wiley, Hoboken, N.J., 2012.

58. B. Marsen, B. Cole and E. L. Miller, *Sol. Energy Mater. Sol. Cells*, 2007, **91**, 1954-1958.

59. S. M. Sze, *Physics of semiconductor devices*, Wiley, New York, 1981.

60. D. M. Rowe and V. S. Shukla, *J. Appl. Phys.*, 1981, **52**, 7421-7426.

61. G. Kieslich, C. S. Birkel, J. E. Douglas, M. Gaultois, I. Veremchuk, R. Seshadri, G. D. Stucky, Y. Grin and W. Tremel, *J. Mater. Chem. A*, 2013, **1**, 13050-13054.

62. R. A. Bennett, S. Poulston, P. Stone and M. Bowker, *Phys. Rev. B*, 1999, **59**, 10341-10346.

63. R. J. Cava, B. Batlogg, J. J. Krajewski, H. F. Poulsen, P. Gammel, W. F. Peck and L. W. Rupp, *Phys. Rev. B*, 1991, **44**, 6973-6981.

Chapter III

1. V. Subramanian, E. E. Wolf and P. V. Kamat, *J. Am. Chem. Soc.*, 2004, **126**, 4943-4950.

2. X. Zeng, S. Yan, J. Cui, H. Liu, J. Dong, W. Xia, M. Zhou and H. Chen, *J. Nanopart. Res.*, 2015, **17**, 1-11.

3. S. Nie and S. R. Emory, *Science (Washington, D. C.)*, 1997, **275**, 1102-1106.

4. W. W. Yu, L. Qu, W. Guo and X. Peng, *Chem. Mater.*, 2003, **15**, 2854-2860.

5. A. P. Alivisatos, *J. Phys. Chem.*, 1996, **100**, 13226-13239.

6. S. W. Boettcher, J. M. Spurgeon, M. C. Putnam, E. L. Warren, D. B. Turner-Evans, M. D. Kelzenberg, J. R. Maiolo, H. A. Atwater and N. S. Lewis, *Science (Washington, DC, U. S.)*, 2010, **327**, 185-187.

7. S. W. Boettcher, E. L. Warren, M. C. Putnam, E. A. Santori, D. Turner-Evans, M. D. Kelzenberg, M. G. Walter, J. R. McKone, B. S. Brunschwig, H. A. Atwater and N. S. Lewis, *J. Am. Chem. Soc.*, 2011, **133**, 1216-1219.

8. X. Yang, A. Wolcott, G. Wang, A. Sobo, R. C. Fitzmorris, F. Qian, J. Z. Zhang and Y. Li, *Nano Lett.*, 2009, **9**, 2331-2336.

9. Y. Ling, G. Wang, D. A. Wheeler, J. Z. Zhang and Y. Li, *Nano Lett.*, 2011, **11**, 2119-2125.

10. S. C. Warren, K. Voitchovsky, H. Dotan, C. M. Leroy, M. Cornuz, F. Stellacci, C. Hebert, A. Rothschild and M. Graetzel, *Nat. Mater.*, 2013, **12**, 842-849.

11. A. Stepanovich, K. Sliozberg, W. Schuhmann and A. Ludwig, *Int. J. Hydrogen Energy*, 2012, **37**, 11618-11624.

12. R. van de Krol, Y. Liang and J. Schoonman, *J. Mater. Chem.*, 2008, **18**, 2311-2320.

13. M. A. Butler, *J. Appl. Phys.*, 1977, **48**, 1914-1920.

14. A. Enesca, A. Duta, M. Nanu, C. Enache, R. van der Krol and J. Schoonman, Institute of Electrical and Electronics Engineers, 2005, pp. 293-296.

15. G. Hodes, D. Cahen and J. Manassen, *Nature (London)*, 1976, **260**, 312-313.

16. K. Liu, D. T. Foord and L. Scipioni, *Nanotechnology*, 2005, **16**, 10-14.

17. T. Horie and T. Iwai, *J. Phys. Soc. Jpn.*, 1961, **16**, 424-429.

18. B. M. Wanklyn, *J. Cryst. Growth*, 1968, **2**, 251-253.

19. F. H. Jones, K. Rawlings, J. S. Foord, R. G. Egdell, J. B. Pethica, B. M. R. Wanklyn, S. C. Parker and P. M. Oliver, *Surf. Sci.*, 1996, **359**, 107-121.

20. E. Salje and H. Hatami, *Z. Anorg. Allg. Chem.*, 1973, **396**, 267-270.

21. G. Hagg and A. Magneli, *Ark. Kemi, Mineral. Geol.*, 1944, **19A**, 14 pp.

22. P. Gado and A. Magneli, *Mater. Res. Bull.*, 1966, **1**, 33-44.

23. J. G. Allpress, R. J. D. Tilley and M. J. Sienko, *J. Solid State Chem.*, 1971, **3**, 440-451.

24. R. J. D. Tilley, *Mater. Res. Bull.*, 1970, **5**, 813-823.

25. M. Spichiger-Ulmann and J. Augustynski, *J. Appl. Phys.*, 1983, **54**, 6061-6064.

26. J. C. Hill and K.-S. Choi, *J. Phys. Chem. C*, 2012, **116**, 7612-7620.

27. A. Tacca, L. Meda, G. Marra, A. Savoini, S. Caramori, V. Cristino, C. A. Bignozzi, V. G. Pedro, P. P. Boix, S. Gimenez and J. Bisquert, *ChemPhysChem*, 2012, **13**, 3025-3034, S3025/3021-S3025/3029.

Chapter IV

1. A. J. Bard and M. A. Fox, *Acc. Chem. Res.*, 1995, **28**, 141-145.

2. M. G. Walter, E. L. Warren, J. R. McKone, S. W. Boettcher, Q. Mi, E. A. Santori and N. S. Lewis, *Chem. Rev. (Washington, DC, U. S.)*, 2010, **110**, 6446-6473.

3. S. Y. Reece, J. A. Hamel, K. Sung, T. D. Jarvi, A. J. Esswein, J. J. H. Pijpers and D. G. Nocera, *Science (Washington, DC, U. S.)*, 2011, **334**, 645-648.

4. J. Rossmeisl, Z. W. Qu, H. Zhu, G. J. Kroes and J. K. Norskov, *J. Electroanal. Chem.*, 2007, **607**, 83-89.

5. R. D. Britt, *Adv. Photosynth.*, 1996, **4**, 137-164.

6. A. Harriman, I. J. Pickering, J. M. Thomas and P. A. Christensen, *J. Chem. Soc., Faraday Trans. 1*, 1988, **84**, 2795-2806.

7. C. C. L. McCrory, S. Jung, I. M. Ferrer, S. M. Chatman, J. C. Peters and T. F. Jaramillo, *J. Am. Chem. Soc.*, 2015, **137**, 4347-4357.

8. H. Chen and S. Trasatti, *J. Indian Chem. Soc.*, 1993, **70**, 323-330.

9. S. Siracusano, N. Van Dijk, E. Payne-Johnson, V. Baglio and A. S. Arico, *Appl. Catal., B*, 2015, **164**, 488-495.

10. C. Le Pape-Rerolle, M. A. Petit and R. Wiart, *J. Appl. Electrochem.*, 1999, **29**, 1347-1350.

11. J. Emsley, *Nature's building blocks : an A-Z guide to the elements*, Oxford. New York : Oxford University Press, Oxford, New York, 2001.

12. Y. Zhao, E. A. Hernandez-Pagan, N. M. Vargas-Barbosa, J. L. Dysart and T. E. Mallouk, *J. Phys. Chem. Lett.*, 2011, **2**, 402-406.

13. G. Gu, B. Zheng, W. Q. Han, S. Roth and J. Liu, *Nano Lett.*, 2002, **2**, 849-851.

14. Y. Baek and K. Yong, *J. Phys. Chem. C*, 2007, **111**, 1213-1218.

15. B. Cao, J. Chen, X. Tang and W. Zhou, *J. Mater. Chem.*, 2009, **19**, 2323-2327.

16. N. F. Razina and L. N. Gur'eva, *Izv. Akad. Nauk Kaz. SSR, Ser. Khim.*, 1975, **25**, 31-35.

17. J. P. Randin, *J. Electron. Mater.*, 1978, **7**, 47-63.

18. A. M. Smith, M. G. Kast, B. A. Nail, S. Aloni and S. W. Boettcher, *J. Mater. Chem. A*, 2014, **2**, 6121-6129.

19. A. Georg and V. Wittwer, *Proc. SPIE-Int. Soc. Opt. Eng.*, 1994, **2255**, 314-321.

20. A. Georg, W. Graf and V. Wittwer, *Sol. Energy Mater. Sol. Cells*, 1998, **51**, 353-370.

21. A. Deneuville and P. Gerard, *J. Electron. Mater.*, 1978, **7**, 559-588.

Chapter V

1. N. S. Lewis and D. G. Nocera, *Proc. Natl. Acad. Sci. U. S. A.*, 2006, **103**, 15729-15735.

2. D. Abbott, *Proc. IEEE*, 2010, **98**, 42-66.

3. M. G. Walter, E. L. Warren, J. R. McKone, S. W. Boettcher, Q. Mi, E. A. Santori and N. S. Lewis, *Chem. Rev.*, 2010, **110**, 6446-6473.

4. H. B. Gray, *Nat Chem*, 2009, **1**, 7-7.

5. J. Rossmeisl, Z. W. Qu, H. Zhu, G. J. Kroes and J. K. Nørskov, *J. Electroanal. Chem.*, 2007, **607**, 83-89.

6. J. B. Gerken, S. E. Shaner, R. C. Masse, N. J. Porubsky and S. S. Stahl, *Energy Environ. Sci.*, 2014, **7**, 2376-2382.

7. C. C. L. McCrory, S. Jung, J. C. Peters and T. F. Jaramillo, *J. Am. Chem. Soc.*, 2013, **135**, 16977-16987.

8. H. Alemu and K. Juettner, *Electrochim. Acta*, 1988, **33**, 1101-1109.

9. G. Beni, L. M. Schiavone, J. L. Shay, W. C. Dautremont-Smith and B. S. Schneider, *Nature (London)*, 1979, **282**, 281-283.

10. K. Sardar, S. C. Ball, J. D. B. Sharman, D. Thompsett, J. M. Fisher, R. A. P. Smith, P. K. Biswas, M. R. Lees, R. J. Kashtiban, J. Sloan and R. I. Walton, *Chem. Mater.*, 2012, **24**, 4192-4200.

11. J. A. Seabold and K.-S. Choi, *J. Am. Chem. Soc.*, 2012, **134**, 2186-2192.

12. C. C. L. McCrory, S. Jung, J. C. Peters and T. F. Jaramillo, *J. Am. Chem. Soc.*, 2013, **135**, 16977-16987.

13. L. Trotochaud, J. K. Ranney, K. N. Williams and S. W. Boettcher, *J. Am. Chem. Soc.*, 2012, **134**, 17253-17261.

14. R. D. L. Smith, M. S. Prevot, R. D. Fagan, S. Trudel and C. P. Berlinguette, *J. Am. Chem. Soc.*, 2013, **135**, 11580-11586.

15. R. Subbaraman, D. Tripkovic, K.-C. Chang, D. Strmcnik, A. P. Paulikas, P. Hirunsit, M. Chan, J. Greeley, V. Stamenkovic and N. M. Markovic, *Nat. Mater.*, 2012, **11**, 550-557.

16. X. Li, F. C. Walsh and D. Pletcher, *Phys. Chem. Chem. Phys.*, 2011, **13**, 1162-1167.

17. L. Trotochaud, S. L. Young, J. K. Ranney and S. W. Boettcher, *J. Am. Chem. Soc.*, 2014.

18. D. A. Corrigan, *J. Electrochem. Soc.*, 1987, **134**, 377-384.

19. D. A. Corrigan and R. M. Bendert, *J. Electrochem. Soc.*, 1989, **136**, 723-728.

20. M. W. Louie and A. T. Bell, *J. Am. Chem. Soc.*, 2013, **135**, 12329-12337.

21. T. M. S. J. L. Letcher, *Materials for a sustainable future*, RSC Pub., Cambridge, UK, 2012.

22. M. Dincă, Y. Surendranath and D. G. Nocera, *Proc. Nat. Acad. Sci.*, 2010.

23. D. K. Bediako, B. Lassalle-Kaiser, Y. Surendranath, J. Yano, V. K. Yachandra and D. G. Nocera, *J. Am. Chem. Soc.*, 2012, **134**, 6801-6809.

24. D. K. Bediako, Y. Surendranath and D. G. Nocera, *J. Am. Chem. Soc.*, 2013, **135**, 3662-3674.

25. M. S. Burke, M. G. Kast, L. Trotochaud, A. M. Smith and S. W. Boettcher, *J. Am. Chem. Soc.*, 2015, **137**, 3638-3648.

26. M. Huynh, D. K. Bediako, Y. Liu and D. G. Nocera, *J. Phys. Chem. C*, 2014, **118**, 17142-17152.

27. L. Martinez, D. Leinen, F. Martin, M. Gabas, J. R. Ramos-Barrado, E. Quagliata and E. A. Dalchiele, *J. Electrochem. Soc.*, 2007, **154**, D126-D133.